NASA
Technical
Paper
3168

March 1992

Installation Effects of Wing-Mounted Turbofan Nacelle-Pylons on a 1/17-Scale, Twin-Engine, Low-Wing Transport Model

Odis C. Pendergraft, Jr.,
Anthony M. Ingraldi,
Richard J. Re,
and Timmy T. Kariya

NASA
Technical
Paper
3168

1992

Installation Effects of Wing-Mounted Turbofan Nacelle-Pylons on a 1/17-Scale, Twin-Engine, Low-Wing Transport Model

Odis C. Pendergraft, Jr.,
Anthony M. Ingraldi,
and Richard J. Re
Langley Research Center
Hampton, Virginia

Timmy T. Kariya
ViGYAN, Inc.
Hampton, Virginia

National Aeronautics and
Space Administration
Office of Management
Scientific and Technical
Information Program

Abstract

A twin-engine, low-wing transport model, with a supercritical wing of aspect ratio 10.8 designed for a cruise Mach number of 0.77 and a lift coefficient of 0.55, was tested in the Langley 16-Foot Transonic Tunnel. The purpose of this test was to compare the wing-nacelle interference effects of flow-through nacelles simulating *superfan* engines (very high bypass ratio (BPR $\approx$ 18) turbofan engines) with the wing-nacelle interference effects of current-technology turbofan engines (BPR $\approx$ 6). Forces and moments on the complete model were measured with a strain-gage balance, and extensive external static-pressure measurements (383 orifice locations) were made on the wing, nacelles, and pylons of the model. Data were taken at Mach numbers from 0.50 to 0.80 and at model angles of attack from -4° to 8°. Test results indicate that flow-through nacelles with a very high bypass ratio can be installed on a low-wing transport model with a lower installation drag penalty than for a conventional turbofan nacelle at a design cruise Mach number of 0.77 and lift coefficient of 0.55.

Introduction

Aircraft manufacturers have focused much of their research and development efforts on improving the performance of commercial transport aircraft by increasing the aerodynamic efficiency, by utilizing turbofan engines with improved (lower) specific fuel consumption (SFC), and by improving the installed performance of the turbofan engine nacelles. The airframe-associated improvements stem from advances in structural materials, machining methods, and computer-aided design techniques that have allowed the use of more efficient, high-aspect-ratio (ratio of wing span squared to wing area) wings. The propulsion-related improvements in turbofan engine efficiency are primarily a result of an increase in the ratio of fan flow to engine core flow (i.e., bypass ratio (BPR)); thus, marked decreases in SFC are provided. Consequently, the current design trends for commercial aircraft are toward higher turbofan engine bypass ratios (increased nacelle diameter relative to thrust) and higher wing aspect ratio (reduced wing chord relative to wing span and area, ref. 1). As a result, nacelle sizes have grown much larger with respect to the wing chord and could result in large nacelle-wing mutual interference effects for low-wing transports with conventional underwing nacelle-pylon layouts. Interference caused by this type of installation may degrade the performance of the new supercritical wing airfoils (which are much more sensitive to small flow disturbances) by causing premature shock formation and flow separation on the wing, which leads to severe drag penalties. These penalties may be large enough to negate the decrease in SFC realized from increased BPR.

Since the early 1980's, Langley Research Center has been investigating the problems and solutions related to the installation of twin turbofan nacelles on transport-type aircraft with supercritical airfoil wings. Previous investigations with a 1/24-scale high-wing transport model (refs. 2 to 10) were conducted in the Langley 16-Foot Transonic Tunnel at Mach numbers from 0.40 to 0.85 and at angles of attack from -4° to 6°. The wing of this model had a quarter-chord sweep of 30°, a wing aspect ratio of 7.52, and a design cruise Mach number of 0.80. However, the flow-through nacelles tested on this model represented turbofan engines with lower bypass ratios (BPR = 4 to 6), and the wing aspect ratio was low relative to current-technology designs. Additionally, the high-wing design of this model is not typical of current and future commercial transport designs, which have predominantly low-wing locations. Therefore, a new model based on the response of the airframe industry to the fuel crisis of the late 1970's—designed to obtain better fuel economy by cruising at a slightly lower Mach number ($M_{\text{des}} = 0.77$)—was fabricated. The model design incorporated a high-aspect-ratio wing (10.795) with a quarter-chord sweep of 21.0°. On this model, flow-through nacelles for engines with very high bypass ratios (BPR = 10 to 20) were tested to determine the best location and orientation on the supercritical wing for minimum drag of the wing-body-nacelle combination. This model had sufficient pressure instrumentation to provide details of the flow around the nacelles, pylons, and wing; therefore, performance differences between various nacelle installations indicated by aerodynamic force and moment data could be explained.

The present investigation was conducted to examine the aerodynamic characteristics of this new wind-tunnel model and to compare the installed interference effects of current-technology turbofan-engine (BPR $\approx$ 6) nacelles with the installed interference effects of turbofan engine nacelles with very high bypass ratios (BPR $\approx$ 18).

Symbols and Abbreviations

ATF	advanced turbofan-engine nacelle (BPR $\approx$ 6)
BL	model buttline (lateral dimension from centerline of model, positive in spanwise direction), in.

BPR	bypass ratio (ratio of fan mass flow to primary, or core, mass flow)
b	wing span, in.
C_D	drag coefficient, $\frac{\text{Drag}}{q_\infty S}$
ΔC_D	increment of drag coefficient produced by installation of nacelle-pylon combination
$C_{D,i}$	nacelle internal-drag coefficient
C_L	lift coefficient, $\frac{\text{Lift}}{q_\infty S}$
C_m	pitching-moment coefficient (positive nose up), $\frac{\text{Pitching moment}}{q_\infty S\bar{c}}$
C_p	static-pressure coefficient, $\frac{p - p_\infty}{q_\infty}$
c	chord measured in wing reference plane, in.
$\bar{c}$	mean aerodynamic chord, in.
config.	configuration
FS	fuselage station (axial dimension measured from nose of model, positive toward tail), in.
I_{nac}	nacelle incidence angle relative to fuselage centerline in pitch (positive for nacelle nose up), deg
LE	leading edge
M	Mach number
p	static pressure, lb/in^2
q_∞	free-stream dynamic pressure, lb/in^2
R	radius, in.
S	wing reference area, in^2
SF-1	superfan engine nacelle (BPR $\approx$ 18)—configuration 1
SF-2	superfan engine nacelle (BPR $\approx$ 18)—configuration 2
T_{nac}	nacelle toe-in angle relative to fuselage centerline in yaw (positive for nacelle nose toward fuselage), deg
t/c	thickness-to-chord ratio
typ.	typical
WL	water line (vertical dimension, positive up, from fuselage centerline), in.
WRP	wing reference plane
x	local axial distance, in.
y	local lateral distance, in.
z	local vertical distance, in.
α	model angle of attack, deg
η	wing semispan location, $y/(b/2)$
ρ_∞	air density, lb/in^3
ϕ	meridian angle measured about centerline of nacelle (advances clockwise from zero at top of nacelle when looking upstream), deg

Subscripts:

des	design cruise point
div	drag divergence
MAC	mean aerodynamic chord, in.
∞	free stream

Apparatus and Procedure

Wind Tunnel and Model Support

The present investigation was conducted in the Langley 16-Foot Transonic Tunnel. This facility is a single-return, continuous-flow, atmospheric wind tunnel with a test section of octagonal cross section and a throat cross-sectional area of 199.15 ft^2. The 31-ft-long test section (maximum length at subsonic speeds) has slots located at the corners of the octagon that vent the test section to a surrounding plenum to provide transonic capability. Test-section airspeed is continuously variable between Mach numbers of 0.20 and 1.30 with an accuracy of ± 0.005. The wall divergence in the test section is adjusted as a function of the airstream dew point and Mach number to minimize any longitudinal static-pressure gradients in the test section. The model was sting mounted and held near the test-section centerline at all angles of attack by the support-system arrangement. Further information on the wind tunnel and model support equipment can be found in references 11 and 12.

Model

The sketch and photograph in figure 1 show the basic research transport model in the clean-wing configuration (without nacelles), including overall dimensions. This model is a 1/17-scale representation of a 150-passenger, twin-engine transport designed to cruise at $M_\infty = 0.77$ and $C_L = 0.55$. The wing and all three nacelle designs were furnished by airframe and engine companies in cooperative programs with NASA. Since only the interference effects of the nacelle-pylon installation on the wing were being studied, no attempt was made to add tail surfaces to the model. Instead, a simple afterbody was used to fair the cylindrical midsection into the base surrounding the model support sting.

Fuselage. The geometry and coordinates of the fuselage nose and afterbody sections are shown in figure 2(a). The fuselage is 80.0 in. long, has a maximum diameter of 9.0 in., and is made up of an ellipsoidal nose profile with circular cross sections, a cylindrical midsection, and an afterbody of elliptical cross sections. The afterbody keel profile is shown in figure 2(b), which also depicts the sting cavity and the fuselage base.

Wing. The planform geometry of the wing as shown in figure 3(a) has a span of 79.668 in., an aspect ratio of 10.795, a taper ratio of 0.275, and a quarter-chord sweep of 21.0°. The quarter-chord dihedral of the wing reference trapezoid is 5.78°, and the wing reference plane (WRP) intersects the vertical plane of symmetry of the model at WL = -1.370 (1.370 in. below the fuselage centerline). In the planform view, the leading edge of the wingtip is rounded with a cubic curve between the wing leading edge and the outermost wing section. (See inset of fig. 3(a).)

Representative airfoil sections and their span locations for the wing, with their relative positions to the wing reference plane, and the chord dimension for each section are shown in figure 3(b). Table I gives the airfoil ordinates for the sections shown in figure 3(b).

The airfoil sections inboard of $\eta = 0.400$ were designed to reduce overall pitching-moment coefficient C_m characteristics of the wing by adding loading to the lower leading-edge region and removing aft loading on the inboard wing. This additional forward loading reduces lower-surface velocities between 0 percent and 40 percent chord and results in smaller leading-edge radii for these inboard airfoil sections, which helps control the stall characteristics of the clean wing.

The airfoil contouring should also reduce the adverse interference effects caused by nacelle-pylon installation by compensating for the typical flow accelerations in the wing-pylon junction. The distributions of twist and maximum thickness ratio for the model wing are shown in figure 3(c).

Wing-fuselage fairings. The geometry of the fairings used to provide smooth transition shapes and to control boundary-layer growth and separation in the wing-fuselage juncture is shown in figure 4. An overall view of the bottom and side of the fairings is displayed in figure 4(a); the sections for the forward fairings and the aft fairings are shown in figures 4(b) and 4(c).

Nacelle-pylon installations. Sketches of the flow-through advanced turbofan (ATF) nacelle, which represents an engine with a bypass ratio of about 6, are shown in figures 5(a) and (b). Figure 5(c) is a photograph of the model with ATF nacelles installed in the Langley 16-Foot Transonic Tunnel. This configuration represents a current-technology turbofan and served as the baseline for the investigation. The two primary components of the nacelle are the fan cowl and the core cowl.

The major dimensions of the ATF nacelle fan cowl and core cowl are shown in figure 5(a). The internal and external cross-sectional shapes of the ATF nacelle fan cowl are symmetric about the nacelle centerline in the vertical plane and nonsymmetric about the nacelle centerline in the horizontal plane. The ATF nacelle core cowl is axisymmetric about the nacelle centerline.

The part of the pylon that attaches the fan cowl to the core cowl has a cross-sectional shape that is symmetric about the nacelle centerline in the vertical plane. The pylon cross-sectional shape, along with coordinates of a typical section 2.613 in. above the nacelle centerline, is shown in figure 5(b). The cross-sectional shape inside the fan cowl is similar, but it has a shorter flat midsection. The pylon for the ATF nacelle has a leading edge that extends from the top of the fan cowl—1.463 in. aft of the fan cowl lip—and intersects the wing lower surface just below and aft of the leading edge. The pylon trailing edge, starting with the pylon shelf, extends from the trailing edge of the nacelle core cowl at an angle of 5° and then sweeps upward at an angle of 39° to intersect the wing lower surface at about the 75-percent-chord location. The cross-sectional shape of the pylon in a horizontal plane has a rounded leading edge with slightly diverging flat-sided extensions that fair into a typical trailing-edge shape.

A sketch of a flow-through nacelle that represents a very high bypass ratio (BPR $\approx$ 18) or superfan engine nacelle, designated as SF-1, is shown in figures 6(a) and (b). Figure 6(c) is a photograph of the model with SF-1 nacelles installed in the Langley 16-Foot Transonic Tunnel. The two primary components of the SF-1 nacelle are the fan cowl and the centerbody. Included in the sketch of figure 6(a) are the major dimensions of the fan cowl and the centerbody of the SF-1 nacelle. Both components of the SF-1 nacelle are axisymmetric about the nacelle centerline. The centerbody represents the fan spinner and gas generator with the core flow cross-sectional area removed.

The pylon for the SF-1 nacelle has a leading edge that extends from the top of the fan cowl—1.395 in. aft of the fan cowl lip—and intersects the wing lower surface just below and aft of the leading edge. The pylon trailing edge, starting with the pylon shelf, extends from the trailing edge of the nacelle centerbody at an angle of -3°, 0°, or 3°, depending on nacelle incidence angle I_{nac}, and then sweeps upward at an angle of 40° to intersect the wing lower surface at about the 75-percent-chord location. A typical cross-sectional shape (a modified NACA 0012 airfoil section with flat-sided extensions at the airfoil maximum thickness) with coordinates is shown in figure 6(b) for a section passing through the upper fan-cowl exit lip. The cross-sectional shape above the fan cowl is similar but has a longer flat midsection extension.

A sketch of a flow-through nacelle that represents an alternate design of a superfan engine nacelle with a very high bypass ratio ($\text{BPR} \approx 18$), designated as SF-2, is shown in figures 7(a) and (b). Figure 7(c) is a photograph of the model with SF-2 nacelles installed in the Langley 16-Foot Transonic Tunnel. The three primary components of the SF-2 nacelle are the fan cowl, the core cowl, and the centerbody.

The major dimensions of the SF-2 nacelle fan cowl, core cowl, and centerbody are indicated in figure 7(a). While the cross-sectional shapes of the centerbody and the core cowl are axisymmetric about the nacelle centerline, the fan cowl is symmetric about the nacelle centerline in the vertical plane and nonsymmetric about the nacelle centerline in the horizontal plane.

The struts that attach the nacelle fan cowl to the centerbody are aligned with the centerline of the nacelle in the vertical plane, and the struts that connect the nacelle core cowl to the centerbody extend in the horizontal plane. These struts have a chord length of 2 in. and a cross-sectional shape defined as airfoil section NACA 0018.

The pylon for the SF-2 nacelle has a leading edge that extends from the top of the fan cowl, 0.467 in. aft of the fan-cowl lip, and extends over the top of the wing leading edge. The pylon trailing edge extends from the trailing edge of the nacelle fan cowl without bifurcating the fan flow duct; the trailing edge follows the estimated shape of the fan plume aft of the fan-cowl trailing edge. The pylon shelf sweeps upwards at 3°, and the pylon trailing edge intersects the wing trailing edge at a sweep angle of 25°. The cross-sectional shape of the pylon is shown in figure 7(b) along with coordinates for a section located just above the maximum diameter of the fan cowl, 3.383 in. above the nacelle centerline.

Instrumentation

The model was completely metric and contained a conventional six-component strain-gage balance that measured overall aerodynamic forces and moments. The balance moment center was located slightly aft of the quarter-chord of the wing mean aerodynamic chord (fuselage station 41.902) at fuselage station (FS) 42.760, BL 0.000, and WL 0.000. (See fig. 1(a).) The model angle of attack was measured with an electronic attitude transmitter mounted in the model nose.

Chordwise pressure distributions were measured on the left upper wing surface at 8 spanwise stations and on the left lower wing surface at 10 stations. The spanwise locations of the orifice rows are indicated in figure 8, and table II provides the orifice locations at each span station. Table II gives the fuselage station location for each orifice relative to the model nose as well as the local value of x/c. This information establishes the spatial relationship between the wing surface pressures and the nacelle-pylon pressures.

The orifices on the lower surface were concentrated in the vicinity of the nacelle-pylon installation locations η of 0.340 and 0.400, so that local flow phenomena around the pylons and nacelles could be examined in greater detail. Although the orifices were spread more uniformly on the upper surface, two rows of taps were located at the nacelle-pylon installation locations of 0.340 and 0.400.

The orifice rows at span stations 0.200, 0.463, 0.550, 0.700, and 0.900 contained 25 taps; each row included one orifice at the leading edge and 12 on the lower and upper surfaces. At span stations 0.277 and 0.400, there were 45 taps in each orifice row, including one orifice at the leading edge and 22 on each surface. The lower-surface orifice rows at $\eta = 0.310$, 0.375, and 0.428 and the upper-surface row at $\eta = 0.340$ contained 23 taps. Several orifices were omitted at various locations on the upper surface, because they were located near model-part interfaces or attachment points.

Nacelle-pylon surface pressures were measured only on the right-hand nacelle. One row of orifices was installed along either side of the pylon as shown in figure 9. All three nacelle configurations were instrumented with longitudinal orifice rows in the key meridian planes. (See fig. 9.) The meridian angle advances clockwise from 0° at the top of the nacelle when viewing the right-hand engine installation from the rear (see rear view). For all three nacelle configurations, the fan cowls were instrumented with orifice rows at $\phi = 30°$, $90°$, $180°$, $270°$, and $330°$. The core cowls of the ATF and SF-2 nacelles and the aft portion of the SF-1 centerbody were similarly instrumented. The forward portion of the SF-2 centerbody had orifice rows at $\phi = 0°$ and $180°$. Internal orifices on the ATF nacelle were located on the fan cowl at $\phi = 0°, 90°, 180°$, and $270°$, while the SF-1 nacelle had internal orifices on the fan cowl at $\phi = 30°, 90°, 180°, 270°$, and $330°$. For the SF-2 nacelle, internal orifices were located on the fan cowl at $\phi = 90°$ and $270°$ and on the core cowl at $\phi = 0°$ and $180°$. The rear-view sketches in figure 9 also show the position of the wing with respect to the nacelle and pylon. The locations of the orifices on the pylons and nacelles for the ATF, SF-1, and SF-2 configurations are given in tables III, IV, and V.

All pressure measurements on the wing, pylon, and nacelle were made with 13 electronically scanning pressure modules mounted in the hollow, removable nose section of the model. Each module contains 32 individual pressure transducers capable of being recorded simultaneously. This instrumentation arrangement required only soft, flexible, electrical wires to be routed across the balance and through the support system; therefore, mechanical restraint on the model is minimized. Pressures were measured at 16 positions on the fuselage base and in the sting cavity (fig. 2(b)) by individual pressure transducers located outside the tunnel test section.

Tests

This investigation was conducted at Mach numbers from 0.50 to 0.80 and nominal angles of attack from $-4°$ to a maximum of $8°$, depending on balance load limits and maximum lift coefficients desired. Mach number was varied in increments of 0.01 near the design cruise point ($M_{\text{des}} = 0.77$), and angle of attack was varied in 0.25° increments around the design cruise lift coefficient of 0.55 to obtain detailed information. Reynolds number based on the mean aerodynamic chord of the wing varied from 2.0×10^6 to 2.7×10^6, depending on Mach number and free-stream temperature.

Aerodynamic force and pressure data were obtained for the clean-wing model (fig. 1) and for the model with the ATF, SF-1, and SF-2 nacelle-pylon configurations installed. All three nacelle-pylon configurations were tested at $\eta = 0.400$, and the ATF nacelle-pylon configuration was also tested at $\eta = 0.340$. The pylon-to-wing mounts allowed the nacelle toe-in T_{nac} (positive for nacelle inlet tilted toward fuselage) to be set from 0° to 3° and allowed the nacelle incidence I_{nac} relative to the fuselage centerline to be set from $-3°$ (nacelle tilted nose down) to 4°. The nacelles were rotated for incidence and toe-in angles about the pivot point for each nacelle. (See figs. 5(a), 6(a), and 7(a).)

On the upper and lower wing surfaces, the natural transition location from laminar to turbulent flow was obtained by using photographic images of fluorescent oil flow on the wing surfaces. These images were used to position grit transition strips on the wing surfaces to obtain transition as far aft as possible, to minimize boundary-layer thickness, and to still fix transition in one location for all test conditions. The application of the grit transition strips on the wing is shown in figure 10. Grit size was determined from procedures in reference 13.

Boundary-layer transition was fixed on the rest of the model by 0.1-in-wide strips of silicon carbide grit; these strips were sized and positioned by the methods of reference 13. A strip of No. 100 grit was applied 1.0 in. behind the fuselage nose. (See fig. 11.) Strips of No. 120 grit were placed 0.375 in. behind the fan-cowl leading edge on both the inner and outer surfaces for all three nacelle configurations. (See fig. 12.) The same applications were made on the core cowls of the ATF and SF-2 nacelles. Strips of No. 120 grit were placed 0.75 in. behind the centerbody nose for the SF-1 and SF-2 nacelles. No. 120 grit strips were also applied on the exterior of pylons as shown in figures 12(a), 12(b), and 12(c) for the ATF, SF-1, and SF-2 nacelles.

Data Reduction

All data from the model and wind tunnel were recorded simultaneously on magnetic tape. Averaged values were used to compute standard aerodynamic force and moment coefficients with the methods and equations of reference 14. The trapezoidal planform area of the wing and the mean aerodynamic chord were used as reference area and length, respectively. Resulting model force and moment coefficients were referred to the stability axis system; the moment reference center was located at the quarter-chord of the wing mean aerodynamic chord (FS 41.902).

The model angle of attack was computed by correcting the averaged values from the electronic attitude transmitter for wind-tunnel upflow, which was determined from inverted-model, clean-wing runs. Sting-cavity and fuselage-base pressures were used to correct the axial-force data for pressure forces acting on the fuselage base and in the sting cavity.

The drag data were corrected for the internal drag of the nacelles, which was computed based on measured internal-nacelle static pressures and external core-cowl or centerbody static pressures (ref. 15). The internal-drag correction method of reference 15 was developed for single-flow nacelles. However, this method has also been applied to separate-flow nacelles. (See ref. 9.) The internal-drag calculations accounted for both the pressure and friction forces that were acting on the internal surfaces of the nacelles and portions of the pylons. In addition, pressure and skin-friction forces exerted on the external surface of the core cowls, centerbodies, and portions of the pylons that would be scrubbed by the fan jet were included in the internal-drag accounting procedure. The nacelle and pylon surfaces included in the internal-drag calculations are indicated in figure 13. The ATF nacelle-pylon surfaces used for internal-drag calculations were the inner surface of the fan cowl, the entire internal and external surface of the core cowl, and the pylon surface encompassed by the fan cowl. (See fig. 13(a).) The pylon surface that would be affected by the fan jet extended vertically at the fan-cowl exit from the fan-cowl inner surface to the external surface of the core cowl and maintained this radial distance to the end of the core-cowl exit. For the SF-1 nacelle-pylon configuration, the inner surface of the fan cowl, the entire centerbody surface area, and the pylon surface encompassed by the fan cowl were used for internal-drag calculations. (See fig. 13(b).) The surface of the pylon outside the fan cowl that was included in friction calculations spanned vertically at the fan-cowl exit from the fan-cowl inner surface to the centerbody and maintained this radial distance to the end of the centerbody. The internal-nacelle surfaces of the SF-2 nacelle that were used for internal-drag calculations included the inner surface of the fan cowl, the external and internal surfaces of the core cowl, the entire centerbody surface area, and all internal centerbody and core support-strut surfaces. (See fig. 13(c).)

Presentation of Results

The aerodynamic force and moment coefficient data and static-pressure coefficient data taken during the investigation are presented graphically in the figures. Although only part of the force and pressure coefficient data that were obtained are presented, the amount of plotted data presented is sufficient to evaluate the interference effects of the nacelle installations. The pressure plots are limited to the design cruise condition ($M_\infty = 0.77$ at $C_L \approx 0.55$) and to $M_\infty = 0.80$ at $C_L \approx 0.55$, where the most severe flow problems are likely to occur. Additional static-pressure coefficient data and force and moment coefficient data were obtained for the various combinations of nacelle incidence angle and toe-in angle at all the Mach numbers investigated. These results include data for the clean-wing configuration at Mach numbers of 0.50, 0.60, 0.70, 0.73, 0.75, 0.76, 0.77, 0.78, 0.79, and 0.80 and include data for configurations with nacelles and pylons installed at Mach numbers of 0.50, 0.70, 0.75, 0.76, 0.77, 0.78, and 0.80 for nominal angles of attack from −4° to 8° ($C_L \approx 0.0$ to 0.8), depending on Mach number.

The major results of the investigation are presented in the following figures:

	Figure
Nacelle internal-drag corrections	14
Drag polars over the tested range of incidence angles and as toe angles for $M_\infty = 0.77$:	
ATF nacelle installed at $\eta = 0.34$	15
ATF nacelle installed at $\eta = 0.40$	16
SF-1 nacelle installed at $\eta = 0.40$	17
SF-2 nacelle installed at $\eta = 0.40$	18
Aerodynamic force data for the clean-wing configuration compared with the data for the nacelle-on configurations:	
ATF nacelle installed at $\eta = 0.34$ and $\eta = 0.40$	19
ATF, SF-1, and SF-2 installed at $\eta = 0.40$	20
Drag increments for nacelles installed at $\eta = 0.40$ and 0.34 for $M_\infty = 0.77$ and $C_L = 0.55$	21
Drag rise at $C_L = 0.55$ for the clean-wing configuration and for nacelles installed at $\eta = 0.40$	22
Comparison of the effects of nacelles installed at $\eta = 0.40$ on the wing surface pressure coefficients:	
$M_\infty = 0.50$ and $C_L \approx 0.55$	23
$M_\infty = 0.77$ and $C_L \approx 0.55$	24
$M_\infty = 0.80$ and $C_L \approx 0.55$	25
Effects of nacelles installed at $\eta = 0.40$ on upper and lower surface pressure coefficients:	
ATF nacelle, $M_\infty = 0.77$ and $C_L \approx 0.55$	26
SF-1 nacelle, $M_\infty = 0.77$ and $C_L \approx 0.55$	27
SF-2 nacelle, $M_\infty = 0.77$ and $C_L \approx 0.55$	28
ATF nacelle, $M_\infty = 0.80$ and $C_L \approx 0.55$	29
SF-1 nacelle, $M_\infty = 0.80$ and $C_L \approx 0.55$	30
SF-2 nacelle, $M_\infty = 0.80$ and $C_L \approx 0.55$	31
Local pressure effects for nacelles installed at $\eta = 0.40$ for $M_\infty = 0.77$ and $C_L \approx 0.55$:	
ATF nacelle	32
SF-1 nacelle	33
SF-2 nacelle	34

Discussion

The computed internal-drag corrections decreased substantially with increasing lift coefficient for all the nacelle installations tested. (The internal-drag coefficients shown in figure 14 represent the total drag for two nacelles.) The large decrease in internal-drag coefficient versus C_L was the result of a favorable interaction of the wing lower-surface pressure field on the aft portions of the installed nacelle, as indicated by the positive C_p values on the aft portions of the nacelle assemblies (figs. 32 to 34). This favorable interference increased with increasing lift coefficient. The combination of positive pressure coefficients and aft-facing core-surface areas produced a negative internal-drag increment (internal thrust) for the aft nacelle regions. The internal drag calculated for the ATF nacelle installed at the $\eta = 0.34$ and $\eta = 0.40$ wing locations indicates that the net force acting on the "internal" surfaces of the nacelle was in the direction of thrust for lift coefficients above about 0.15. Therefore, the corrected drag levels for the ATF nacelle installations increased in some instances when the nacelle internal-drag corrections were applied to the measured model drag.

To determine the most favorable nacelle orientation for each configuration, each nacelle installation was tested over a range of nacelle incidence and toe angles. The optimum settings for a given nacelle installation were established by comparing the drag data for the various settings and determining which combination of incidence and toe angles produced the lowest drag level at $M_\infty = 0.77$ and $C_L = 0.55$ (the design cruise condition for the wing). In some cases, the selected optimum incidence settings occurred at either the maximum or minimum angle tested. In these instances, the true optimum incidence is not known, since data were not obtained at incidence angles that bracketed the selected "optimum" incidence. The drag data shown in figure 15 indicate that 1° toe and 3° incidence were the optimum settings for the ATF nacelle installed at $\eta = 0.340$. The difference in drag levels for the various toe and nacelle settings is about five drag counts or less at the cruise lift coefficient. For the ATF nacelle installed at $\eta = 0.400$, figure 16 shows that the optimum toe and incidence settings were 1° and 4°, respectively. Again, the drag levels obtained for the various incidence and toe settings differ by only five drag counts or less at the cruise lift coefficient. Figure 16(a) indicates that the variation of the ATF nacelle toe angle between 1° and 3° resulted in negligible differences in drag at the cruise lift coefficient when the nacelle was installed at $\eta = 0.400$. Since the highest incidence setting tested for the ATF nacelle was 4° (fig. 16(b)), it is not known whether 4° is actually the optimum incidence setting for the ATF nacelle installed at $\eta = 0.400$. For the SF-1 nacelle installed at $\eta = 0.400$, the most favorable toe and incidence settings tested were 1° and $-3°$, respectively (fig. 17). The optimum settings tested for the SF-2 nacelle installed at $\eta = 0.400$ were 1° toe and 3° incidence. (See fig. 18.) The remaining figures and discussion concerning the nacelle installations are based exclusively on data obtained for the optimum toe and incidence settings for each nacelle.

Figure 19 indicates that installation of the ATF nacelle at the 40.0-percent wing semispan location resulted in lower drag than at the 34.0-percent wing semispan location. This result is evident over the entire test range of Mach number and lift coefficient and may be the result of stronger adverse nacelle-pylon-fuselage interactions at the inboard location ($\eta = 0.340$). The ATF nacelle installed at $\eta = 0.340$ resulted in more negative pitching moment than the installation at $\eta = 0.400$. As indicated by the increase of C_m with C_L, all the configurations were longitudinally unstable because of the lack of horizontal tail surfaces on the model. The loss of lift at a given angle of attack caused by the installation of the ATF nacelle was roughly equal for both installation locations. However, installation of nacelles produced an increase in lift-curve slope at all Mach numbers. The presence of the ATF nacelles delayed the onset of separation or reduced the extent of separation on the wing above $M_\infty = 0.77$, as indicated by the extended linear range of C_L and C_m in figures 19(f) and 19(g) and by the more abrupt increase in the drag of the clean-wing configuration relative to the nacelle-installed configurations in the high-lift range.

Figure 20 indicates that the model configuration with the SF-2 nacelle installed at the 40.0-percent wing semispan location produced the lowest drag of all the configurations over most of the Mach number and lift range investigated. The drag coefficient for the SF-2 nacelle configuration at cruise was about 41 drag counts higher than the clean-wing configuration drag coefficient for the same condition. This is a 13-percent increase in overall drag for the SF-2 configuration relative to the clean wing. At the cruise condition, the drag level for the SF-2 nacelle configuration was about 8 drag counts less than the drag for the ATF nacelle configuration and about 15 drag counts less than that for the SF-1 nacelle configuration. (The ATF and SF-1 nacelle installations resulted in drag increases of 15 and 18 percent, respectively, relative to the clean-wing configuration at the cruise point.) The SF-1 nacelle installation resulted in the greatest loss of lift relative to the clean-wing configuration and had the highest overall drag of the nacelle installations tested. The relatively low drag levels for the SF-2 nacelle installation were unexpected, since the SF-2 nacelle is much larger than the ATF nacelle and since it could create more adverse interference and, therefore, higher installed drag. Figure 21 shows that the interference drag for the SF-2 nacelle installation is actually lower than for the ATF nacelle configuration. The interference drag was calculated by subtracting the computed nacelle-pylon, flat-plate, skin-friction drag from the total drag increment for the nacelle installation. In addition to having the lowest installed drag, the SF-2 nacelle configuration resulted in a higher drag-rise Mach number than either the clean-wing configuration or the other nacelle configurations (fig. 22). Much of the improved performance with the SF-2 nacelle installation can probably be attributed to its pylon geometry. Unfortunately, there are several major geometry differences between the SF-2 nacelle-pylon and the other nacelle-pylons (i.e., pylon curvature and leading- and trailing-edge locations); these differences make it difficult to determine which geometry feature was responsible for the improved drag performance.

The attachment of the nacelle-pylon to the wing induced disturbances in the pressure distribution on the wing upper and lower surfaces relative to the clean-wing pressure distributions. For $M_\infty = 0.50$ and $C_L \approx 0.55$, the effects of the nacelles installed at $\eta = 0.400$ on wing surface pressures were most noticeable between $\eta = 0.310$ and $\eta = 0.463$ (fig. 23). The most obvious difference at $M_\infty = 0.50$ is the substantial reduction in the leading-edge suction peak between $\eta = 0.340$ and $\eta = 0.463$. A portion of the decrease in leading-edge suction is a result of slight differences in lift coefficient for the different configurations, as shown in table VI, but most of the suction loss is caused by the presence of the nacelles and pylons. Unexpectedly, the nacelle-pylon installations induced pressure disturbances on the lower surface of the wing that are less severe in magnitude than those on the upper surface of the wing. Apparently, the wing lower-surface contouring inboard of the 40.0-percent semispan location, which was intended to alleviate the effects of nacelle-pylon installation, was successful.

For a free-stream Mach number of 0.77 (the wing design Mach number, figs. 24 and 26 to 28), the nacelle installation affects a larger portion of the wing than at $M_\infty = 0.50$. At $\eta = 0.200$, all the nacelle installations induced higher velocities over the first 30 percent of the wing upper surface, as indicated by the lower values of C_p in that region. This effect is not nearly as pronounced at $\eta = 0.277$. At $\eta = 0.277$, the SF-2 nacelle installation induced higher velocities over the forward 30 percent of the wing upper surface than either the ATF or SF-1 nacelle installations. This result is probably caused by the extension of the SF-2 pylon up and over the leading edge of the wing. A similar effect is seen on the wing upper surface at the 34.0-percent semispan station. Outboard of the nacelle installation location ($\eta > 0.400$), effects opposite of those noted inboard are observed. The nacelle installations induced lower velocities and higher pressures over the forward 40 percent of the wing upper surface at $\eta = 0.463$ and $\eta = 0.55$. The SF-2 nacelle installation had the largest effect at these locations. The pressure distributions on the lower surface of the wing at $\eta = 0.375$ indicate that the SF-2 nacelle installation induced lower pressures on the forward 30 percent of the wing chord and higher pressures on the aft 70 percent. The ATF nacelle installation induced the highest velocities on the wing lower surface at $\eta = 0.375$ near 40 percent chord. Just outboard of the nacelle installation location ($\eta = 0.428$), effects similar to those at $\eta = 0.375$ are observed.

The flow field over the upper surface of the wing at $M_\infty = 0.80$ is characterized by a shock structure located between 60 and 70 percent chord and extending over most of the wing span. The nacelle installations had varying but small effects on the shock strength and location (figs. 25 and 29 to 31) over the wing upper surface. The SF-2 nacelle installation attenuated the shock over the inboard portion of the wing, and the ATF nacelle installation appears to have increased the shock strength at the most outboard wing orifice row ($\eta = 0.900$). These effects are indicative of the interference drag levels associated with the SF-2 and ATF nacelle installations; the ATF nacelle installation has higher interference drag than the SF-2 nacelle installation (fig. 21), and the model with the SF-2 nacelles had the highest drag divergence Mach number (fig. 22). The lower-surface pressures for the stations nearest the nacelle-pylon location ($\eta = 0.375$ and $\eta = 0.428$) further illustrate the adverse effects of the ATF nacelle installation relative to the other nacelle installations (fig. 25). At $\eta = 0.375$, inboard of the nacelle-pylon, a shock is apparent just past the 40-percent-chord location with the ATF nacelle installed. (The critical pressure coefficient at $M_\infty = 0.80$ is -0.44.) On the outboard side of the nacelle-pylon location at $\eta = 0.428$, there is no shock evident, but the ATF nacelle installation does induce higher velocities over the aft 60-percent wing chord than the SF-2 nacelle installation.

Concluding Remarks

The installation of *superfans* (very high bypass ratio (BPR $\approx$ 18) turbofans) on conventional transport configurations with a design cruise Mach number of 0.77 does not present an insurmountable installation drag problem. Model test results with flow-through nacelles show that a superfan nacelle can be installed on a low-wing transport configuration and have a lower installation drag penalty than a conventional turbofan (BPR $\approx$ 6) nacelle. One superfan configuration resulted in a drag increase of 18 percent above the clean-wing drag at the design cruise point, while another superfan installation increased drag by 13 percent. The conventional turbofan nacelle installation had an installation drag penalty of 15 percent at the cruise condition. Test results also indicate that pylon geometry is an important factor in the overall drag penalty associated with a given nacelle installation.

NASA Langley Research Center
Hampton, VA 23665-5225
January 7, 1992

References

1. Henderson, William P.; and Patterson, James C., Jr.: Propulsion Installation Characteristics for Turbofan Transports. AIAA-83-0087, Jan. 1983.
2. Lee, Edwin E., Jr.; and Pendergraft, Odis C., Jr.: *Installation Effects of Long-Duct Pylon-Mounted Nacelles on a Twin-Jet Transport Model With Swept Supercritical Wing.* NASA TP-2457, 1985.
3. Lamb, Milton; Abeyounis, William K.; and Patterson, James C., Jr.: *Nacelle/Pylon/Wing Integration on a Transport Model With a Natural Laminar Flow Nacelle.* NASA TP-2439, 1985.
4. Abeyounis, William K.; and Patterson, James C., Jr.: *Effect of Underwing Aft-Mounted Nacelles on the Longitudinal Aerodynamic Characteristics of a High-Wing Transport Airplane.* NASA TP-2447, 1985.
5. Henderson, William P.; and Abeyounis, William K.: *Aerodynamic Characteristics of a High-Wing Transport Configuration With an Over-the-Wing Nacelle-Pylon Arrangement.* NASA TP-2497, 1985.
6. Carlson, John R.; and Lamb, Milton: Integration Effects of Pylon Geometry and Rearward Mounted Nacelles for a High-Wing Transport. AIAA-87-1920, June–July 1987.
7. Bangert, L. H.; Krivec, D. K.; and Segall, R. N.: *Effects of Nacelle Configuration/Position on Performance of Subsonic Transport.* NASA CR-3743, 1983.
8. Lamb, Milton; Carlson, John R.; and Pendergraft, Odis C., Jr.: *Integration Effects of D-Shaped, Underwing, Aft-Mounted, Separate-Flow, Flow-Through Nacelles on a High-Wing Transport.* NASA TM-4018, 1987.
9. Lamb, Milton; and Abeyounis, William K.: *Integration Effects of Underwing Forward- and Rearward-Mounted Separate-Flow, Flow-Through Nacelles on a High-Wing Transport.* NASA TM-87627, 1986.
10. Carlson, John R.; and Lamb, Milton: *Integration Effects of Pylon Geometry on a High-Wing Transport Airplane.* NASA TP-2877, 1989.
11. Corson, Blake W., Jr.; Runckel, Jack F.; and Igoe, William B.: *Calibration of the Langley 16-Foot Transonic Tunnel With Test Section Air Removal.* NASA TR R-423, 1974.
12. Staff of the Propulsion Aerodynamics Branch: *A User's Guide to the Langley 16-Foot Transonic Tunnel Complex, Revision 1.* NASA TM-102750, 1990. (Supersedes NASA TM-83186, compiled by Kathryn H. Peddrew, 1981.)
13. Braslow, Albert L.; Hicks, Raymond M.; and Harris, Roy V., Jr.: *Use of Grit-Type Boundary-Layer-Transition Trips on Wind-Tunnel Models.* NASA TN D-3579, 1966.
14. Mercer, Charles E.; Berrier, Bobby L.; Capone, Francis J.; Grayston, Alan M.; and Sherman C. D.: *Computations for the 16-Foot Transonic Tunnel—NASA, Langley Research Center, Revision 1.* NASA TM-86319, 1987. (Supersedes NASA TM-86319, 1984.)
15. Putnam, Lawrence E.: *Effects of Upper-Surface Nacelles on Longitudinal Aerodynamic Characteristics of High-Wing Transport Configuration.* NASA TP-2579, 1986.

Table I. Wing Ordinates Relative to Wing Reference Plane

BL = 3.278	$\eta = 0.082$		$c = 15.149$
LE at FS 32.855, WL −2.196			
Upper surface		Lower surface	
x/c	z/c	x/c	z/c
0.0000	0.0000	0.0000	0.0000
0.0003	0.0019	0.0001	−0.0063
0.0006	0.0032	0.0003	−0.0075
0.0010	0.0047	0.0005	−0.0085
0.0015	0.0061	0.0009	−0.0100
0.0022	0.0079	0.0015	−0.0119
0.0030	0.0095	0.0023	−0.0140
0.0041	0.0115	0.0034	−0.0164
0.0053	0.0134	0.0048	−0.0189
0.0068	0.0155	0.0065	−0.0216
0.0087	0.0177	0.0085	−0.0244
0.0108	0.0200	0.0109	−0.0273
0.0134	0.0224	0.0137	−0.0303
0.0164	0.0249	0.0169	−0.0333
0.0198	0.0273	0.0205	−0.0364
0.0236	0.0297	0.0246	−0.0395
0.0279	0.0320	0.0293	−0.0427
0.0327	0.0341	0.0344	−0.0460
0.0380	0.0362	0.0402	−0.0494
0.0440	0.0382	0.0465	−0.0528
0.0506	0.0400	0.0534	−0.0563
0.0580	0.0416	0.0611	−0.0600
0.0660	0.0431	0.0694	−0.0638
0.0748	0.0444	0.0786	−0.0677
0.0845	0.0455	0.0886	−0.0718
0.0950	0.0464	0.0996	−0.0760
0.1064	0.0470	0.1115	−0.0804
0.1188	0.0473	0.1244	−0.0848
0.1322	0.0473	0.1383	−0.0894
0.1467	0.0471	0.1534	−0.0942
0.1623	0.0465	0.1696	−0.0990
0.1791	0.0455	0.1870	−0.1038
0.1971	0.0442	0.2056	−0.1088
0.2162	0.0425	0.2255	−0.1137
0.2366	0.0405	0.2466	−0.1186
0.2582	0.0381	0.2690	−0.1234
0.2809	0.0353	0.2926	−0.1281
0.3049	0.0322	0.3173	−0.1326
0.3300	0.0288	0.3433	−0.1370
0.3561	0.0250	0.3703	−0.1410
0.3833	0.0210	0.3983	−0.1447
0.4113	0.0168	0.4271	−0.1480
0.4402	0.0123	0.4568	−0.1509
0.4697	0.0076	0.4870	−0.1533
0.4997	0.0027	0.5177	−0.1552
0.5302	−0.0025	0.5487	−0.1566
0.5608	−0.0079	0.5798	−0.1573
0.5915	−0.0136	0.6109	−0.1574
0.6221	−0.0196	0.6417	−0.1569
0.6524	−0.0259	0.6722	−0.1556
0.6823	−0.0324	0.7021	−0.1538
0.7116	−0.0390	0.7313	−0.1514
0.7402	−0.0458	0.7597	−0.1486
0.7680	−0.0527	0.7872	−0.1455
0.7948	−0.0596	0.8137	−0.1422
0.8206	−0.0665	0.8391	−0.1390
0.8453	−0.0733	0.8633	−0.1359
0.8689	−0.0800	0.8864	−0.1330
0.8913	−0.0866	0.9083	−0.1304
0.9125	−0.0930	0.9290	−0.1281
0.9324	−0.0992	0.9486	−0.1262
0.9511	−0.1052	0.9669	−0.1246
0.9686	−0.1109	0.9840	−0.1234
0.9850	−0.1162	1.0000	−0.1225
1.0000	−0.1209		

BL = 4.521	$\eta = 0.114$		$c = 14.467$
LE at FS 33.537, WL −2.076			
Upper surface		Lower surface	
x/c	z/c	x/c	z/c
0.0000	0.0000	0.0000	0.0000
0.0003	0.0019	0.0001	−0.0051
0.0006	0.0033	0.0003	−0.0063
0.0010	0.0046	0.0005	−0.0072
0.0015	0.0060	0.0009	−0.0086
0.0022	0.0076	0.0015	−0.0104
0.0030	0.0092	0.0023	−0.0123
0.0041	0.0111	0.0034	−0.0144
0.0053	0.0128	0.0048	−0.0167
0.0068	0.0147	0.0065	−0.0191
0.0087	0.0168	0.0085	−0.0216
0.0108	0.0189	0.0109	−0.0242
0.0134	0.0211	0.0137	−0.0269
0.0164	0.0234	0.0169	−0.0296
0.0198	0.0257	0.0205	−0.0324
0.0236	0.0279	0.0246	−0.0352
0.0279	0.0300	0.0293	−0.0381
0.0327	0.0321	0.0344	−0.0410
0.0380	0.0340	0.0402	−0.0440
0.0440	0.0359	0.0465	−0.0471
0.0506	0.0376	0.0534	−0.0503
0.0580	0.0393	0.0611	−0.0536
0.0660	0.0407	0.0694	−0.0570
0.0748	0.0420	0.0786	−0.0607
0.0845	0.0432	0.0886	−0.0644
0.0950	0.0442	0.0996	−0.0683
0.1064	0.0449	0.1115	−0.0724
0.1188	0.0455	0.1244	−0.0766
0.1322	0.0458	0.1383	−0.0809
0.1467	0.0458	0.1534	−0.0854
0.1623	0.0455	0.1696	−0.0899
0.1791	0.0450	0.1870	−0.0946
0.1971	0.0441	0.2056	−0.0993
0.2162	0.0429	0.2255	−0.1040
0.2366	0.0414	0.2466	−0.1087
0.2582	0.0395	0.2690	−0.1134
0.2809	0.0373	0.2926	−0.1180
0.3049	0.0348	0.3173	−0.1224
0.3300	0.0319	0.3433	−0.1266
0.3561	0.0288	0.3703	−0.1305
0.3833	0.0253	0.3983	−0.1341
0.4113	0.0216	0.4271	−0.1374
0.4402	0.0176	0.4568	−0.1402
0.4697	0.0133	0.4870	−0.1425
0.4997	0.0088	0.5177	−0.1443
0.5302	0.0040	0.5487	−0.1456
0.5608	−0.0011	0.5798	−0.1462
0.5915	−0.0066	0.6109	−0.1463
0.6221	−0.0124	0.6417	−0.1457
0.6524	−0.0184	0.6722	−0.1444
0.6823	−0.0247	0.7021	−0.1426
0.7116	−0.0312	0.7313	−0.1404
0.7402	−0.0378	0.7597	−0.1377
0.7680	−0.0445	0.7872	−0.1347
0.7948	−0.0512	0.8137	−0.1317
0.8206	−0.0579	0.8391	−0.1286
0.8453	−0.0645	0.8633	−0.1257
0.8689	−0.0711	0.8864	−0.1229
0.8913	−0.0775	0.9083	−0.1205
0.9125	−0.0838	0.9290	−0.1183
0.9324	−0.0898	0.9486	−0.1165
0.9511	−0.0957	0.9669	−0.1151
0.9686	−0.1013	0.9840	−0.1140
0.9850	−0.1066	1.0000	−0.1131
1.0000	−0.1114		

Table I. Continued

BL = 10.942	$\eta = 0.275$		$c = 10.940$
LE at FS 37.064, WL −1.443			
Upper surface		Lower surface	
x/c	z/c	x/c	z/c
0.0000	0.0000	0.0000	0.0000
0.0003	0.0022	0.0001	−0.0024
0.0006	0.0034	0.0003	−0.0034
0.0010	0.0045	0.0005	−0.0041
0.0015	0.0056	0.0009	−0.0052
0.0022	0.0069	0.0015	−0.0064
0.0030	0.0081	0.0023	−0.0077
0.0041	0.0094	0.0034	−0.0090
0.0053	0.0107	0.0048	−0.0104
0.0068	0.0120	0.0065	−0.0118
0.0087	0.0135	0.0085	−0.0132
0.0108	0.0149	0.0109	−0.0146
0.0134	0.0164	0.0137	−0.0160
0.0164	0.0179	0.0169	−0.0174
0.0198	0.0194	0.0205	−0.0188
0.0236	0.0209	0.0246	−0.0202
0.0279	0.0224	0.0293	−0.0216
0.0327	0.0240	0.0344	−0.0232
0.0380	0.0256	0.0402	−0.0249
0.0440	0.0273	0.0465	−0.0267
0.0506	0.0290	0.0534	−0.0286
0.0580	0.0306	0.0611	−0.0306
0.0660	0.0322	0.0694	−0.0326
0.0748	0.0337	0.0786	−0.0349
0.0845	0.0353	0.0886	−0.0373
0.0950	0.0368	0.0996	−0.0399
0.1064	0.0382	0.1115	−0.0426
0.1188	0.0396	0.1244	−0.0454
0.1322	0.0409	0.1383	−0.0484
0.1467	0.0421	0.1534	−0.0515
0.1623	0.0432	0.1696	−0.0548
0.1791	0.0442	0.1870	−0.0581
0.1971	0.0451	0.2056	−0.0615
0.2162	0.0458	0.2255	−0.0649
0.2366	0.0463	0.2466	−0.0683
0.2582	0.0466	0.2690	−0.0717
0.2809	0.0466	0.2926	−0.0749
0.3049	0.0464	0.3173	−0.0780
0.3300	0.0460	0.3433	−0.0810
0.3561	0.0453	0.3703	−0.0836
0.3833	0.0442	0.3983	−0.0860
0.4113	0.0429	0.4271	−0.0879
0.4402	0.0412	0.4568	−0.0894
0.4697	0.0391	0.4870	−0.0904
0.4997	0.0365	0.5177	−0.0908
0.5302	0.0336	0.5487	−0.0907
0.5608	0.0302	0.5798	−0.0901
0.5915	0.0265	0.6109	−0.0889
0.6221	0.0224	0.6417	−0.0873
0.6524	0.0179	0.6722	−0.0853
0.6823	0.0132	0.7021	−0.0831
0.7116	0.0081	0.7313	−0.0807
0.7402	0.0029	0.7597	−0.0782
0.7680	−0.0025	0.7872	−0.0757
0.7948	−0.0079	0.8137	−0.0734
0.8206	−0.0135	0.8391	−0.0712
0.8453	−0.0190	0.8633	−0.0693
0.8689	−0.0246	0.8864	−0.0676
0.8913	−0.0300	0.9083	−0.0662
0.9125	−0.0354	0.9290	−0.0651
0.9324	−0.0406	0.9486	−0.0643
0.9511	−0.0458	0.9669	−0.0638
0.9686	−0.0509	0.9840	−0.0637
0.9850	−0.0560	1.0000	−0.0639
1.0000	−0.0608		

BL = 13.544	$\eta = 0.340$		$c = 9.525$
LE at FS 38.490, WL −1.182			
Upper surface		Lower surface	
x/c	z/c	x/c	z/c
0.0000	0.0000	0.0000	0.0000
0.0003	0.0024	0.0001	−0.0022
0.0006	0.0035	0.0003	−0.0033
0.0010	0.0047	0.0005	−0.0040
0.0015	0.0058	0.0009	−0.0051
0.0022	0.0070	0.0015	−0.0064
0.0030	0.0082	0.0023	−0.0077
0.0041	0.0096	0.0034	−0.0091
0.0053	0.0108	0.0048	−0.0105
0.0068	0.0122	0.0065	−0.0119
0.0087	0.0136	0.0085	−0.0134
0.0108	0.0150	0.0109	−0.0148
0.0134	0.0165	0.0137	−0.0162
0.0164	0.0180	0.0169	−0.0177
0.0198	0.0196	0.0205	−0.0191
0.0236	0.0211	0.0246	−0.0205
0.0279	0.0226	0.0293	−0.0220
0.0327	0.0242	0.0344	−0.0236
0.0380	0.0258	0.0402	−0.0253
0.0440	0.0275	0.0465	−0.0270
0.0506	0.0292	0.0534	−0.0288
0.0580	0.0308	0.0611	−0.0308
0.0660	0.0324	0.0694	−0.0327
0.0748	0.0340	0.0786	−0.0348
0.0845	0.0356	0.0886	−0.0370
0.0950	0.0371	0.0996	−0.0394
0.1064	0.0386	0.1115	−0.0418
0.1188	0.0400	0.1244	−0.0444
0.1322	0.0413	0.1383	−0.0470
0.1467	0.0426	0.1534	−0.0498
0.1623	0.0438	0.1696	−0.0526
0.1791	0.0449	0.1870	−0.0554
0.1971	0.0459	0.2056	−0.0583
0.2162	0.0467	0.2255	−0.0612
0.2366	0.0474	0.2466	−0.0640
0.2582	0.0479	0.2690	−0.0667
0.2809	0.0482	0.2926	−0.0692
0.3049	0.0483	0.3173	−0.0716
0.3300	0.0482	0.3433	−0.0737
0.3561	0.0479	0.3703	−0.0755
0.3833	0.0473	0.3983	−0.0770
0.4113	0.0464	0.4271	−0.0780
0.4402	0.0452	0.4568	−0.0785
0.4697	0.0437	0.4870	−0.0784
0.4997	0.0418	0.5177	−0.0779
0.5302	0.0395	0.5487	−0.0767
0.5608	0.0368	0.5798	−0.0750
0.5915	0.0338	0.6109	−0.0729
0.6221	0.0304	0.6417	−0.0703
0.6524	0.0267	0.6722	−0.0675
0.6823	0.0227	0.7021	−0.0645
0.7116	0.0184	0.7313	−0.0615
0.7402	0.0139	0.7597	−0.0586
0.7680	0.0092	0.7872	−0.0559
0.7948	0.0043	0.8137	−0.0535
0.8206	−0.0007	0.8391	−0.0515
0.8453	−0.0058	0.8633	−0.0498
0.8689	−0.0109	0.8864	−0.0485
0.8913	−0.0159	0.9083	−0.0476
0.9125	−0.0209	0.9290	−0.0471
0.9324	−0.0259	0.9486	−0.0470
0.9511	−0.0308	0.9669	−0.0474
0.9686	−0.0357	0.9840	−0.0481
0.9850	−0.0407	1.0000	−0.0491
1.0000	−0.0454		

Table I. Continued

BL = 14.902	$\eta = 0.374$	$c = 8.857$	
LE at FS 39.210, WL −1.051			
Upper surface		Lower surface	
x/c	z/c	x/c	z/c
0.0000	0.0000	0.0000	0.0000
0.0003	0.0024	0.0001	−0.0022
0.0006	0.0036	0.0003	−0.0033
0.0010	0.0047	0.0005	−0.0040
0.0015	0.0059	0.0009	−0.0052
0.0022	0.0071	0.0015	−0.0064
0.0030	0.0083	0.0023	−0.0077
0.0041	0.0097	0.0034	−0.0091
0.0053	0.0109	0.0048	−0.0106
0.0068	0.0123	0.0065	−0.0121
0.0087	0.0137	0.0085	−0.0135
0.0108	0.0152	0.0109	−0.0150
0.0134	0.0167	0.0137	−0.0165
0.0164	0.0182	0.0169	−0.0179
0.0198	0.0197	0.0205	−0.0194
0.0236	0.0212	0.0246	−0.0209
0.0279	0.0228	0.0293	−0.0224
0.0327	0.0244	0.0344	−0.0240
0.0380	0.0260	0.0402	−0.0257
0.0440	0.0277	0.0465	−0.0274
0.0506	0.0294	0.0534	−0.0292
0.0580	0.0310	0.0611	−0.0311
0.0660	0.0326	0.0694	−0.0330
0.0748	0.0342	0.0786	−0.0350
0.0845	0.0358	0.0886	−0.0371
0.0950	0.0374	0.0996	−0.0393
0.1064	0.0389	0.1115	−0.0416
0.1188	0.0403	0.1244	−0.0440
0.1322	0.0417	0.1383	−0.0465
0.1467	0.0431	0.1534	−0.0491
0.1623	0.0443	0.1696	−0.0517
0.1791	0.0455	0.1870	−0.0543
0.1971	0.0466	0.2056	−0.0569
0.2162	0.0475	0.2255	−0.0595
0.2366	0.0483	0.2466	−0.0620
0.2582	0.0489	0.2690	−0.0644
0.2809	0.0494	0.2926	−0.0667
0.3049	0.0497	0.3173	−0.0687
0.3300	0.0498	0.3433	−0.0705
0.3561	0.0496	0.3703	−0.0720
0.3833	0.0492	0.3983	−0.0730
0.4113	0.0485	0.4271	−0.0737
0.4402	0.0476	0.4568	−0.0738
0.4697	0.0463	0.4870	−0.0733
0.4997	0.0447	0.5177	−0.0723
0.5302	0.0427	0.5487	−0.0706
0.5608	0.0403	0.5798	−0.0685
0.5915	0.0376	0.6109	−0.0658
0.6221	0.0345	0.6417	−0.0628
0.6524	0.0311	0.6722	−0.0595
0.6823	0.0274	0.7021	−0.0562
0.7116	0.0234	0.7313	−0.0529
0.7402	0.0191	0.7597	−0.0497
0.7680	0.0147	0.7872	−0.0469
0.7948	0.0100	0.8137	−0.0444
0.8206	0.0052	0.8391	−0.0424
0.8453	0.0003	0.8633	−0.0408
0.8689	−0.0046	0.8864	−0.0398
0.8913	−0.0096	0.9083	−0.0392
0.9125	−0.0145	0.9290	−0.0390
0.9324	−0.0193	0.9486	−0.0393
0.9511	−0.0241	0.9669	−0.0401
0.9686	−0.0290	0.9840	−0.0413
0.9850	−0.0340	1.0000	−0.0428
1.0000	−0.0387		

BL = 15.762	$\eta = 0.396$	$c = 8.492$	
LE at FS 39.646, WL −0.971			
Upper surface		Lower surface	
x/c	z/c	x/c	z/c
0.0000	0.0000	0.0000	0.0000
0.0003	0.0025	0.0001	−0.0021
0.0006	0.0036	0.0003	−0.0032
0.0010	0.0048	0.0005	−0.0040
0.0015	0.0059	0.0009	−0.0051
0.0022	0.0071	0.0015	−0.0064
0.0030	0.0083	0.0023	−0.0077
0.0041	0.0097	0.0034	−0.0092
0.0053	0.0109	0.0048	−0.0106
0.0068	0.0123	0.0065	−0.0121
0.0087	0.0138	0.0085	−0.0136
0.0108	0.0152	0.0109	−0.0151
0.0134	0.0167	0.0137	−0.0166
0.0164	0.0182	0.0169	−0.0181
0.0198	0.0197	0.0205	−0.0195
0.0236	0.0212	0.0246	−0.0210
0.0279	0.0228	0.0293	−0.0226
0.0327	0.0244	0.0344	−0.0242
0.0380	0.0260	0.0402	−0.0259
0.0440	0.0277	0.0465	−0.0276
0.0506	0.0294	0.0534	−0.0294
0.0580	0.0310	0.0611	−0.0312
0.0660	0.0326	0.0694	−0.0331
0.0748	0.0342	0.0786	−0.0350
0.0845	0.0358	0.0886	−0.0371
0.0950	0.0374	0.0996	−0.0392
0.1064	0.0389	0.1115	−0.0414
0.1188	0.0404	0.1244	−0.0437
0.1322	0.0418	0.1383	−0.0461
0.1467	0.0432	0.1534	−0.0485
0.1623	0.0445	0.1696	−0.0510
0.1791	0.0457	0.1870	−0.0534
0.1971	0.0468	0.2056	−0.0559
0.2162	0.0478	0.2255	−0.0583
0.2366	0.0487	0.2466	−0.0606
0.2582	0.0494	0.2690	−0.0629
0.2809	0.0499	0.2926	−0.0649
0.3049	0.0503	0.3173	−0.0668
0.3300	0.0505	0.3433	−0.0684
0.3561	0.0504	0.3703	−0.0696
0.3833	0.0501	0.3983	−0.0705
0.4113	0.0496	0.4271	−0.0709
0.4402	0.0488	0.4568	−0.0707
0.4697	0.0476	0.4870	−0.0700
0.4997	0.0462	0.5177	−0.0687
0.5302	0.0443	0.5487	−0.0668
0.5608	0.0421	0.5798	−0.0643
0.5915	0.0396	0.6109	−0.0614
0.6221	0.0367	0.6417	−0.0581
0.6524	0.0335	0.6722	−0.0545
0.6823	0.0300	0.7021	−0.0510
0.7116	0.0262	0.7313	−0.0475
0.7402	0.0221	0.7597	−0.0442
0.7680	0.0178	0.7872	−0.0413
0.7948	0.0132	0.8137	−0.0388
0.8206	0.0086	0.8391	−0.0368
0.8453	0.0038	0.8633	−0.0354
0.8689	−0.0010	0.8864	−0.0344
0.8913	−0.0059	0.9083	−0.0340
0.9125	−0.0107	0.9290	−0.0341
0.9324	−0.0155	0.9486	−0.0347
0.9511	−0.0203	0.9669	−0.0357
0.9686	−0.0251	0.9839	−0.0373
0.9850	−0.0300	1.0000	−0.0391
1.0000	−0.0348		

Table I. Continued

BL = 17.017	$\eta = 0.427$	$c = 8.062$	
LE at FS 40.249, WL −0.860			
Upper surface		Lower surface	
x/c	z/c	x/c	z/c
0.0000	0.0000	0.0000	0.0000
0.0003	0.0025	0.0001	−0.0021
0.0006	0.0037	0.0003	−0.0033
0.0010	0.0048	0.0005	−0.0040
0.0015	0.0060	0.0009	−0.0052
0.0022	0.0072	0.0015	−0.0065
0.0030	0.0084	0.0023	−0.0079
0.0041	0.0098	0.0034	−0.0093
0.0053	0.0111	0.0048	−0.0109
0.0068	0.0125	0.0065	−0.0124
0.0087	0.0140	0.0085	−0.0139
0.0108	0.0154	0.0109	−0.0155
0.0134	0.0169	0.0137	−0.0171
0.0164	0.0185	0.0169	−0.0186
0.0198	0.0201	0.0205	−0.0202
0.0236	0.0216	0.0246	−0.0217
0.0279	0.0232	0.0293	−0.0233
0.0327	0.0248	0.0344	−0.0250
0.0380	0.0265	0.0402	−0.0267
0.0440	0.0281	0.0465	−0.0285
0.0506	0.0298	0.0534	−0.0302
0.0580	0.0315	0.0611	−0.0320
0.0660	0.0331	0.0694	−0.0339
0.0748	0.0347	0.0786	−0.0358
0.0845	0.0363	0.0886	−0.0378
0.0950	0.0379	0.0996	−0.0398
0.1064	0.0394	0.1115	−0.0419
0.1188	0.0409	0.1244	−0.0441
0.1322	0.0424	0.1383	−0.0463
0.1467	0.0438	0.1534	−0.0485
0.1623	0.0452	0.1696	−0.0508
0.1791	0.0464	0.1870	−0.0531
0.1971	0.0476	0.2056	−0.0553
0.2162	0.0487	0.2255	−0.0575
0.2366	0.0496	0.2466	−0.0596
0.2582	0.0504	0.2690	−0.0616
0.2809	0.0511	0.2926	−0.0634
0.3049	0.0515	0.3173	−0.0650
0.3300	0.0518	0.3433	−0.0663
0.3561	0.0519	0.3703	−0.0673
0.3833	0.0517	0.3983	−0.0679
0.4113	0.0514	0.4271	−0.0680
0.4402	0.0507	0.4568	−0.0675
0.4697	0.0497	0.4870	−0.0664
0.4997	0.0484	0.5177	−0.0647
0.5302	0.0467	0.5487	−0.0624
0.5608	0.0448	0.5798	−0.0595
0.5915	0.0424	0.6109	−0.0561
0.6221	0.0398	0.6416	−0.0524
0.6524	0.0368	0.6721	−0.0484
0.6823	0.0336	0.7020	−0.0445
0.7116	0.0300	0.7312	−0.0407
0.7402	0.0261	0.7596	−0.0372
0.7680	0.0220	0.7871	−0.0341
0.7948	0.0176	0.8136	−0.0315
0.8206	0.0131	0.8390	−0.0295
0.8453	0.0085	0.8632	−0.0281
0.8689	0.0038	0.8863	−0.0274
0.8913	−0.0009	0.9082	−0.0272
0.9125	−0.0056	0.9289	−0.0276
0.9324	−0.0103	0.9485	−0.0285
0.9511	−0.0150	0.9668	−0.0299
0.9686	−0.0197	0.9839	−0.0319
0.9850	−0.0247	0.9999	−0.0341
1.0000	−0.0294		

BL = 23.912	$\eta = 0.600$	$c = 6.532$	
LE at FS 43.295, WL −0.288			
Upper surface		Lower surface	
x/c	z/c	x/c	z/c
0.0000	0.0000	0.0000	0.0000
0.0003	0.0028	0.0001	−0.0019
0.0006	0.0040	0.0003	−0.0031
0.0010	0.0051	0.0005	−0.0039
0.0015	0.0062	0.0009	−0.0051
0.0022	0.0075	0.0015	−0.0065
0.0030	0.0088	0.0023	−0.0079
0.0041	0.0102	0.0034	−0.0095
0.0053	0.0115	0.0048	−0.0111
0.0068	0.0129	0.0065	−0.0127
0.0087	0.0145	0.0085	−0.0143
0.0108	0.0160	0.0109	−0.0160
0.0134	0.0176	0.0137	−0.0177
0.0164	0.0192	0.0169	−0.0194
0.0198	0.0209	0.0205	−0.0210
0.0236	0.0225	0.0246	−0.0227
0.0279	0.0241	0.0293	−0.0243
0.0327	0.0258	0.0344	−0.0260
0.0380	0.0274	0.0402	−0.0277
0.0440	0.0291	0.0465	−0.0293
0.0506	0.0308	0.0534	−0.0309
0.0580	0.0324	0.0611	−0.0326
0.0660	0.0341	0.0694	−0.0342
0.0748	0.0357	0.0786	−0.0359
0.0845	0.0374	0.0886	−0.0377
0.0950	0.0391	0.0996	−0.0394
0.1064	0.0407	0.1115	−0.0412
0.1188	0.0424	0.1244	−0.0430
0.1322	0.0440	0.1383	−0.0447
0.1467	0.0456	0.1534	−0.0465
0.1623	0.0471	0.1696	−0.0482
0.1791	0.0487	0.1870	−0.0499
0.1971	0.0501	0.2056	−0.0515
0.2162	0.0515	0.2255	−0.0530
0.2366	0.0528	0.2466	−0.0544
0.2582	0.0539	0.2690	−0.0557
0.2809	0.0550	0.2926	−0.0568
0.3049	0.0559	0.3173	−0.0576
0.3300	0.0566	0.3433	−0.0582
0.3561	0.0572	0.3703	−0.0584
0.3833	0.0576	0.3983	−0.0582
0.4113	0.0578	0.4270	−0.0576
0.4402	0.0577	0.4567	−0.0563
0.4697	0.0574	0.4869	−0.0543
0.4997	0.0568	0.5176	−0.0517
0.5302	0.0559	0.5486	−0.0483
0.5608	0.0547	0.5797	−0.0442
0.5915	0.0532	0.6108	−0.0396
0.6221	0.0515	0.6416	−0.0346
0.6524	0.0494	0.6721	−0.0293
0.6823	0.0471	0.7020	−0.0241
0.7116	0.0444	0.7312	−0.0191
0.7402	0.0415	0.7596	−0.0146
0.7680	0.0383	0.7871	−0.0107
0.7948	0.0349	0.8136	−0.0074
0.8206	0.0312	0.8390	−0.0051
0.8453	0.0273	0.8632	−0.0036
0.8689	0.0233	0.8863	−0.0029
0.8913	0.0191	0.9082	−0.0030
0.9125	0.0149	0.9289	−0.0039
0.9324	0.0106	0.9485	−0.0055
0.9511	0.0062	0.9668	−0.0076
0.9686	0.0018	0.9839	−0.0104
0.9850	−0.0029	0.9999	−0.0135
1.0000	−0.0077		

Table I. Concluded

BL = 33.158	$\eta = 0.832$	$c = 4.591$	
LE at FS 47.341, WL 0.471			
Upper surface		Lower surface	
x/c	z/c	x/c	z/c
0.0000	0.0000	0.0000	0.0000
0.0003	0.0032	0.0001	−0.0016
0.0006	0.0044	0.0003	−0.0028
0.0010	0.0056	0.0005	−0.0036
0.0015	0.0068	0.0009	−0.0049
0.0022	0.0082	0.0015	−0.0063
0.0030	0.0095	0.0023	−0.0078
0.0041	0.0110	0.0034	−0.0094
0.0053	0.0124	0.0048	−0.0111
0.0068	0.0139	0.0065	−0.0128
0.0087	0.0156	0.0085	−0.0145
0.0108	0.0173	0.0109	−0.0163
0.0134	0.0190	0.0137	−0.0180
0.0164	0.0209	0.0169	−0.0198
0.0198	0.0227	0.0205	−0.0215
0.0236	0.0245	0.0246	−0.0232
0.0279	0.0264	0.0293	−0.0249
0.0327	0.0282	0.0344	−0.0266
0.0380	0.0301	0.0402	−0.0282
0.0440	0.0319	0.0465	−0.0298
0.0506	0.0338	0.0534	−0.0314
0.0580	0.0357	0.0611	−0.0329
0.0660	0.0375	0.0694	−0.0344
0.0748	0.0393	0.0786	−0.0358
0.0845	0.0412	0.0886	−0.0373
0.0950	0.0431	0.0996	−0.0387
0.1064	0.0449	0.1115	−0.0401
0.1188	0.0468	0.1244	−0.0414
0.1322	0.0487	0.1383	−0.0427
0.1467	0.0505	0.1534	−0.0440
0.1623	0.0524	0.1696	−0.0451
0.1791	0.0542	0.1870	−0.0462
0.1971	0.0560	0.2056	−0.0472
0.2162	0.0577	0.2255	−0.0481
0.2366	0.0594	0.2466	−0.0488
0.2582	0.0610	0.2690	−0.0493
0.2809	0.0625	0.2926	−0.0496
0.3049	0.0639	0.3172	−0.0496
0.3300	0.0652	0.3433	−0.0494
0.3561	0.0663	0.3702	−0.0488
0.3833	0.0673	0.3982	−0.0477
0.4113	0.0681	0.4270	−0.0462
0.4402	0.0688	0.4567	−0.0441
0.4697	0.0692	0.4869	−0.0413
0.4997	0.0694	0.5176	−0.0379
0.5302	0.0694	0.5486	−0.0337
0.5608	0.0691	0.5797	−0.0289
0.5915	0.0686	0.6108	−0.0235
0.6221	0.0677	0.6416	−0.0178
0.6524	0.0666	0.6721	−0.0117
0.6823	0.0653	0.7020	−0.0058
0.7116	0.0636	0.7312	−0.0001
0.7402	0.0616	0.7596	0.0052
0.7680	0.0594	0.7871	0.0098
0.7948	0.0569	0.8136	0.0137
0.8206	0.0541	0.8390	0.0168
0.8453	0.0511	0.8632	0.0190
0.8689	0.0478	0.8863	0.0204
0.8913	0.0443	0.9082	0.0210
0.9125	0.0406	0.9289	0.0208
0.9324	0.0368	0.9485	0.0200
0.9511	0.0328	0.9668	0.0184
0.9686	0.0288	0.9838	0.0164
0.9850	0.0248	0.9998	0.0143
1.0000	0.0211		

BL = 39.834	$\eta = 1.000$	$c = 3.188$	
LE at FS 50.264, WL 1.029			
Upper surface		Lower surface	
x/c	z/c	x/c	z/c
0.0000	0.0000	0.0000	0.0000
0.0003	0.0032	0.0001	−0.0012
0.0006	0.0044	0.0003	−0.0023
0.0010	0.0056	0.0005	−0.0031
0.0015	0.0067	0.0009	−0.0043
0.0022	0.0081	0.0015	−0.0056
0.0030	0.0094	0.0023	−0.0070
0.0041	0.0109	0.0034	−0.0085
0.0053	0.0123	0.0048	−0.0100
0.0068	0.0139	0.0065	−0.0115
0.0087	0.0156	0.0085	−0.0130
0.0108	0.0173	0.0109	−0.0144
0.0134	0.0191	0.0137	−0.0159
0.0164	0.0210	0.0169	−0.0173
0.0198	0.0228	0.0205	−0.0188
0.0236	0.0247	0.0246	−0.0201
0.0279	0.0266	0.0293	−0.0216
0.0327	0.0286	0.0344	−0.0229
0.0380	0.0305	0.0402	−0.0242
0.0440	0.0325	0.0465	−0.0255
0.0506	0.0345	0.0534	−0.0267
0.0580	0.0365	0.0611	−0.0280
0.0660	0.0386	0.0694	−0.0292
0.0748	0.0406	0.0786	−0.0305
0.0845	0.0428	0.0886	−0.0317
0.0950	0.0449	0.0996	−0.0329
0.1064	0.0470	0.1115	−0.0341
0.1188	0.0492	0.1244	−0.0353
0.1322	0.0514	0.1383	−0.0363
0.1467	0.0537	0.1534	−0.0374
0.1623	0.0559	0.1696	−0.0383
0.1791	0.0582	0.1870	−0.0392
0.1971	0.0605	0.2056	−0.0399
0.2162	0.0627	0.2255	−0.0406
0.2366	0.0650	0.2466	−0.0410
0.2582	0.0672	0.2689	−0.0412
0.2809	0.0694	0.2926	−0.0412
0.3049	0.0714	0.3173	−0.0409
0.3300	0.0734	0.3432	−0.0402
0.3561	0.0753	0.3702	−0.0392
0.3833	0.0770	0.3982	−0.0376
0.4113	0.0786	0.4270	−0.0355
0.4402	0.0801	0.4567	−0.0327
0.4697	0.0813	0.4869	−0.0293
0.4997	0.0823	0.5176	−0.0251
0.5302	0.0830	0.5486	−0.0203
0.5608	0.0835	0.5797	−0.0148
0.5915	0.0837	0.6108	−0.0088
0.6221	0.0835	0.6416	−0.0024
0.6524	0.0832	0.6721	0.0042
0.6823	0.0825	0.7019	0.0109
0.7116	0.0815	0.7312	0.0172
0.7402	0.0803	0.7595	0.0231
0.7680	0.0788	0.7871	0.0285
0.7948	0.0770	0.8135	0.0331
0.8206	0.0750	0.8389	0.0370
0.8453	0.0727	0.8631	0.0400
0.8689	0.0702	0.8862	0.0422
0.8913	0.0674	0.9081	0.0435
0.9125	0.0645	0.9288	0.0441
0.9324	0.0615	0.9484	0.0440
0.9511	0.0583	0.9667	0.0432
0.9686	0.0552	0.9838	0.0419
0.9850	0.0520	0.9998	0.0403
1.0000	0.0491		

TABLE II. Location of Wing Pressure Orifices by Fuselage Station

[Linear dimensions are in inches; values shown are fuselage stations]

x/c	Surfaces on which taps are located										
	Upper and lower		Lower	Upper	Lower	Upper and lower	Lower	Upper and lower			
	$\eta = 0.200$	$\eta = 0.277$	$\eta = 0.310$	$\eta = 0.340$	$\eta = 0.375$	$\eta = 0.400$	$\eta = 0.428$	$\eta = 0.463$	$\eta = 0.550$	$\eta = 0.700$	$\eta = 0.900$
0.0000	35.429*	37.115*	37.837	38.490	39.228	39.728*	40.263	40.894*	42.418*	45.033*	48.520*
0.0125	35.586	37.251	37.964	38.609	39.339	39.833	40.364	40.990	42.505	45.104	48.570
0.0250	35.743	37.387	38.091	38.728	39.450	39.939	40.465	41.086	42.592	45.175	48.621
0.0500	36.058	37.659	38.346	38.967	39.672	40.149	40.667	41.279	42.766	45.318	48.721
0.0750		37.932	38.600	39.205	39.893	40.360	40.869				
0.1000	36.686	38.204	38.855	39.443	40.115	40.571	41.071	41.664	43.113	45.603	48.922
0.1500		38.748	39.363		40.559	40.992	41.475				
0.2000	37.944	39.293	39.872	40.397	41.002	41.413†	41.879	42.434	43.808	46.173	49.325
0.2500		39.837	40.381	40.873	41.446	41.834	42.283				
0.3000	39.201	40.382	40.890	41.350	41.890	42.256	42.687	43.203	44.503	46.742	49.727
0.3500		40.926	41.398	41.826	42.333	42.677	43.091				
0.4000	40.459	41.471	41.907		42.777	43.098	43.496	43.974	45.198	47.312	50.130
0.4500		42.015	42.416	42.780	43.221	43.520†	43.900				
0.5000	41.716	42.560	42.925	43.256	43.664	43.941	44.304	44.743	45.894	47.882	50.532
0.5500		43.104	43.433	43.733	44.116	44.362	44.708				
0.6000	42.974	43.648	43.942	44.210	44.552	44.784	45.112	45.513	46.589	48.452	50.935
0.6500		44.193	44.451	44.686	45.005	45.205	45.516				
0.7000	44.231	44.737	44.960	45.163	45.439	45.626	45.920	46.283	47.284	49.022	51.337
0.7500		45.282	45.468	45.640	45.883	46.047	46.324				
0.8000	45.489	45.826	45.977	46.116	46.326	46.469	46.728	47.053	47.979	49.591	51.740
0.8500		46.371	46.486	46.593	46.770	46.890	47.132				
0.9000	46.746	46.915	46.995	47.070	47.213	47.311	47.536	47.822	48.674	50.161	52.142
0.9500		47.460	47.503	47.546	47.657	47.733	47.940				
Chord	12.575	10.889	10.175	9.533	8.876	8.426	8.081	7.698	6.951	5.698	4.025

*Upper-surface orifice only.

†Lower-surface orifice only.

Table III. Location of ATF Nacelle-Pylon Pressure Orifices by Fuselage Station

[Linear dimensions are in inches]

(a) $y/(b/2) = 0.340$

Pylon external orifices			
Inboard		Outboard	
FS	WL	FS	WL
31.275	−1.964		
32.235	−1.964	32.235	−1.964
33.594	−1.964	33.594	−1.964
34.593	−1.964	34.593	−1.964
36.313	−1.964	36.313	−1.964
37.672	−1.964	37.672	−1.964
39.032	−1.964	39.032	−1.964
39.430	−2.195	39.430	−2.195
40.775	−2.195	40.775	−2.195
42.826	−2.195	42.826	−2.195
43.811	−2.195	43.811	−2.195

Nacelle external orifices		
FS for ϕ of —		
30°/330°	90°/270°	180°
Fan cowl		
28.923	29.000	29.113
30.910	30.910	30.910
32.910	32.910	32.910
34.910	34.910	34.910
35.910	35.910	35.910
36.660	36.660	36.660
Core cowl		
36.718	36.718	36.718
37.343	37.343	37.343
38.293	38.293	38.293
39.243	39.243	39.243

Nacelle internal orifices			
FS for ϕ of —			
0°	90°	180°	270°
Fan cowl			
31.860	31.860	31.860	31.860
Core cowl			
35.844	35.844	35.844	35.844

Table III. Concluded

(b) $y/(b/2) = 0.400$

Pylon external orifices			
Inboard		Outboard	
FS	WL	FS	WL
32.572	−1.722		
33.532	−1.722	33.532	−1.722
34.891	−1.722	34.891	−1.722
36.250	−1.722	36.250	−1.722
37.610	−1.722	37.610	−1.722
38.969	−1.722	38.969	−1.722
40.329	−1.722	40.329	−1.722
40.727	−1.953	40.727	−1.953
42.072	−1.953	42.072	−1.953
44.123	−1.953	44.123	−1.953
45.108	−1.953	45.108	−1.953

Nacelle external orifices		
FS for ϕ of —		
30°/330°	90°/270°	180°
Fan cowl		
30.220	30.297	30.410
32.207	32.207	32.207
34.207	34.207	34.207
36.207	36.207	36.207
37.207	37.207	37.207
37.957	37.957	37.957
Core cowl		
38.015	38.015	38.015
38.640	38.640	38.640
39.590	39.590	39.590
40.540	40.540	40.540

Nacelle internal orifices			
FS for ϕ of —			
0°	90°	180°	270°
Fan cowl			
33.207	33.207	33.207	33.207
Core cowl			
37.141	37.141	37.141	37.141

Table IV. Location of SF-1 Nacelle-Pylon Pressure Orifices by Fuselage Station

[Linear dimensions are in inches]

Pylon external orifices			
Inboard		Outboard	
FS	WL	FS	WL
32.533	−1.589		
33.983	−1.589	33.983	−1.589
35.233	−1.589	35.233	−1.589
36.483	−1.589	36.483	−1.589
37.733	−1.589	37.733	−1.589
38.983	−1.589	38.983	−1.589
39.733	−1.589	39.733	−1.589
40.733	−1.829	40.733	−1.829
41.971	−2.040	41.971	−1.926
43.221	−2.082	43.221	−2.017
44.471	−2.016	44.471	−1.993

Nacelle external orifices		
FS for ϕ of —		
30°/330°	90°/270°	180°
Fan cowl		
30.876	30.876	30.876
31.641	31.641	31.641
32.641	32.641	32.641
34.141	34.141	34.141
35.141	35.141	35.141
36.141	36.141	36.141
37.141	37.141	37.141
37.876	37.876	37.876
Centerbody		
37.991	37.991	37.991
39.176	39.176	39.176
40.176	40.176	40.176

Nacelle internal orifices		
FS for ϕ of —		
30°/330°	90°/270°	180°
Fan cowl		
32.876	32.876	32.876

Table V. Location of SF-2 Nacelle-Pylon Pressure Orifices by Fuselage Station

[Linear dimensions are in inches]

Pylon external orifices			
Inboard		Outboard	
FS	WL	FS	WL
33.406	−1.603		
34.606	−1.603	34.606	−1.603
36.106	−1.603	36.106	−1.603
37.606	−1.603	37.606	−1.603
39.106	−1.603	39.106	−1.603
39.856	−1.603	39.856	−1.603
41.356	−2.006	41.356	−1.964
42.856	−1.987	42.856	−1.979
44.356	−2.003	44.356	−2.003
45.856	−2.003	45.856	−2.003

Nacelle external orifices			
FS for ϕ of —			
0°	30°/330°	90°/270°	180°
Centerbody			
29.565			29.565
30.065			30.065
31.065			31.065
32.115			32.115
Fan cowl			
	32.045	32.183	32.348
	34.106	34.106	34.106
	35.106	35.106	35.106
	36.106	36.106	36.106
	37.106	37.106	37.106
	37.856	37.856	37.856
Core cowl			
	36.848	36.848	36.848
	38.863	38.863	38.863
	39.863	39.863	39.863
	40.586	40.586	40.586

Nacelle internal orifices			
FS for ϕ of —			
0°	90°	180°	270°
Fan cowl			
	33.781		33.781
Core cowl			
39.703		39.703	

Table VI. Data Points Nearest the Cruise Lift Coefficient ($C_L = 0.55$) for Test Mach Numbers of 0.50, 0.77, and 0.80

Configuration	M	C_L
Clean wing	0.50	0.564
	0.77	0.527
	0.80	0.556
With ATF at $\eta = 0.340$	0.50	0.558
	0.77	0.552
	0.80	0.550
With ATF at $\eta = 0.400$	0.50	0.557
	0.77	0.545
	0.80	0.545
With SF-1 at $\eta = 0.400$	0.50	0.544
	0.77	0.527
	0.80	0.532
With SF-2 at $\eta = 0.400$	0.50	0.556
	0.77	0.539
	0.80	0.554

Area, ft^2	587.96
Aspect ratio	10.795
Taper ratio	.275
c/4 sweep in WRP, deg	21.0
c/4 dihedral, deg	5.78
$\bar{c}$, in.	8.176
M_{des}	.77

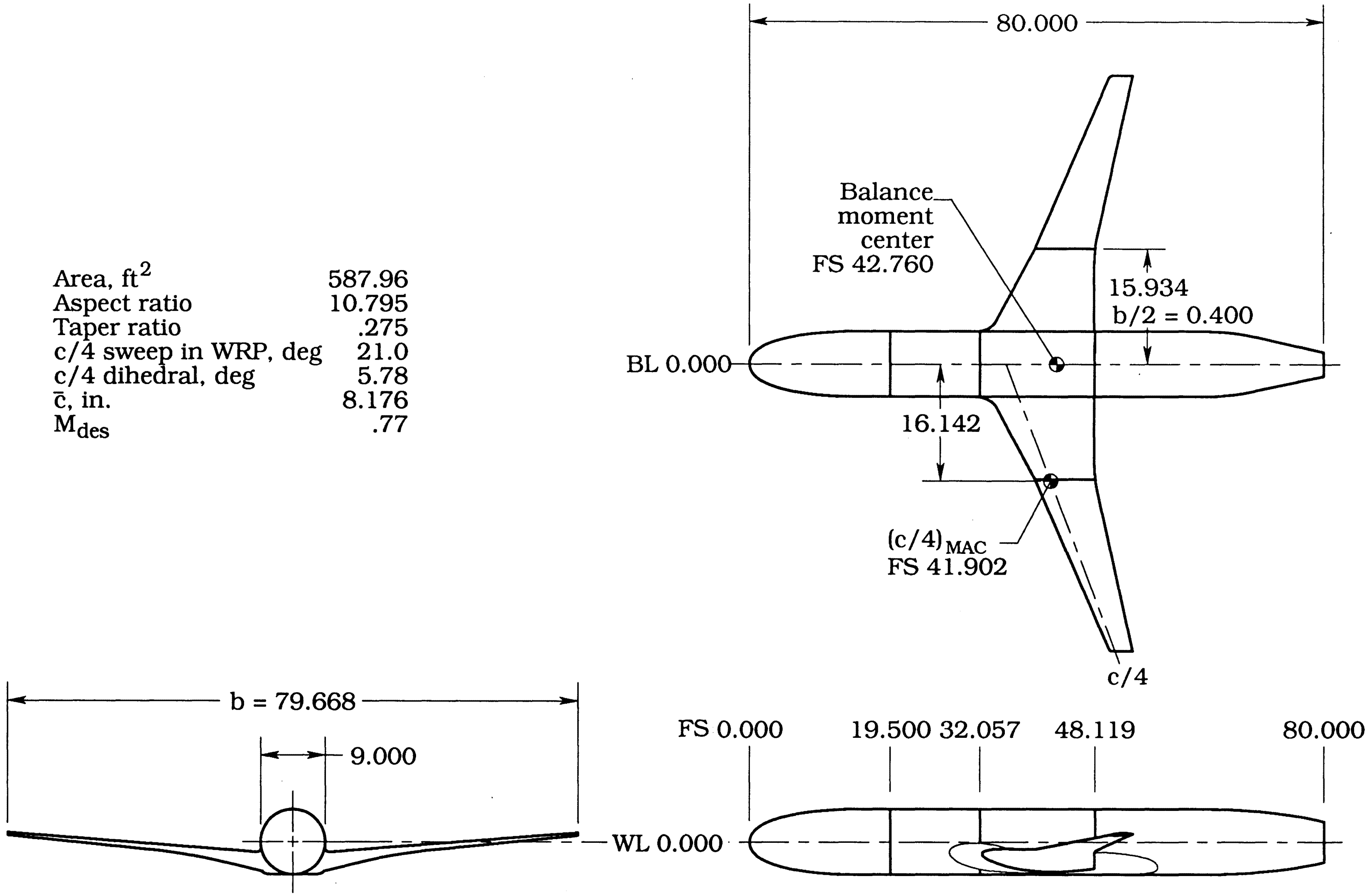

(a) General characteristics. Linear dimensions are in inches.

Figure 1. Basic low-wing transport model without nacelles.

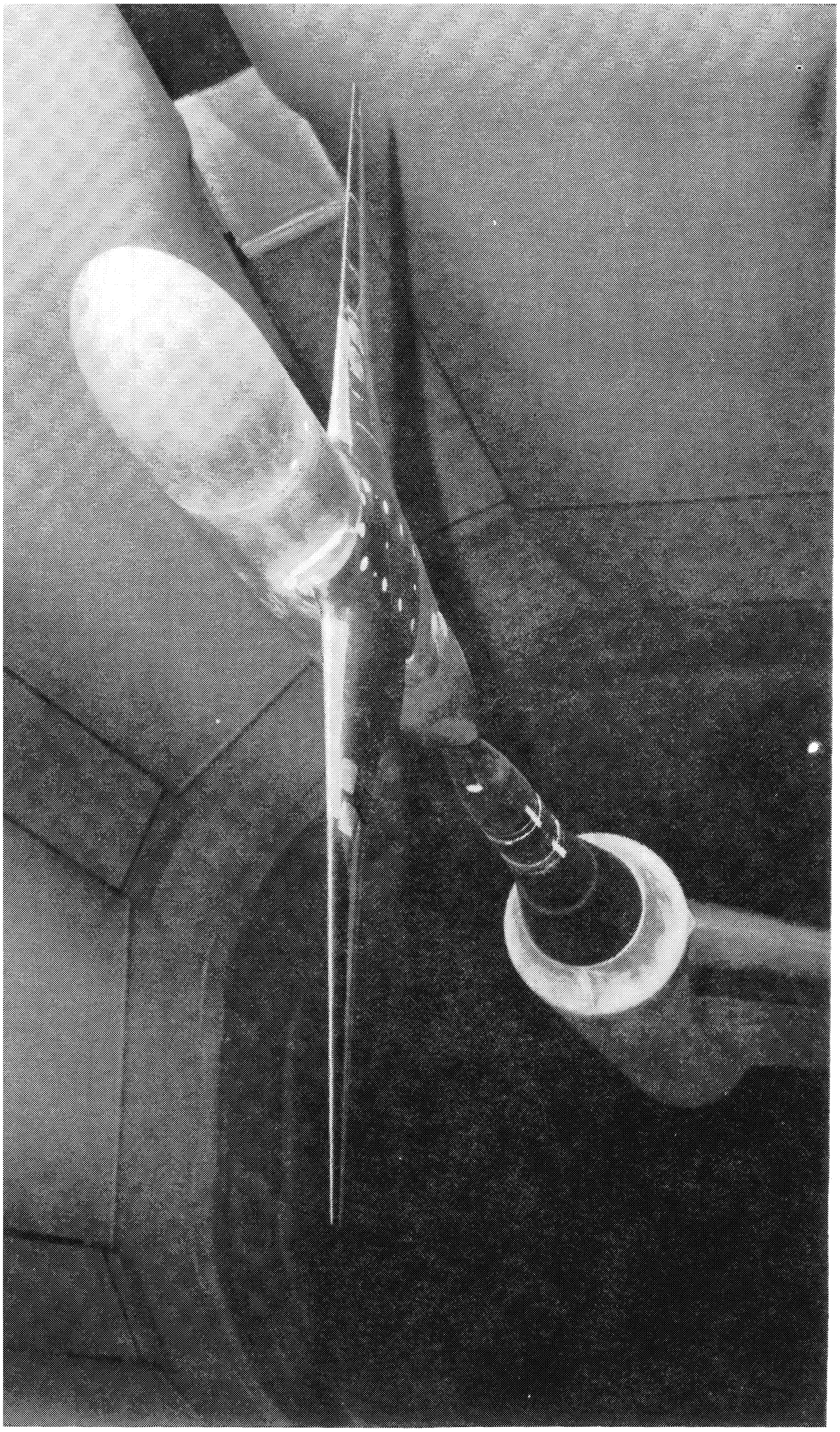

(b) Photograph of model without nacelles installed in Langley 16-Foot Transonic Tunnel.

Figure 1. Concluded.

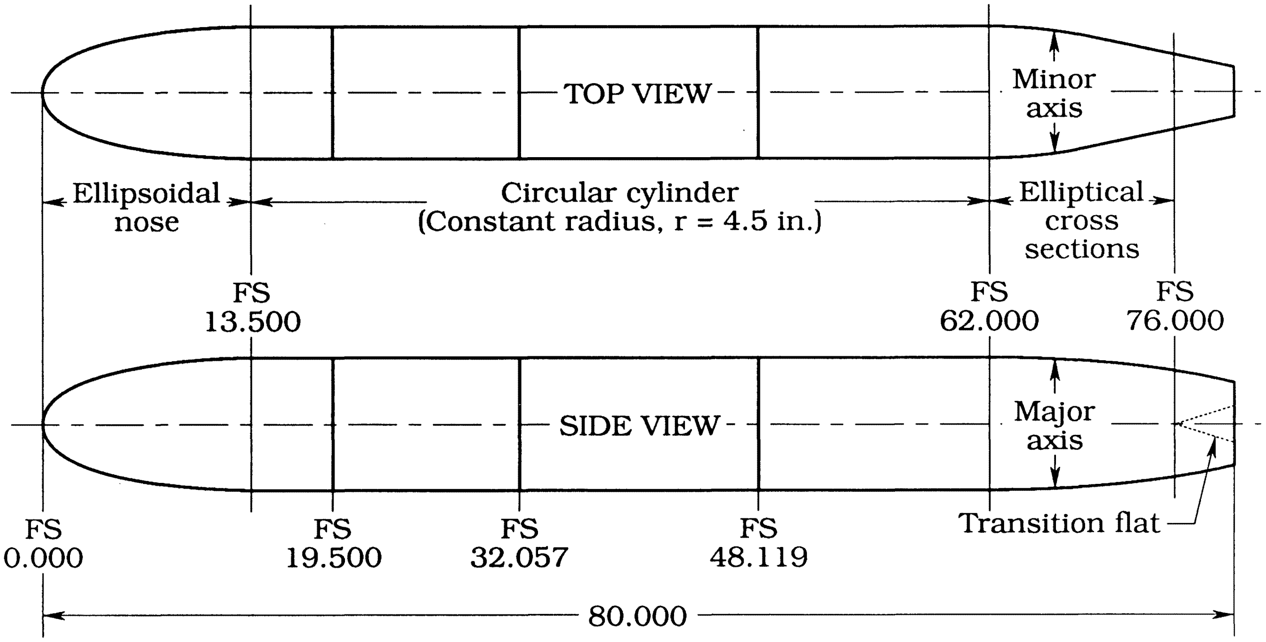

Ellipsoidal nose coordinates	
FS, in.	R, in.
0.000	0.000
0.100	0.547
0.200	0.772
0.250	0.862
0.375	1.053
0.500	1.213
0.750	1.480
1.000	1.700
1.250	1.891
1.500	2.062
2.000	2.357
2.500	2.609
3.500	3.023
4.500	3.354
5.500	3.625
6.500	3.848
7.500	4.031
9.500	4.298
11.500	4.450
13.500	4.500

Elliptical cross sections		
FS, in.	Major axis, in.	Minor axis, in.
62.000	9.000	9.000
63.000	8.990	8.957
64.000	8.958	8.828
65.000	8.906	8.612
65.500	8.873	8.470
66.000	8.834	8.307
66.102	8.825	8.271
66.500	8.789	8.131
67.000	8.740	7.955
67.500	8.685	7.778
68.000	8.625	7.602
68.500	8.600	7.426
69.000	8.490	7.249
69.500	8.414	7.073
70.000	8.333	6.897
70.500	8.247	6.720
71.000	8.156	6.544
71.500	8.059	6.368
72.000	7.958	6.191
72.500	7.850	6.015
73.000	7.738	5.839
73.500	7.620	5.662
74.000	7.497	5.486
74.500	7.369	5.310
75.000	7.235	5.133
75.500	7.096	4.957
76.000	6.951	4.781

(a) Overall dimensions and cross-section descriptions.

Figure 2. Fuselage geometry. Linear dimensions are in inches.

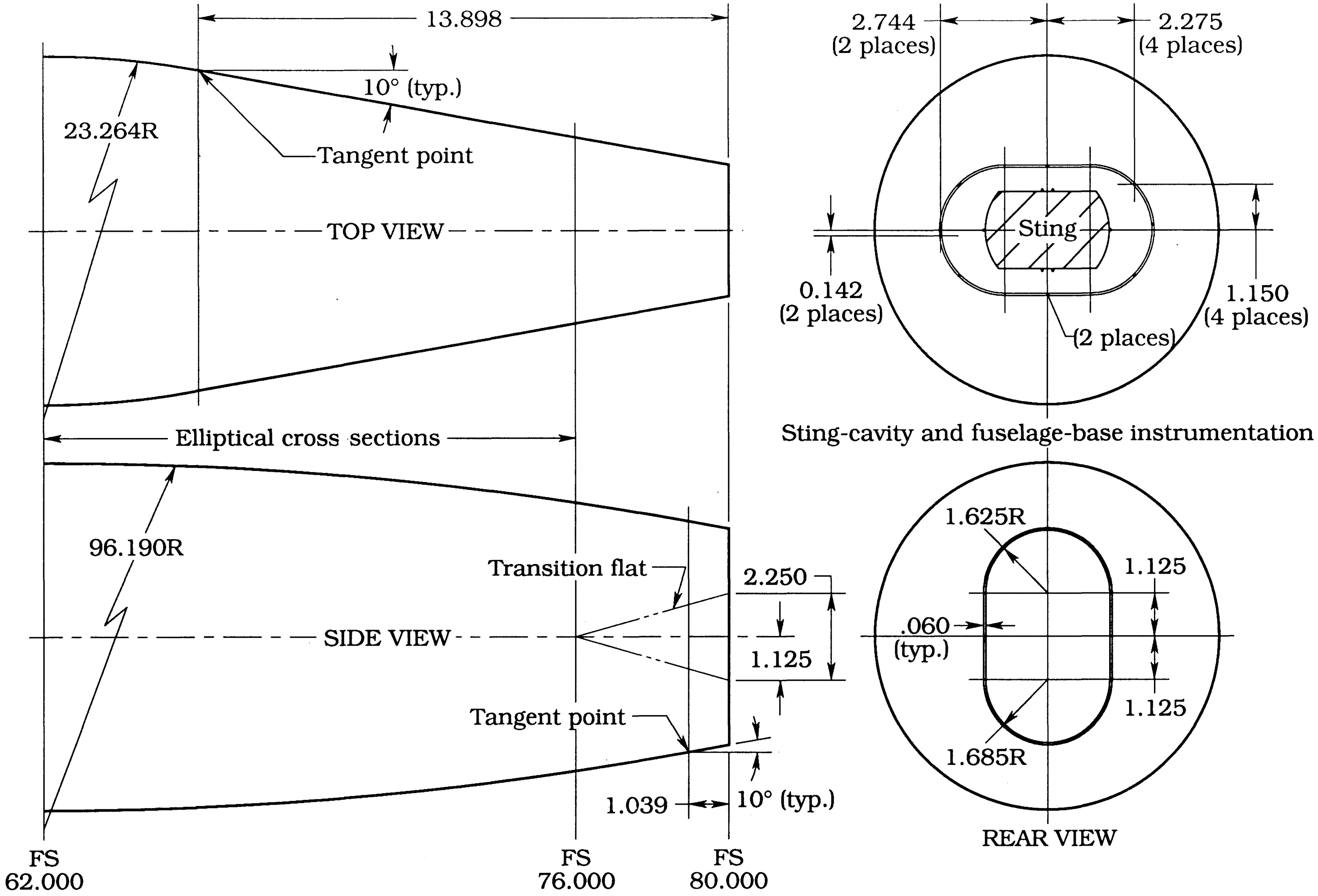

(b) Details of afterbody, sting cavity, and base.

Figure 2. Concluded.

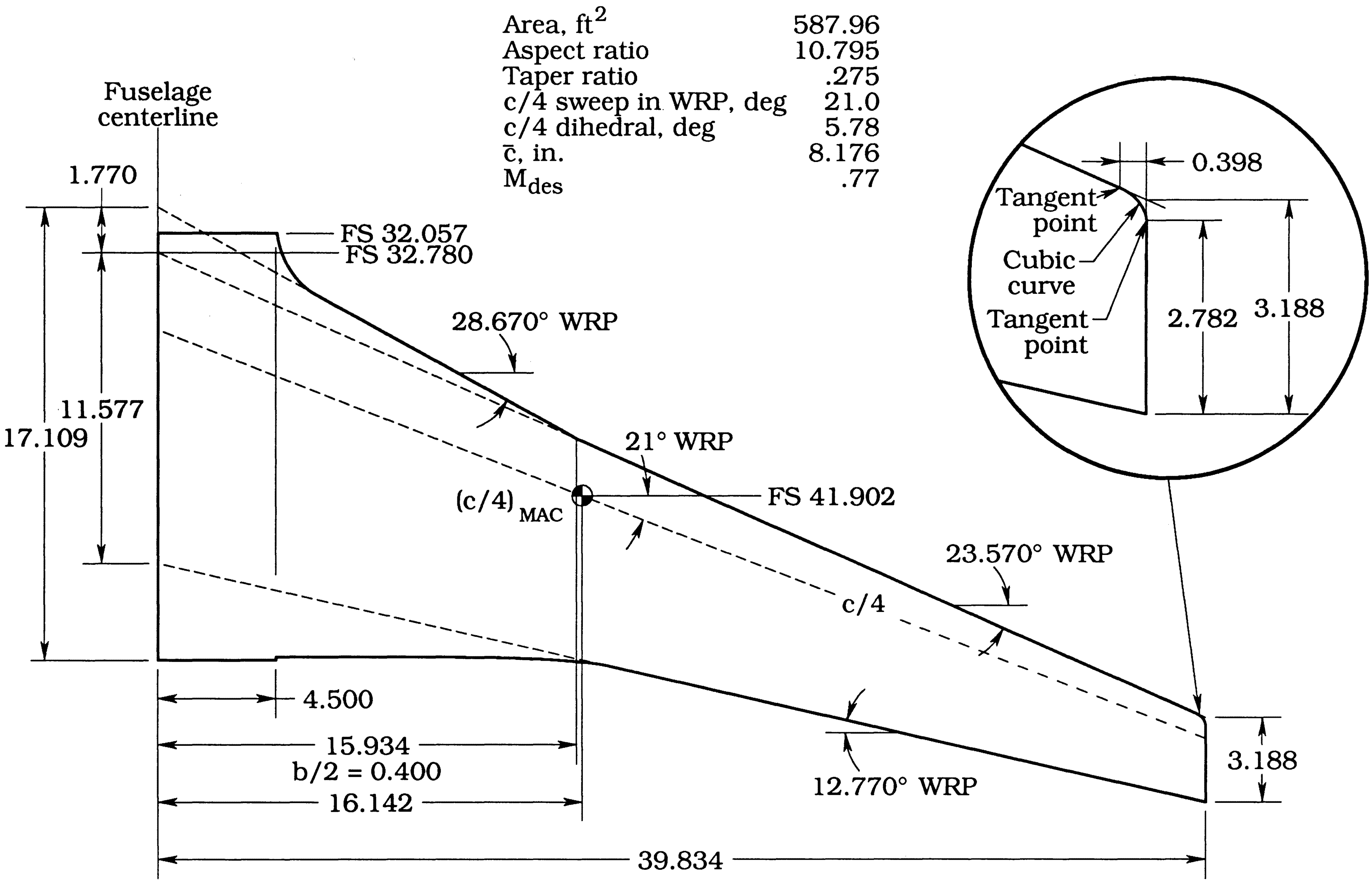

Area, ft^2	587.96
Aspect ratio	10.795
Taper ratio	.275
c/4 sweep in WRP, deg	21.0
c/4 dihedral, deg	5.78
$\bar{c}$, in.	8.176
M_{des}	.77

(a) Planform geometry.

Figure 3. Details of wing geometry. Linear dimensions are in inches.

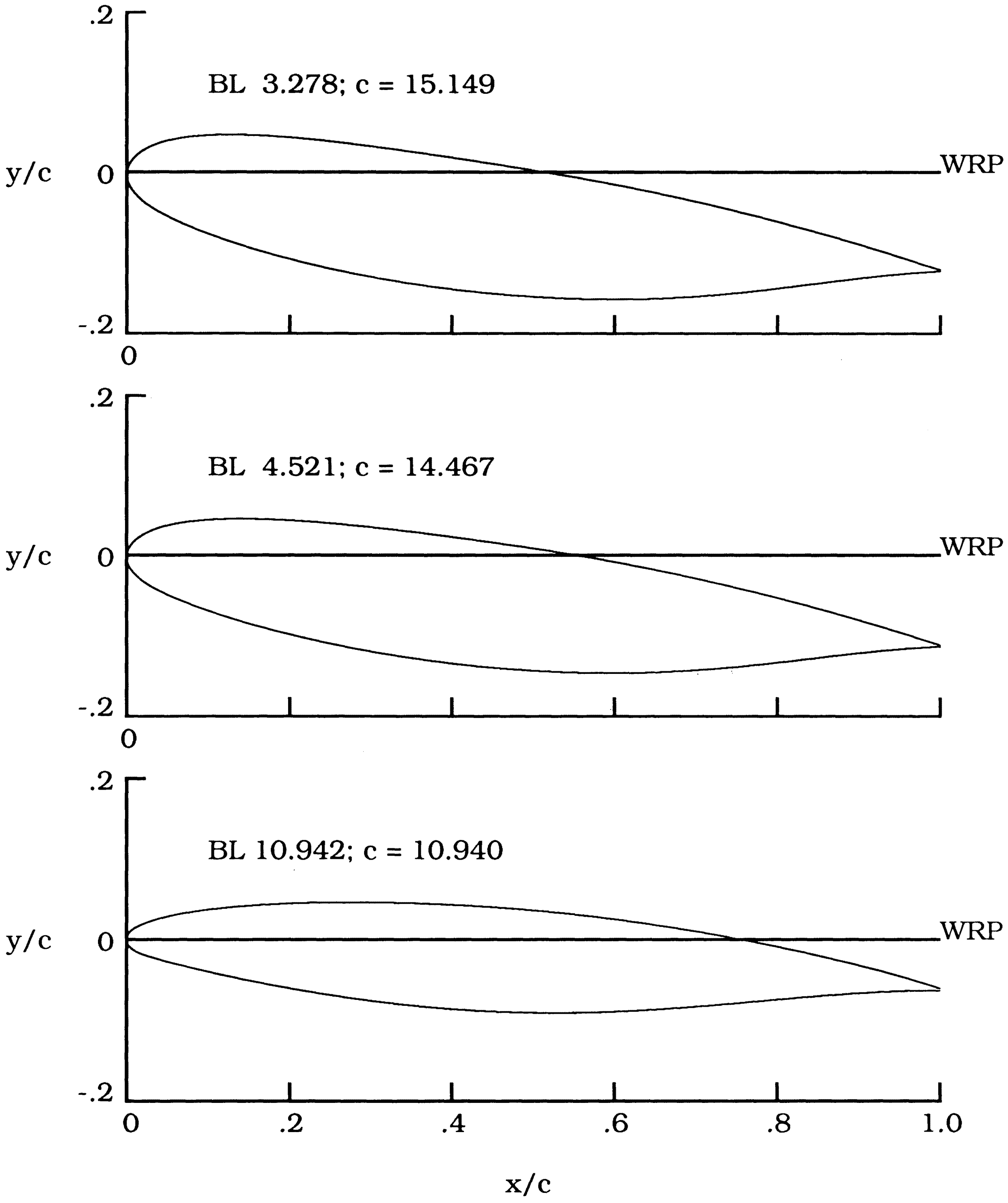

(b) Representative airfoil sections.

Figure 3. Continued.

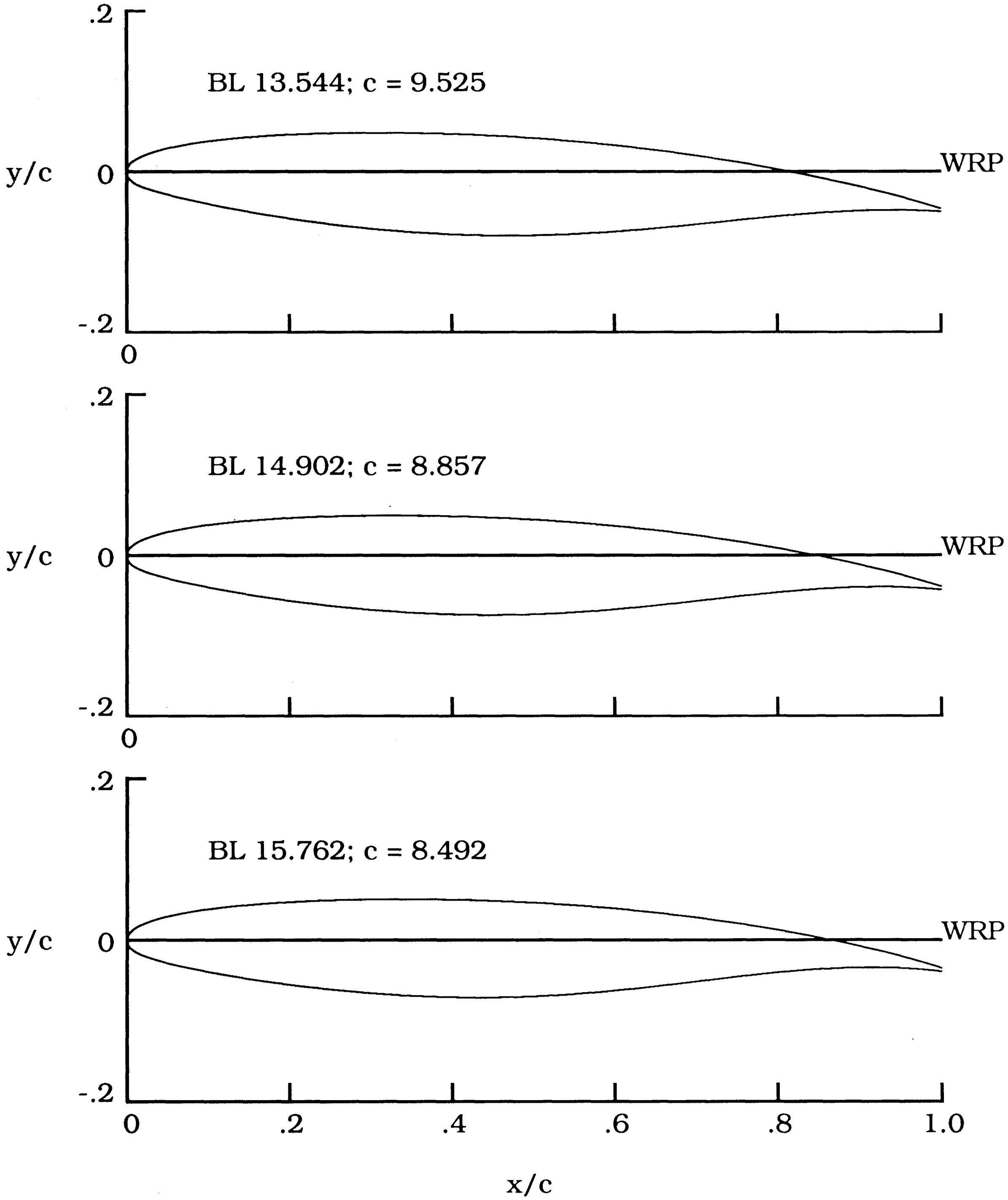

(b) Continued.

Figure 3. Continued.

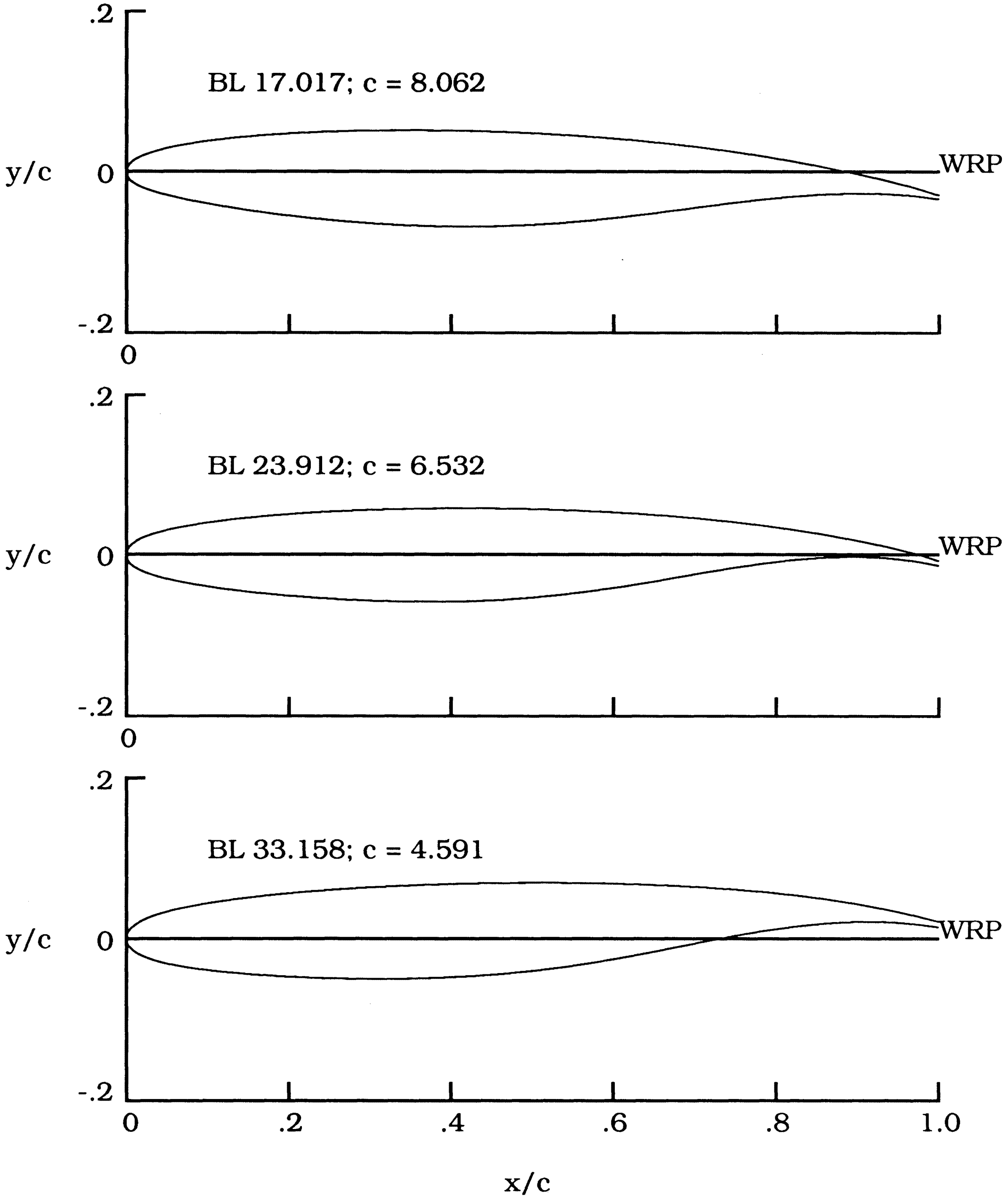

(b) Continued.

Figure 3. Continued.

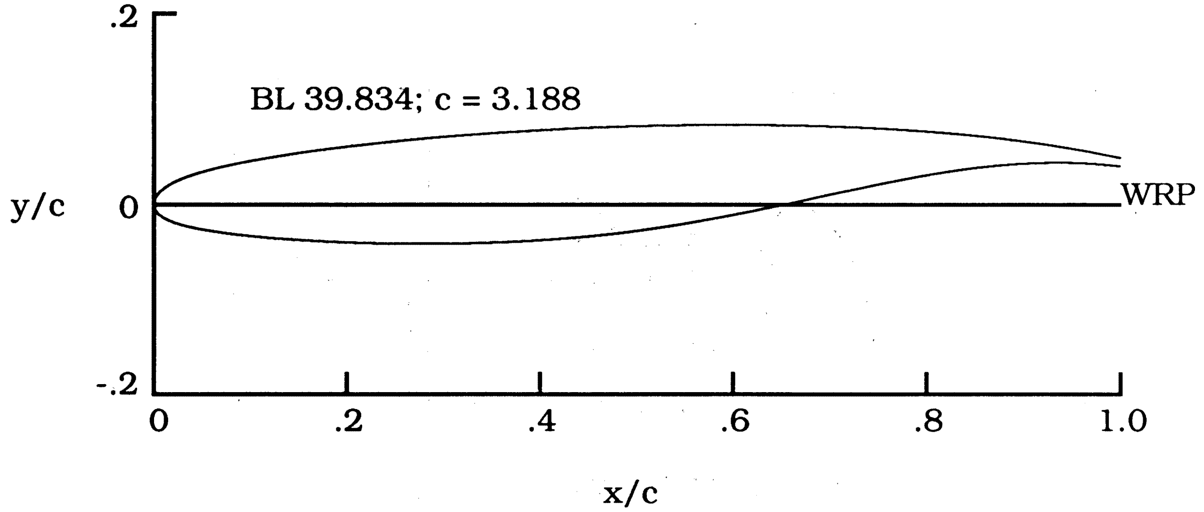

(b) Concluded.

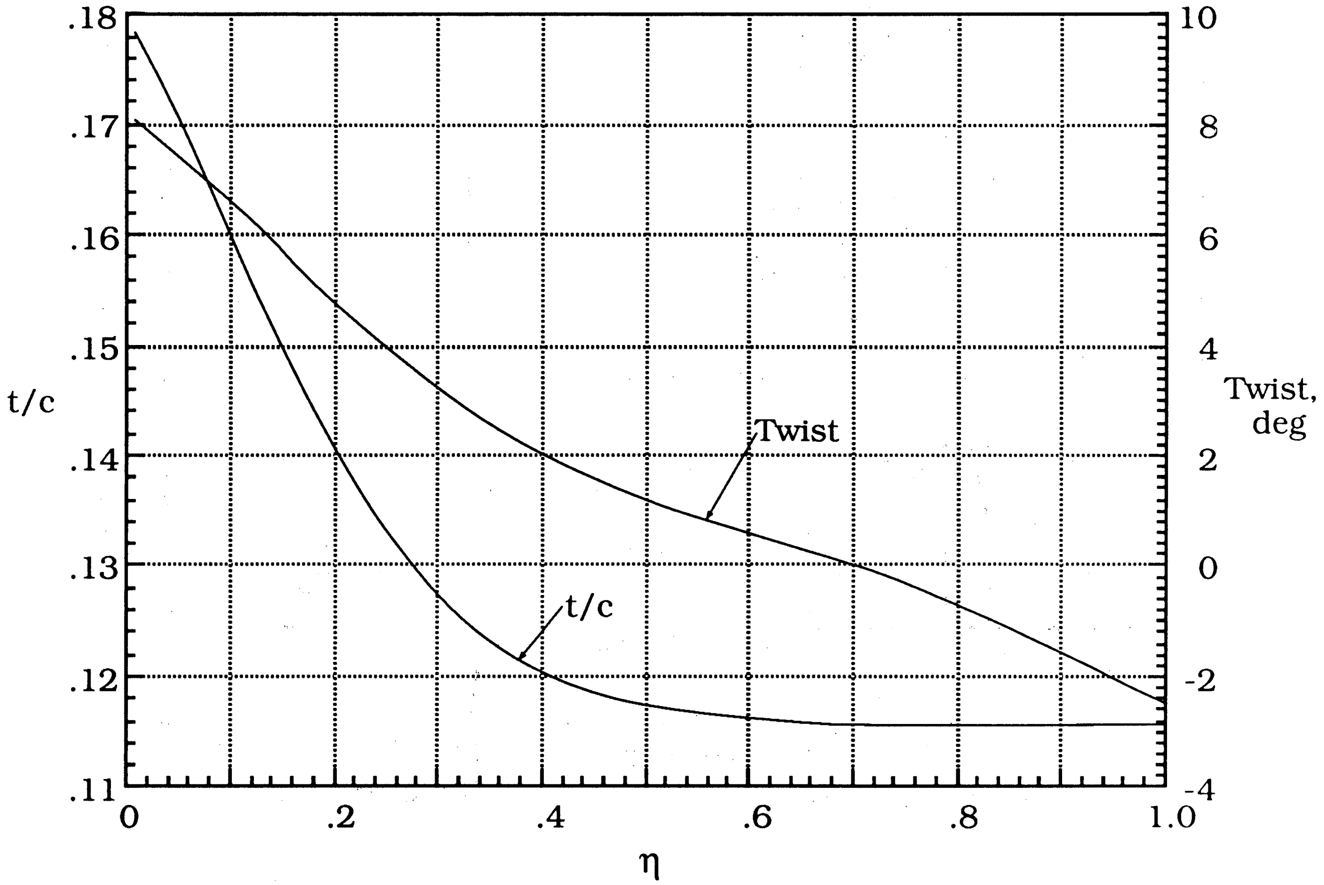

(c) Distributions of wing twist and airfoil maximum thickness ratio.

Figure 3. Concluded.

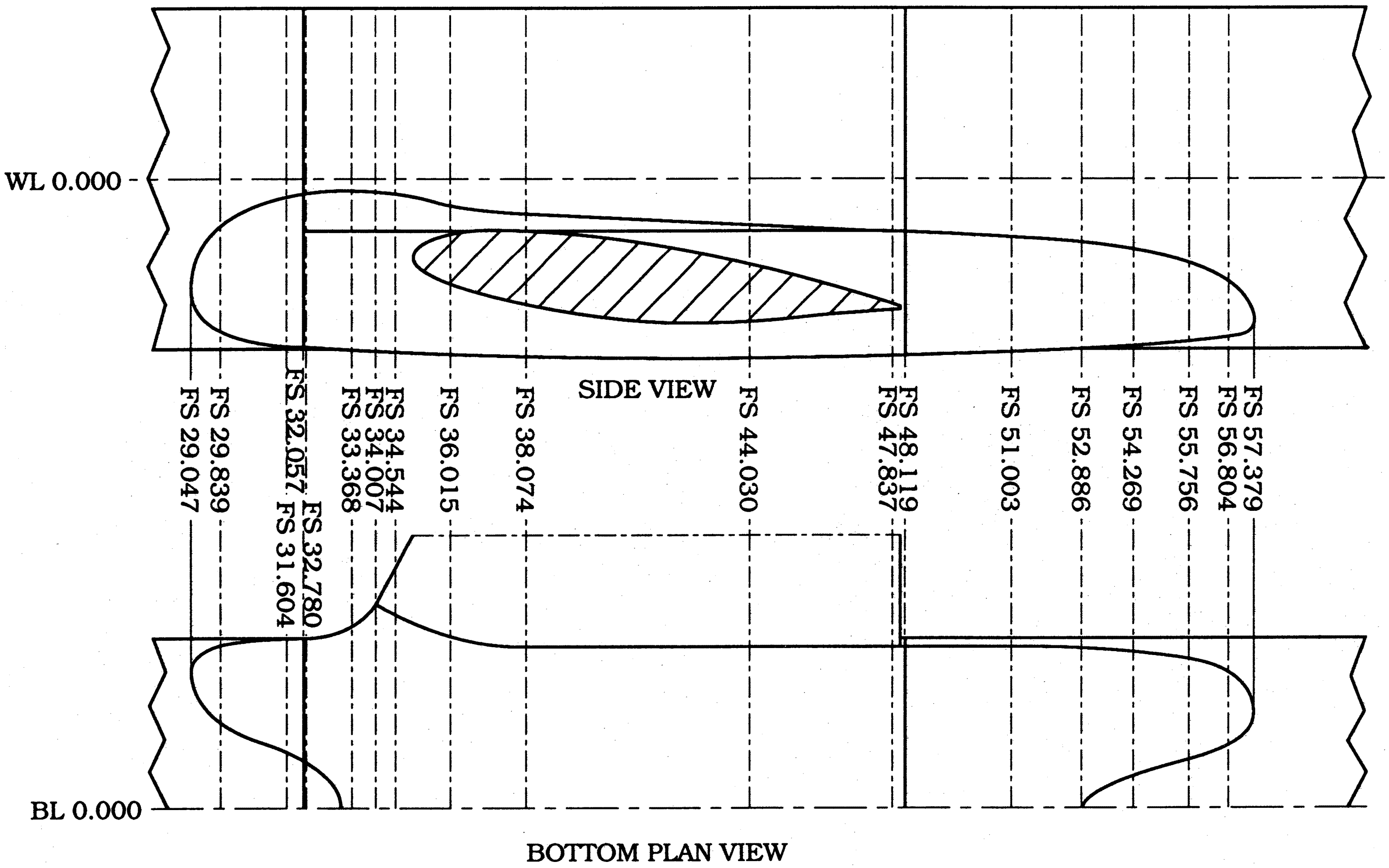

(a) Plan view and side view of fillet with important dimensions and cross-section locations.

Figure 4. Details of wing-fuselage fillet. Linear dimensions are in inches.

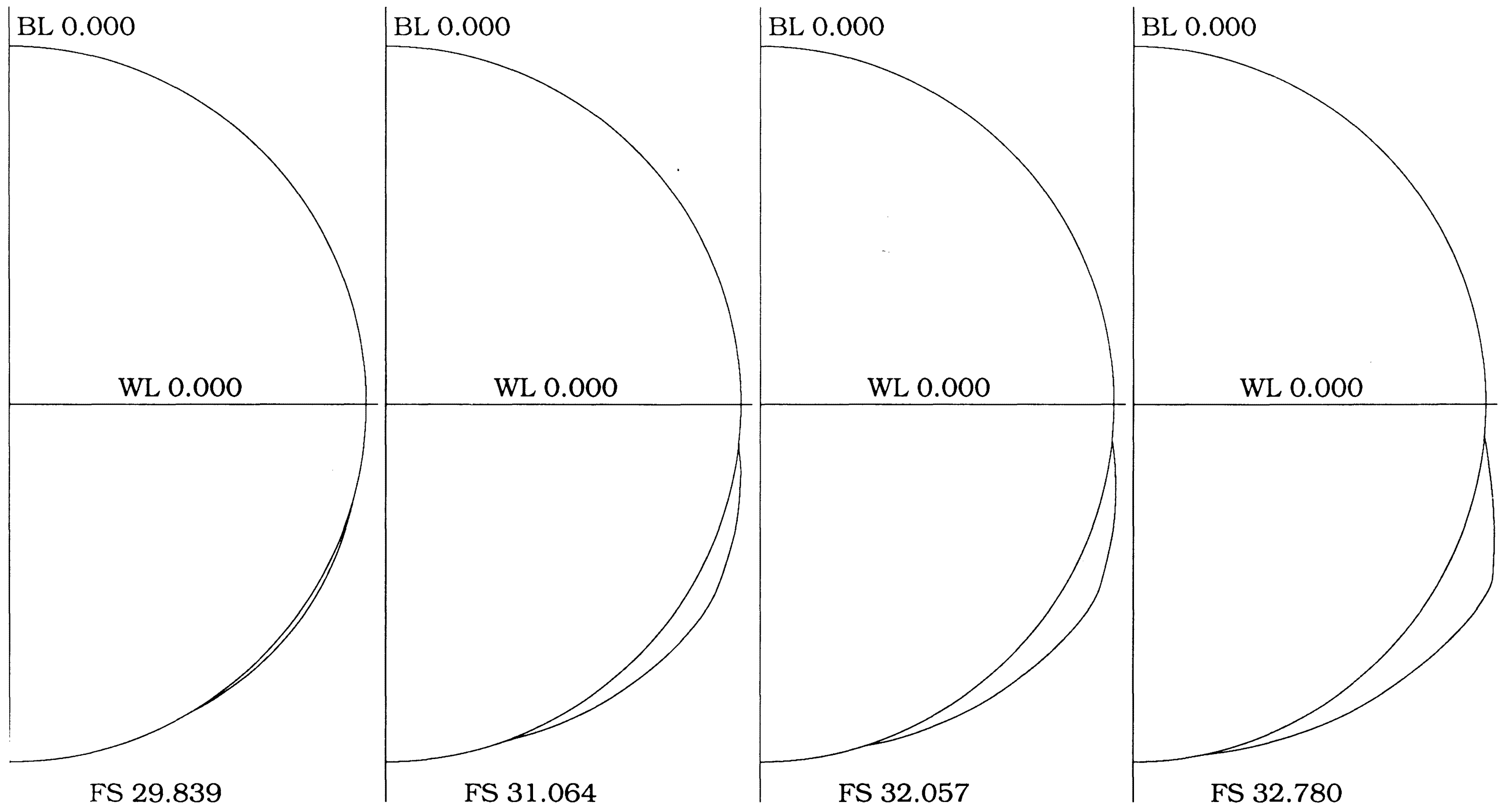

(b) Leading-edge and midchord wing-fuselage fillet cross sections to FS 44.030.

Figure 4. Continued.

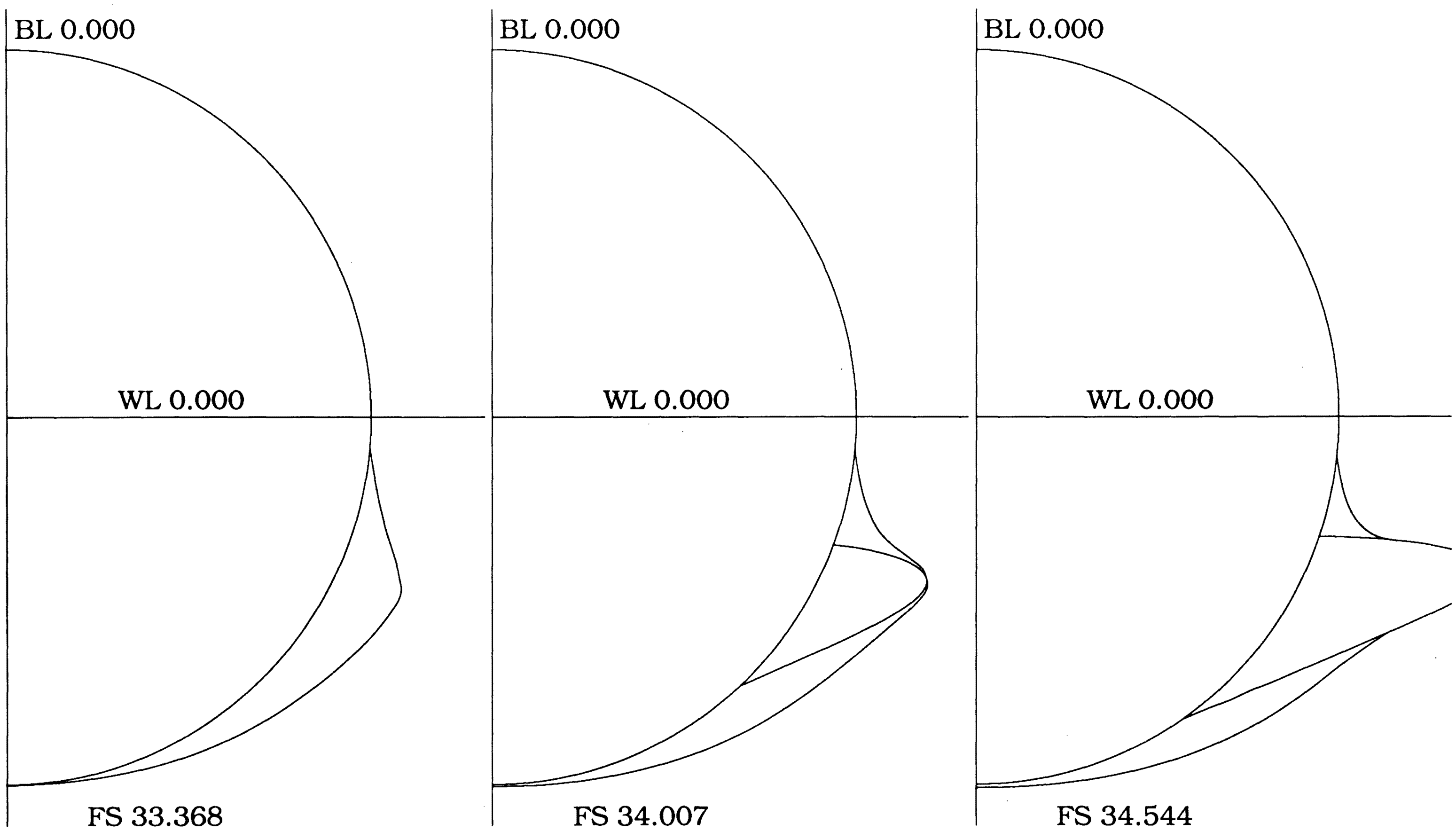

(b) Continued.

Figure 4. Continued.

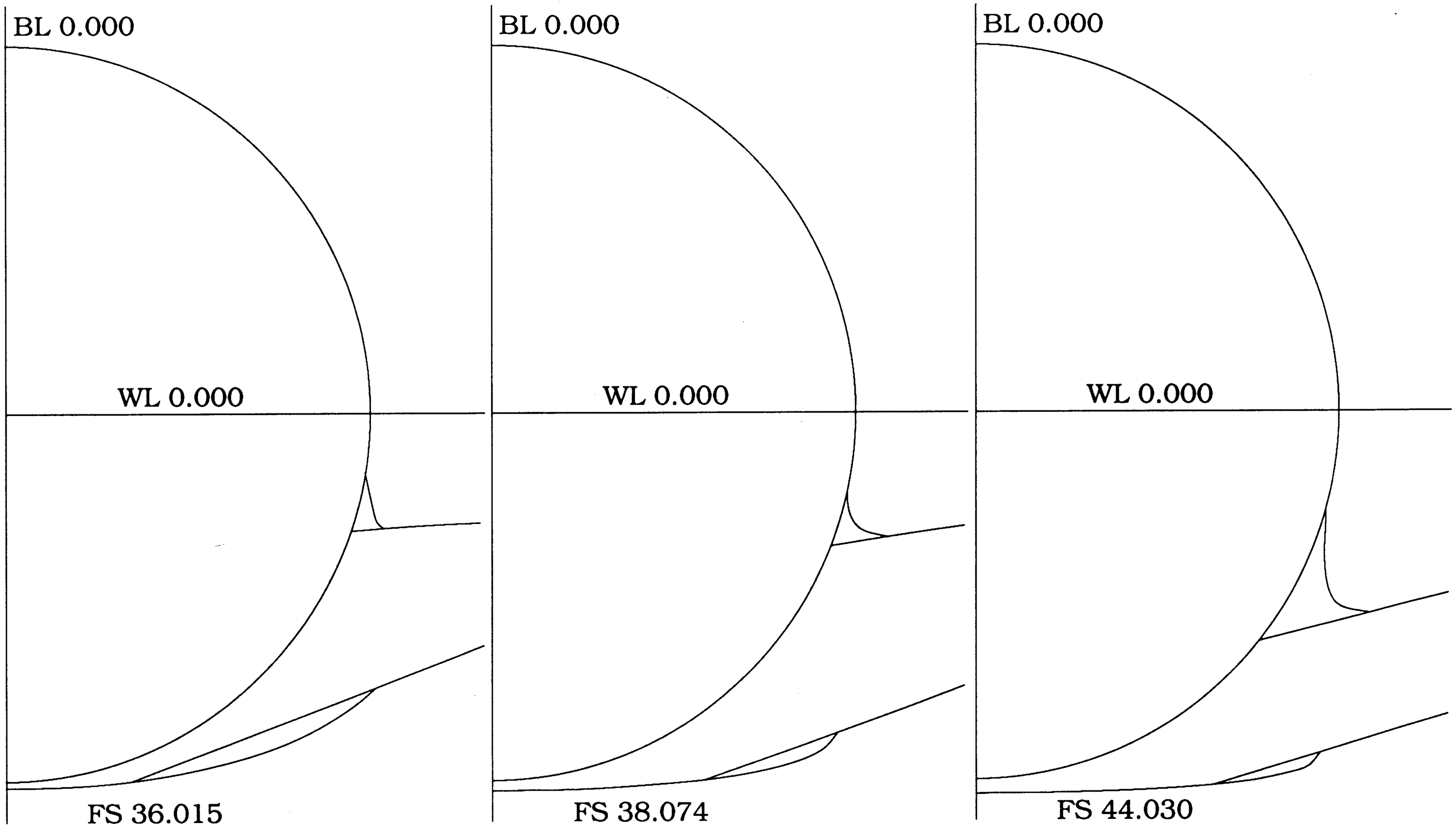

(b) Concluded.

Figure 4. Continued.

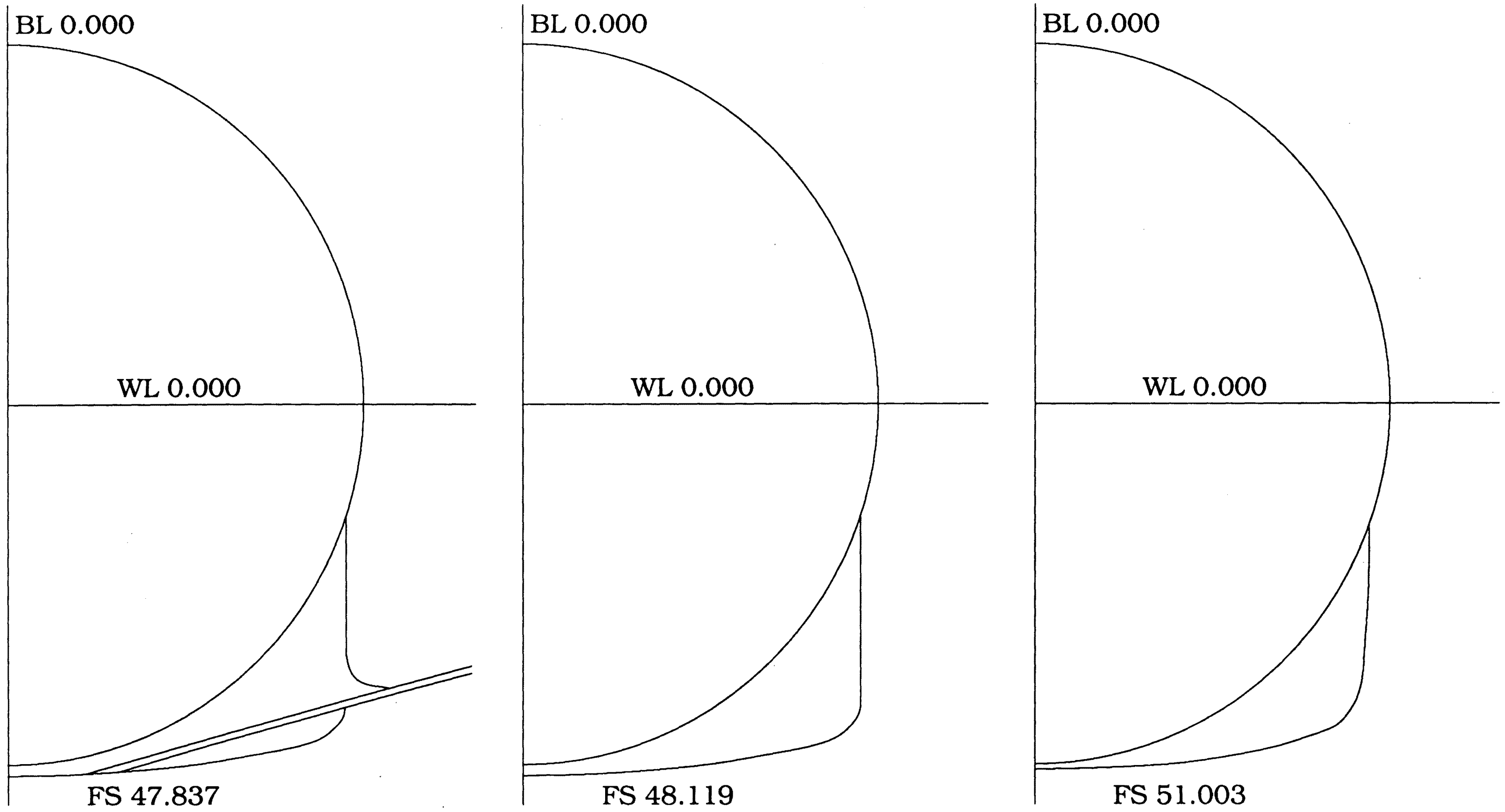

(c) Trailing-edge and wing-fuselage fillet cross sections from FS 47.837 to end of fillet at FS 57.837.

Figure 4. Continued.

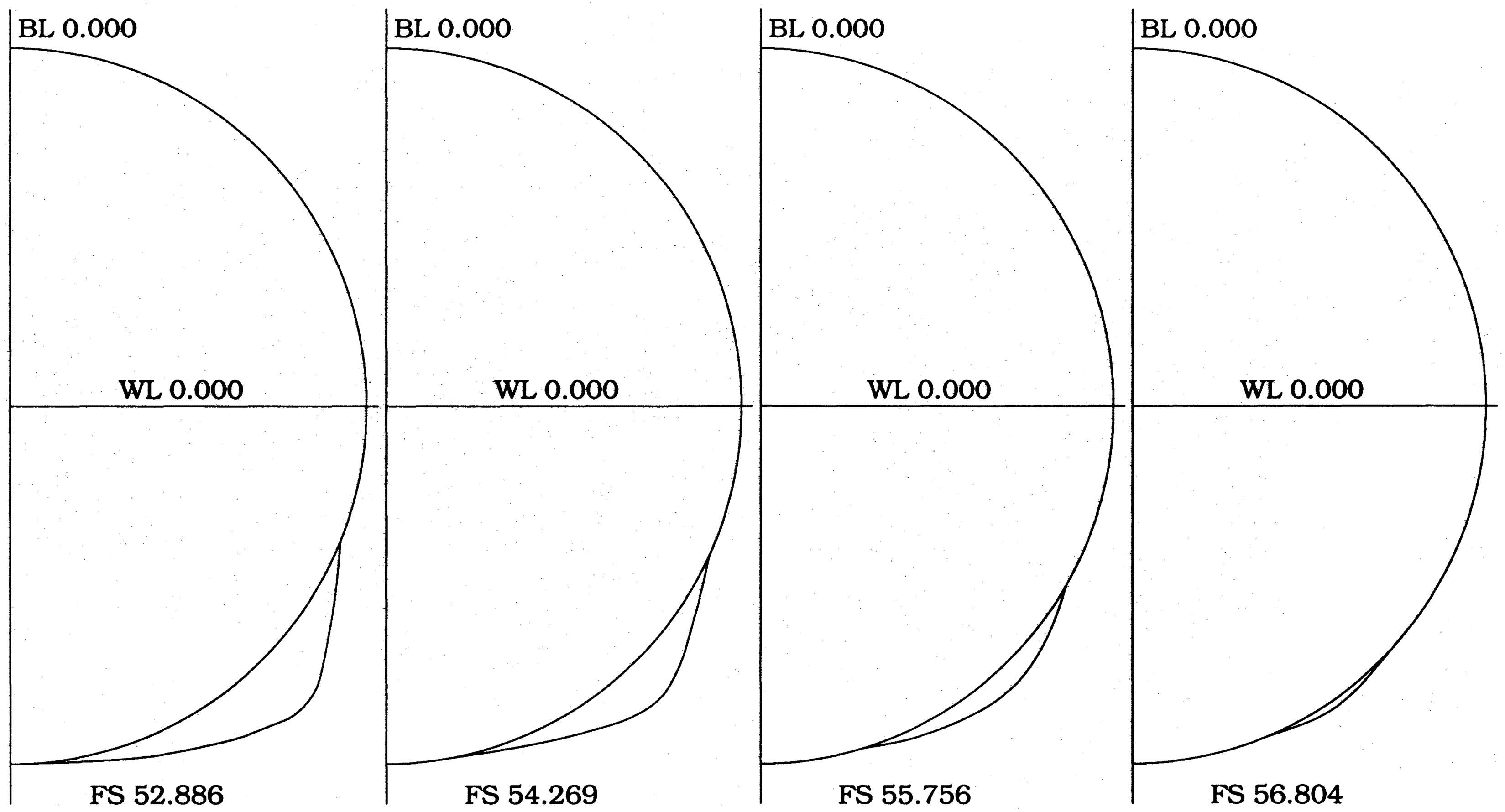

(c) Concluded.

Figure 4. Concluded.

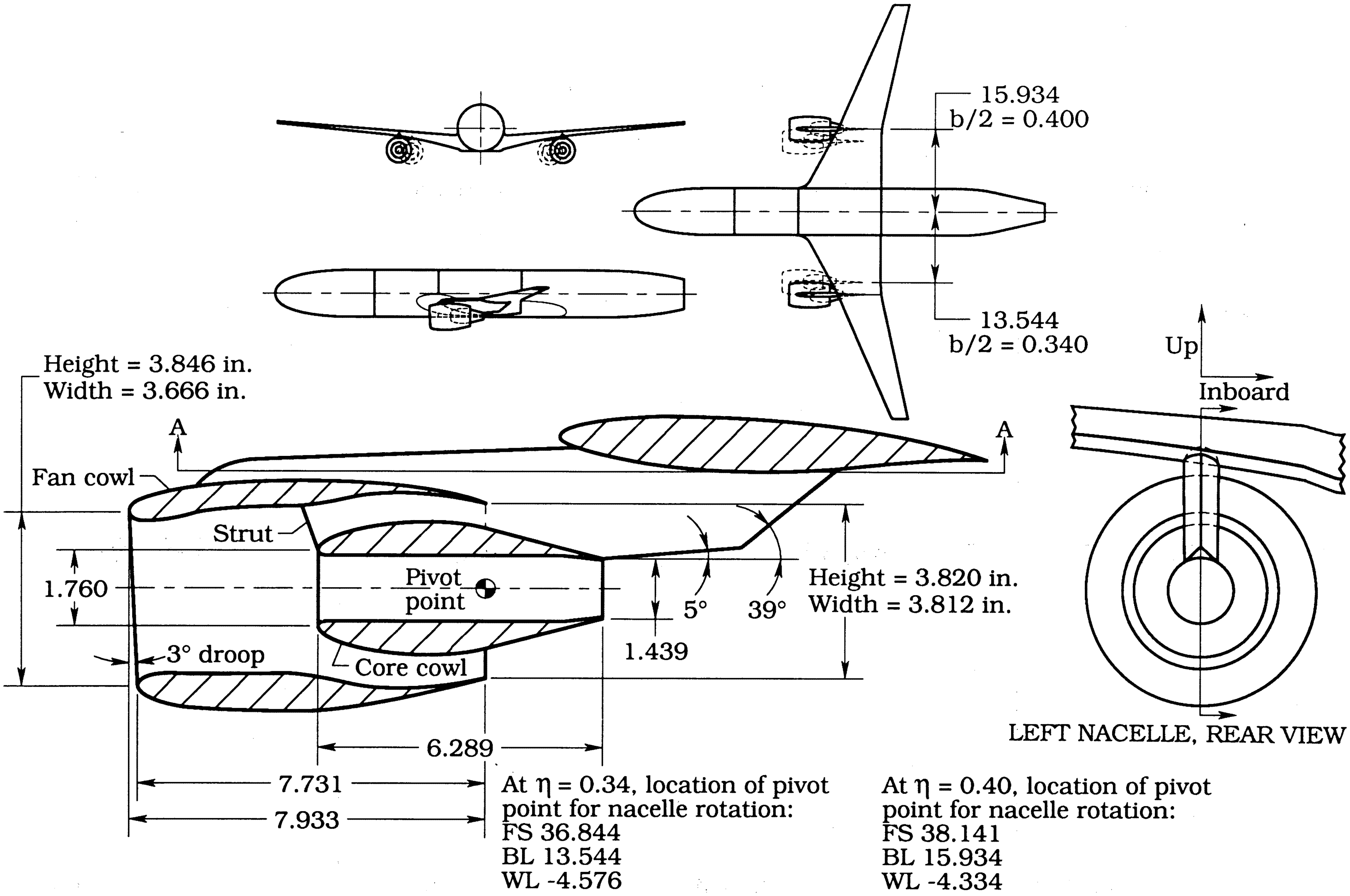

(a) Sketches of nacelle and installed locations on model.

Figure 5. Details of ATF nacelle. Linear dimensions are in inches.

Inboard and outboard sides of pylon			
x/c	y/c	x/c	y/c
0.000000	0.000000	0.422080	0.030137
0.000064	0.000941	0.471373	0.030189
0.000955	0.003877	0.635685	0.030310
0.002624	0.006460	0.717840	0.030169
0.006909	0.010389	0.791466	0.029867
0.015288	0.014993	0.804857	0.029789
0.029466	0.019523	0.815159	0.029596
0.039383	0.021341	0.854253	0.027599
0.049415	0.022279	0.886446	0.024056
0.200266	0.026964	0.932238	0.015677
0.298847	0.028967	0.968059	0.007732
0.372786	0.029865	1.000000	0.000142

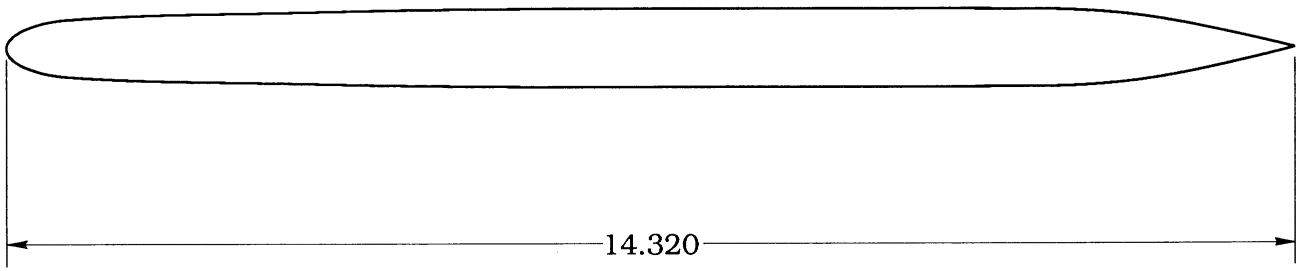

SECTION A-A

At 34-percent span station, WL -1.963
At 40-percent span station, WL -1.721

(b) Cross section of typical pylon airfoil.

Figure 5. Continued.

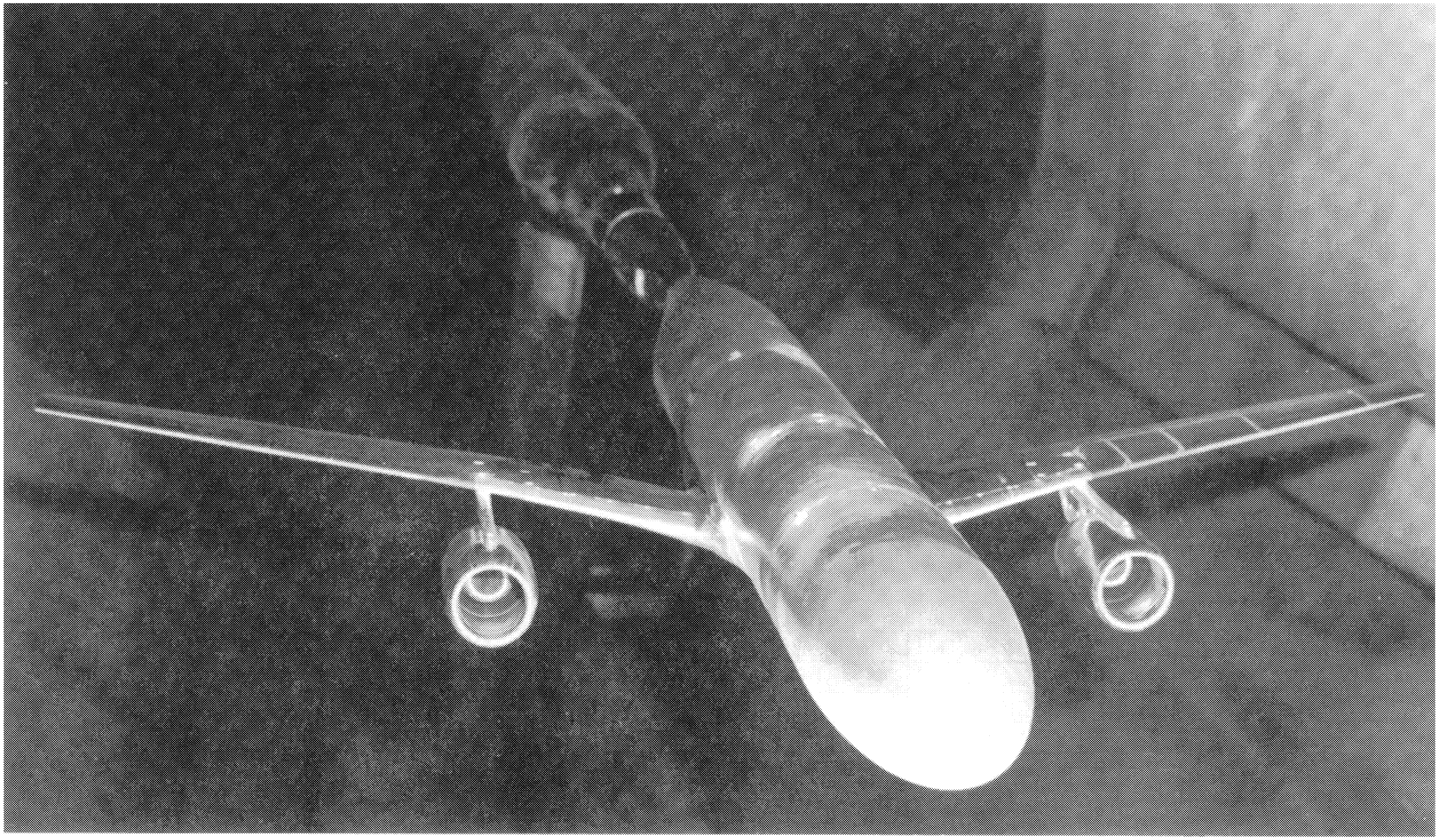

L-89-1610

(c) Photograph of model with ATF nacelles at $y/(b/2) = 0.40$ installed in Langley 16-Foot Transonic Tunnel.

Figure 5. Concluded.

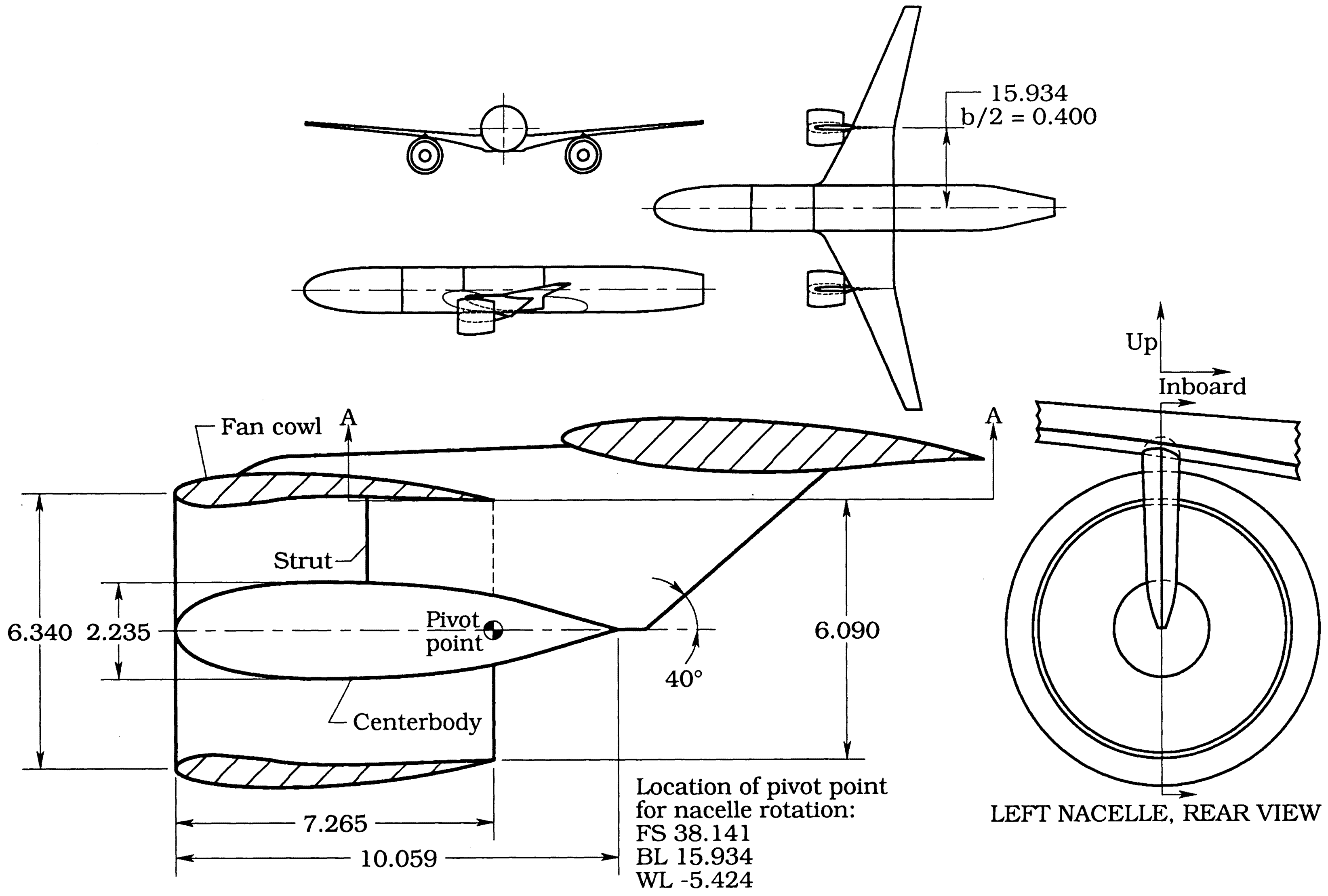

(a) Sketches of nacelle and installed location on model.

Figure 6. Details of SF-1 nacelle. Linear dimensions are in inches.

Inboard and outboard sides of pylon			
x/c	y/c	x/c	y/c
0.000000	0.000000	0.275145	0.043189
0.011055	0.015060	0.336399	0.043189
0.028394	0.023071	0.399593	0.043189
0.046714	0.028527	0.441730	0.043189
0.065402	0.032532	0.496128	0.043189
0.084273	0.035608	0.568109	0.041771
0.103247	0.037968	0.640091	0.038107
0.122282	0.039776	0.712073	0.032845
0.141348	0.041125	0.784055	0.026374
0.160444	0.042096	0.856036	0.018881
0.179551	0.042739	0.928018	0.010423
0.198668	0.043087	0.964014	0.005809
0.217784	0.043189	1.000000	0.000907

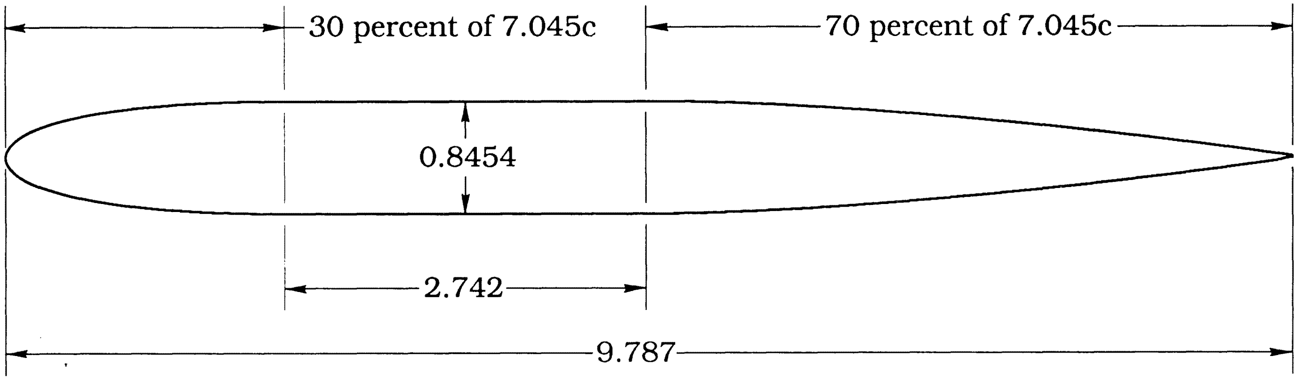

SECTION A-A

At 40-percent span station, WL -2.379

(b) Cross section of typical pylon airfoil.

Figure 6. Continued.

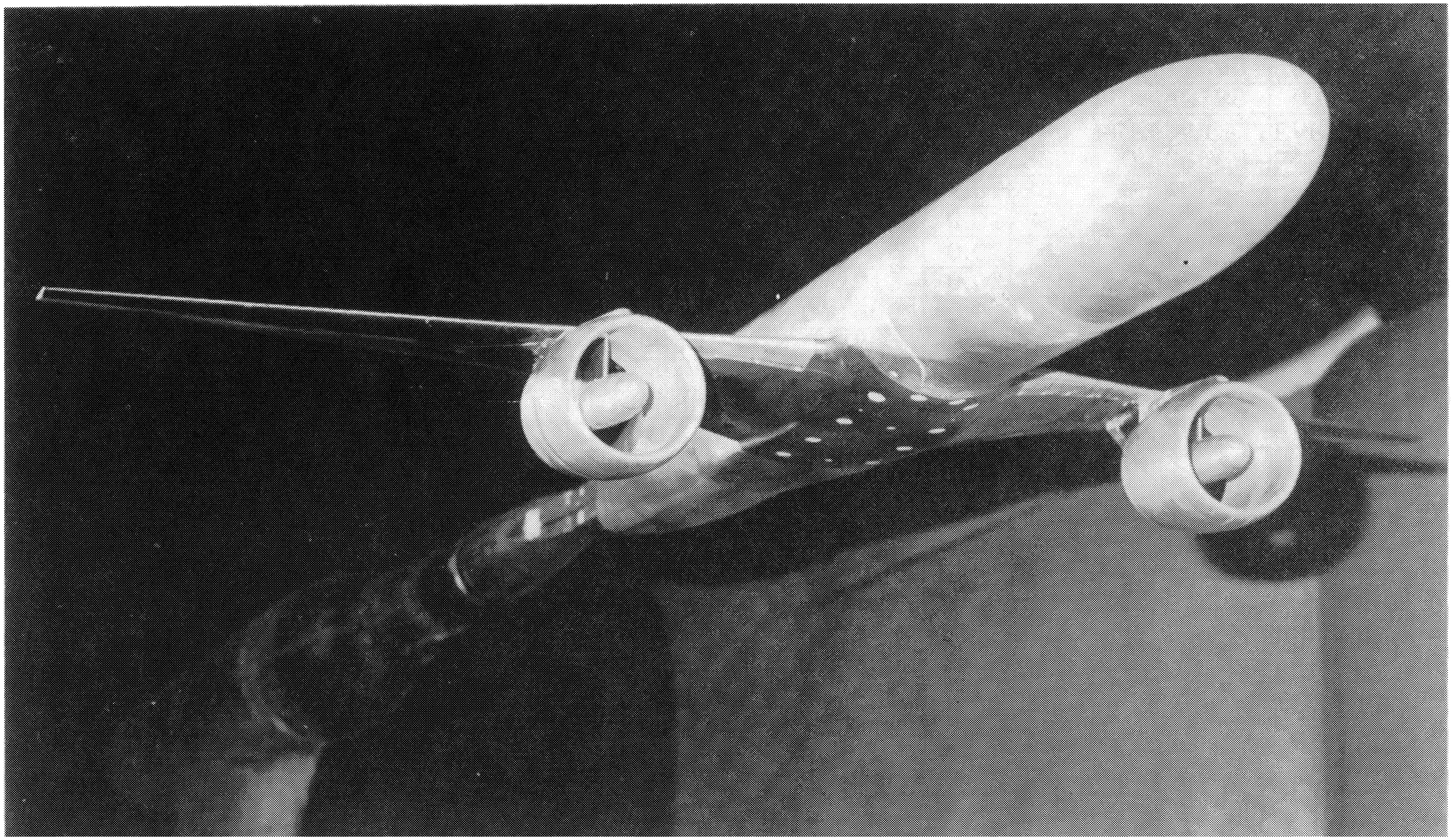

L-89-01629

(c) Photograph of model with SF-1 nacelles at $y/(b/2) = 0.40$ installed in Langley 16-Foot Transonic Tunnel.

Figure 6. Concluded.

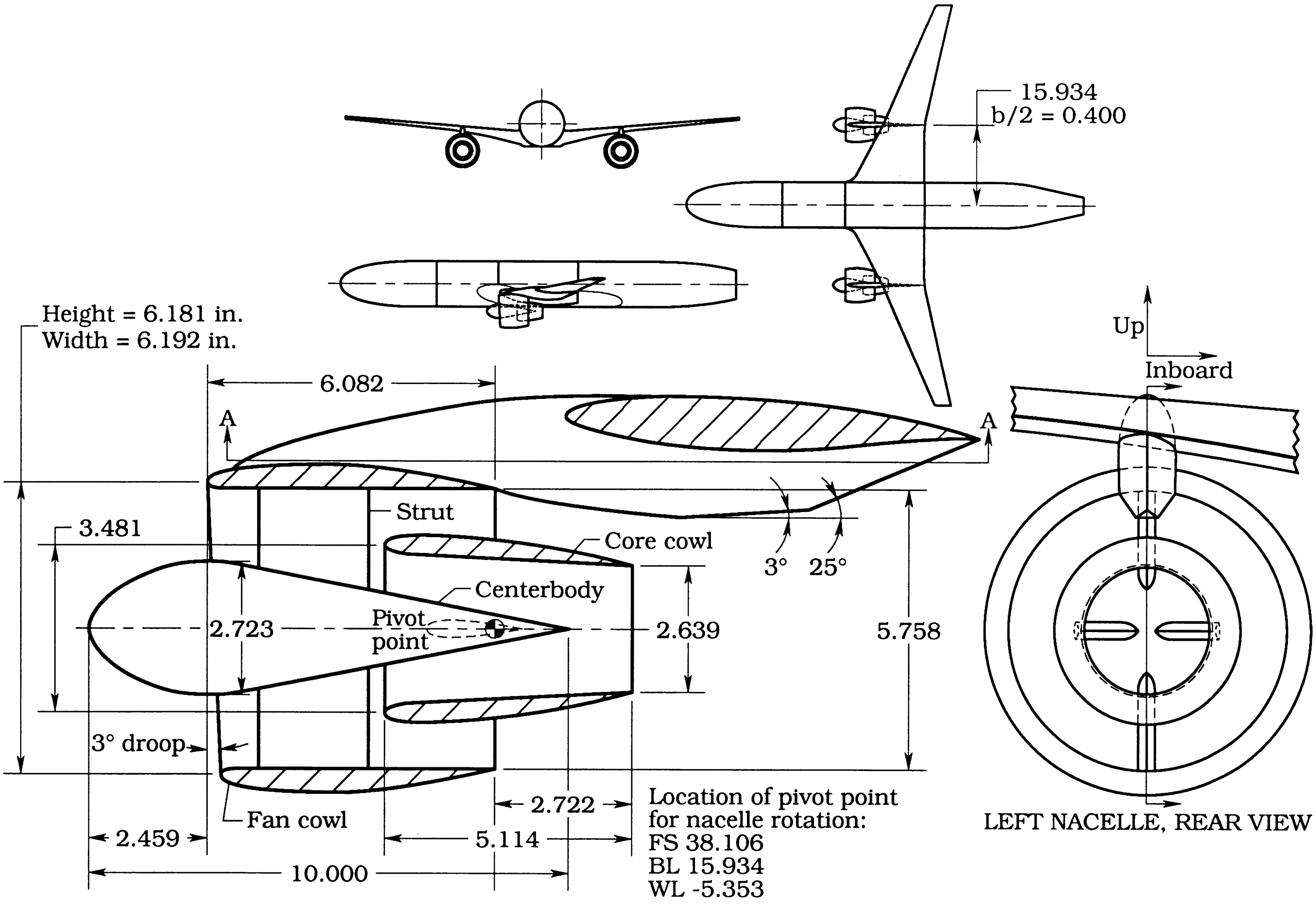

(a) Sketches of nacelle and installed location on model.

Figure 7. Details of SF-2 nacelles. Linear dimensions are in inches.

Inboard side of pylon			
x/c	y/c	x/c	y/c
0.000531	0.000000	0.429508	-0.037373
0.000910	-0.003144	0.447143	-0.037344
0.002132	-0.006696	0.464785	-0.037140
0.004541	-0.011310	0.506365	-0.037053
0.007576	-0.016012	0.519014	-0.036696
0.010466	-0.017649	0.530026	-0.036339
0.029476	-0.025350	0.586904	-0.034338
0.033253	-0.026470	0.644612	-0.032278
0.062861	-0.031638	0.694459	-0.031157
0.096180	-0.035168	0.744722	-0.027504
0.132839	-0.037336	0.792742	-0.022824
0.172308	-0.038414	0.836665	-0.017533
0.214150	-0.038661	0.877001	-0.012016
0.257804	-0.038479	0.915938	-0.006507
0.302790	-0.037962	0.956783	-0.000793
0.348452	-0.037489	1.000000	0.006128

Outboard side of pylon			
x/c	y/c	x/c	y/c
0.000000	0.000000	0.417390	0.049382
0.000356	0.003130	0.442128	0.050131
0.001521	0.006696	0.491590	0.050139
0.003792	0.011332	0.534669	0.049811
0.006768	0.016237	0.545644	0.049505
0.009374	0.017831	0.555994	0.049171
0.028006	0.026143	0.567609	0.048683
0.032213	0.027533	0.622908	0.046252
0.061660	0.033683	0.678178	0.043625
0.094855	0.038392	0.721293	0.041398
0.131420	0.041885	0.764925	0.037861
0.170831	0.044367	0.807124	0.033632
0.212585	0.045990	0.846374	0.028923
0.256312	0.047067	0.883143	0.024032
0.301297	0.047649	0.919301	0.019112
0.346953	0.048123	0.957882	0.013952
0.392761	0.048523	1.000000	0.007584

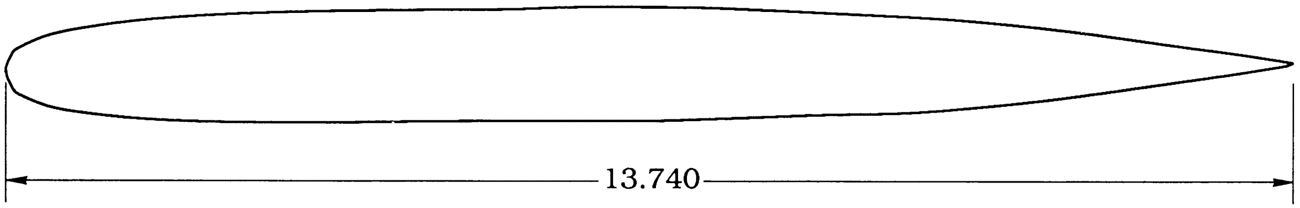

SECTION A-A
At 40-percent span station, WL -1.970

(b) Cross section of typical pylon airfoil.

Figure 7. Continued.

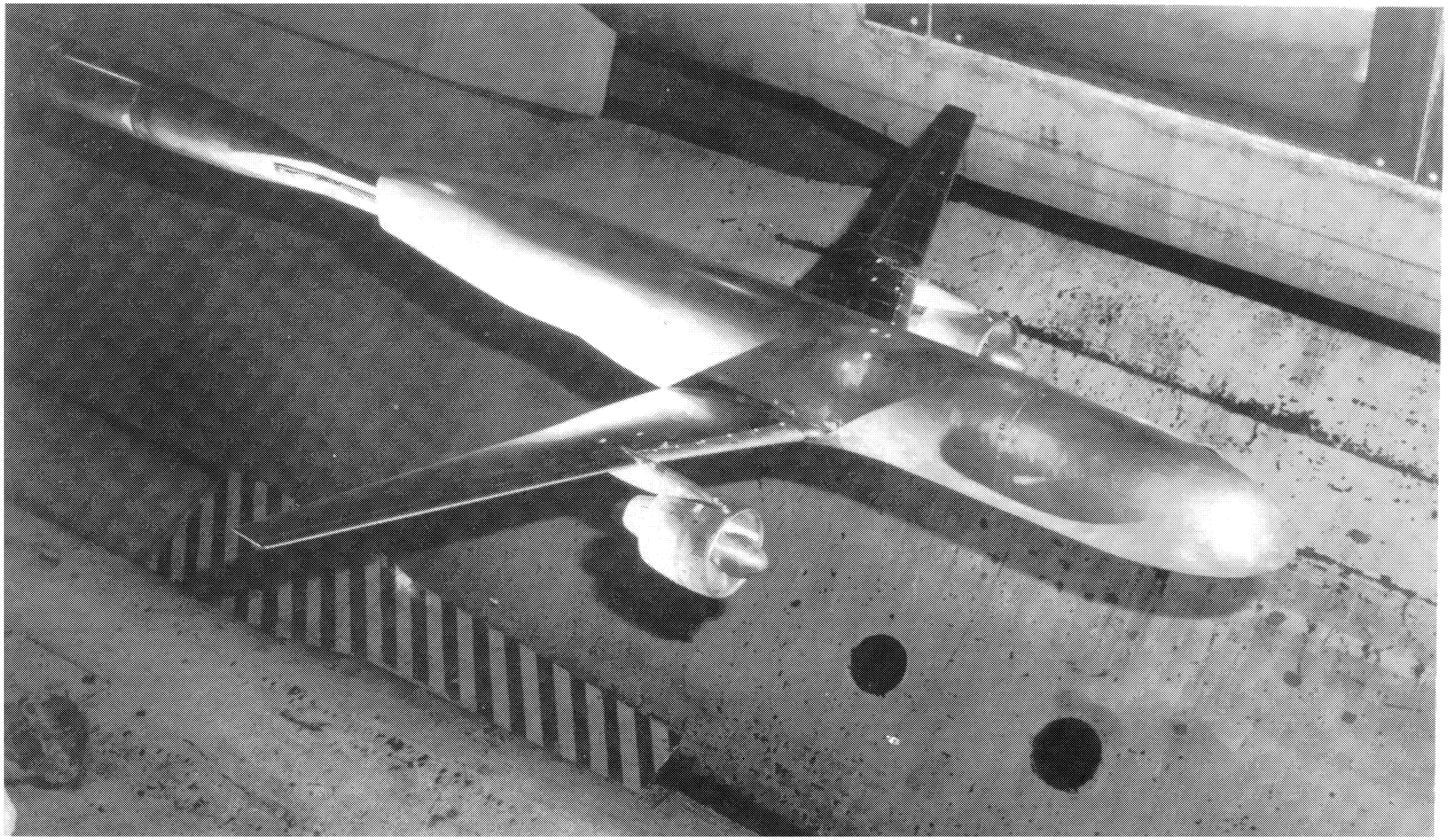

L-89-3318

(c) Photograph of model with SF-2 nacelles at $y/(b/2) = 0.40$ installed in Langley 16-Foot Transonic Tunnel.

Figure 7. Concluded.

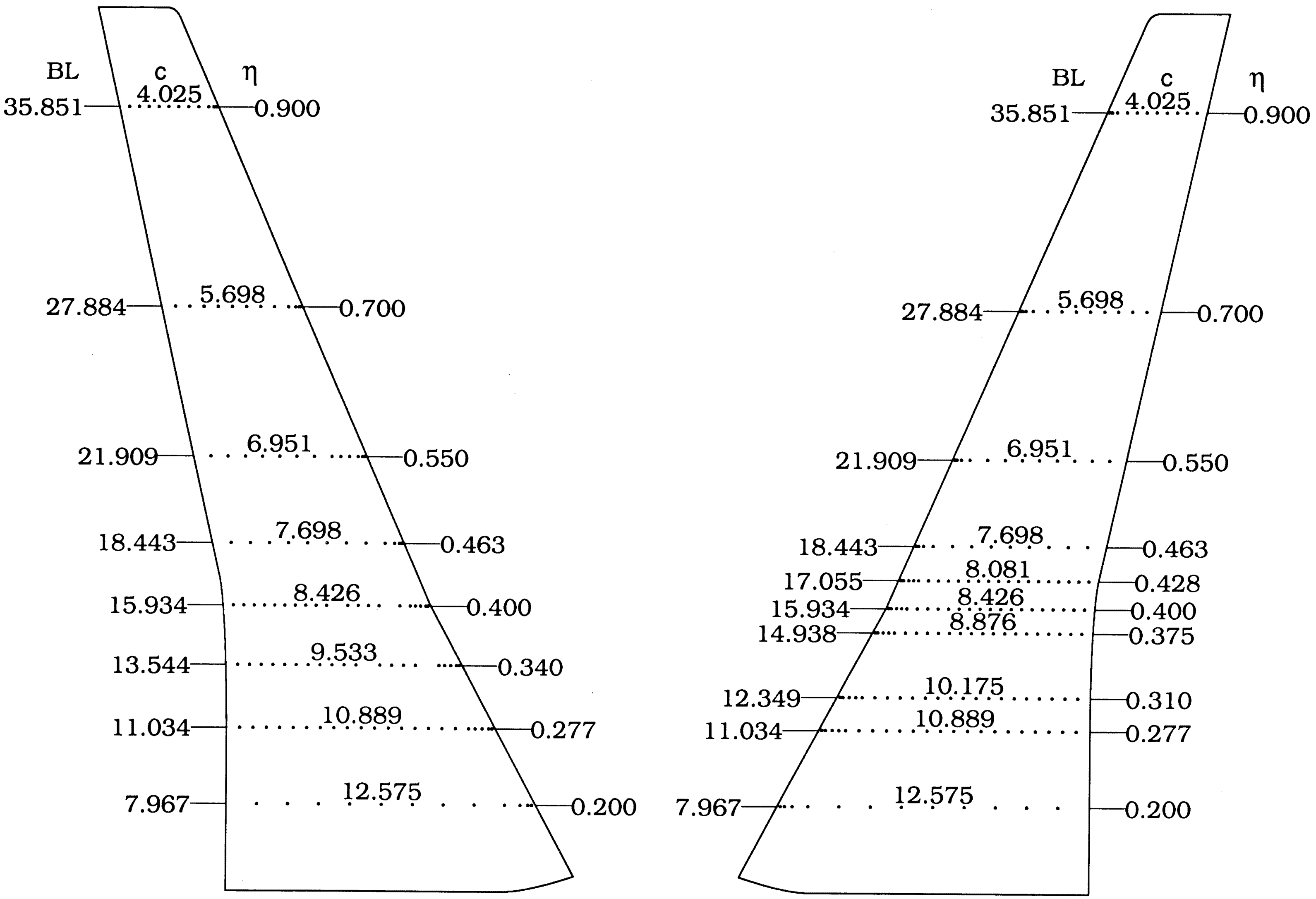

UPPER SURFACE

LOWER SURFACE

Figure 8. Sketches of wing with orifice locations. Linear dimensions are in inches.

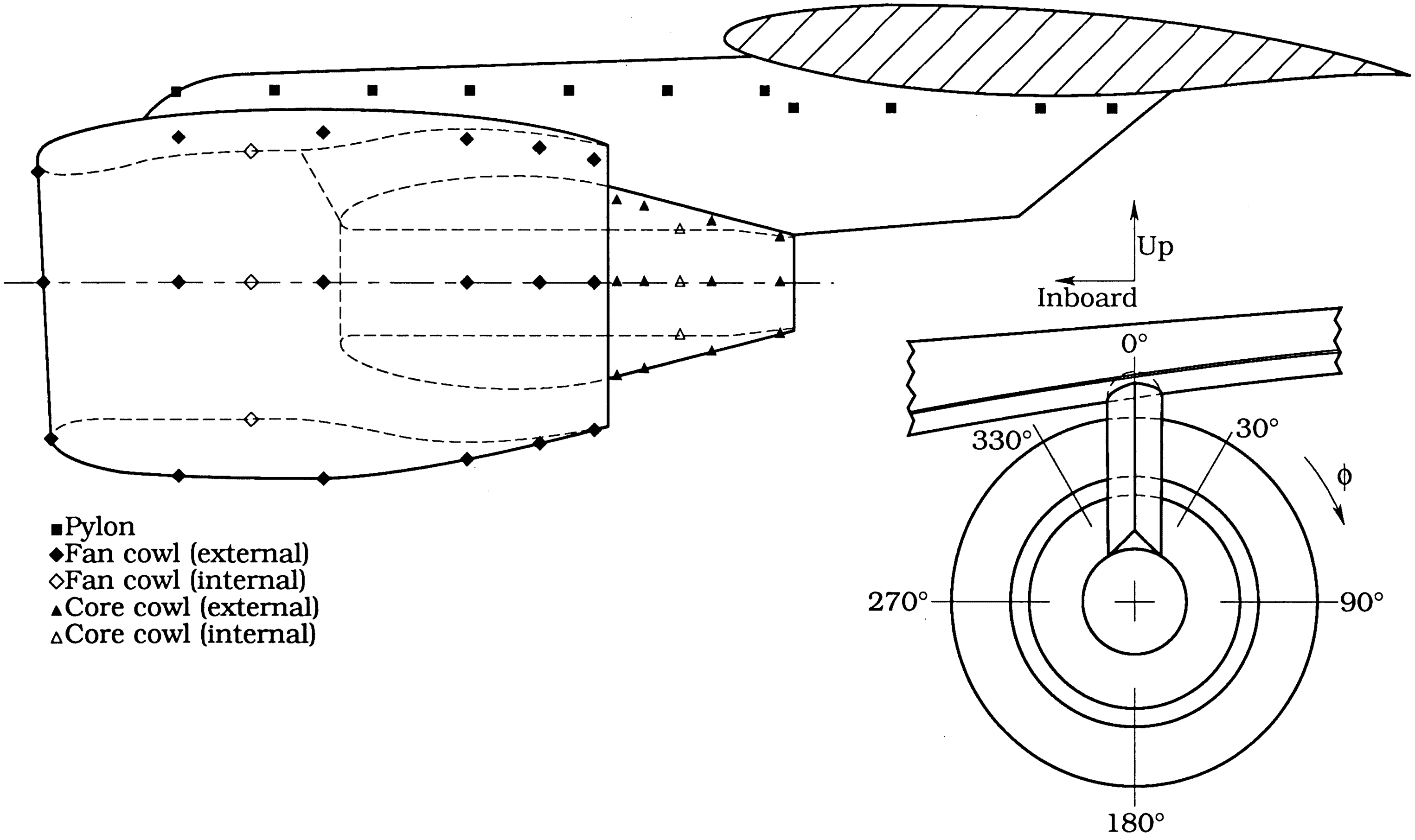

RIGHT NACELLE, REAR VIEW

(a) ATF nacelle.

Figure 9. Sketches of nacelle configurations showing distribution of orifices on right-hand nacelle.

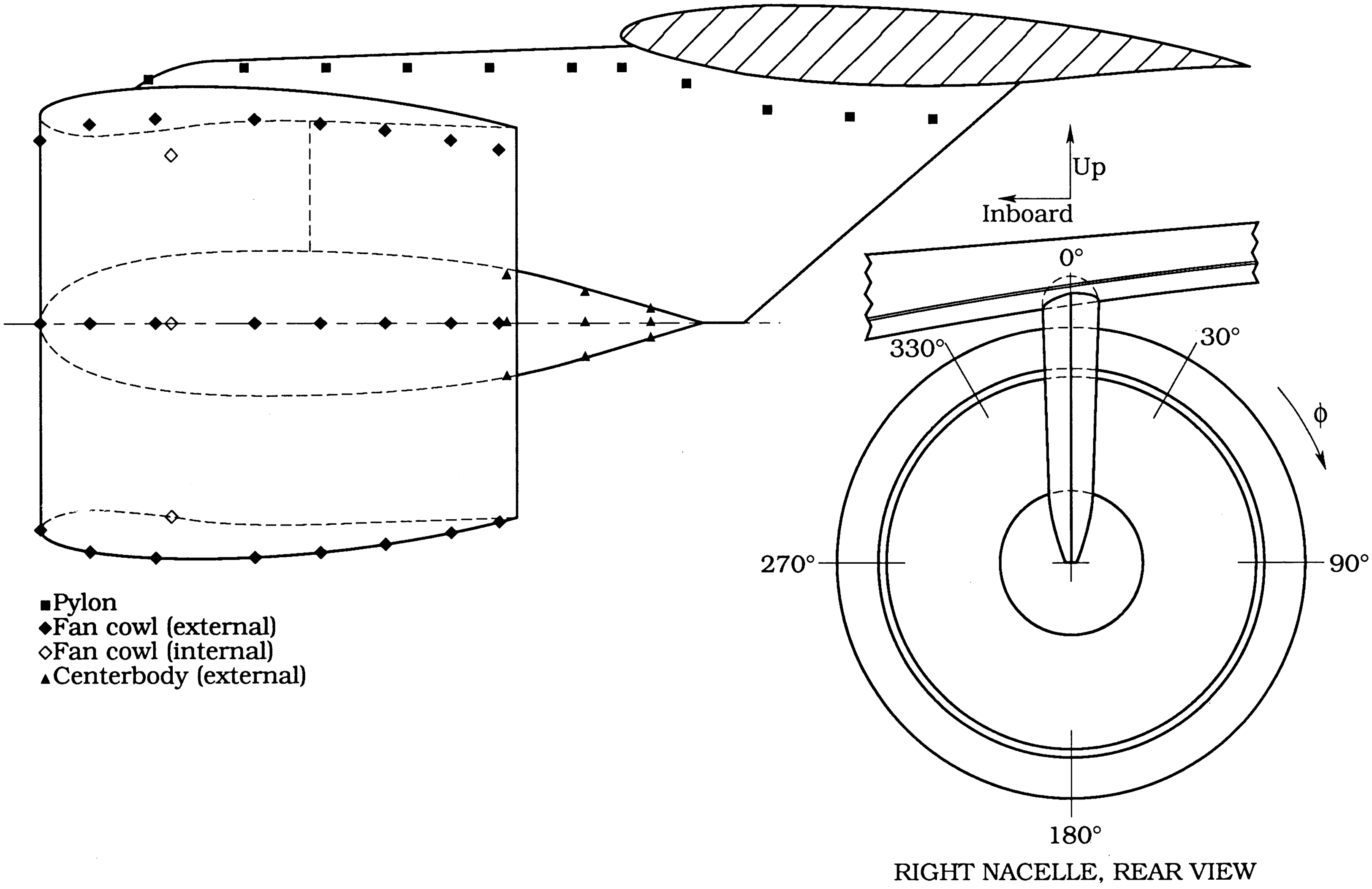

(b) SF-1 nacelle.

Figure 9. Continued.

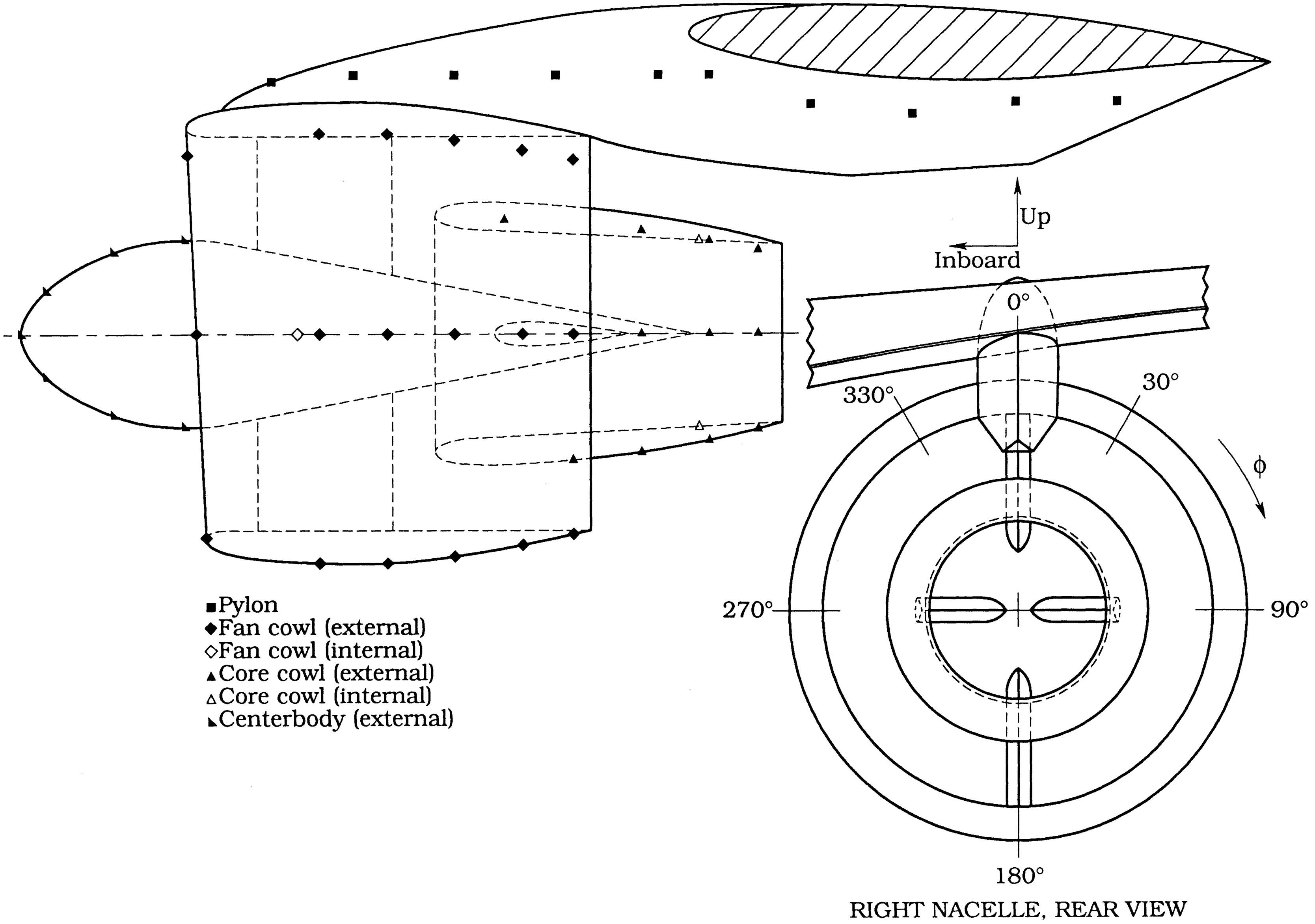

(c) SF-2 nacelle.

Figure 9. Concluded.

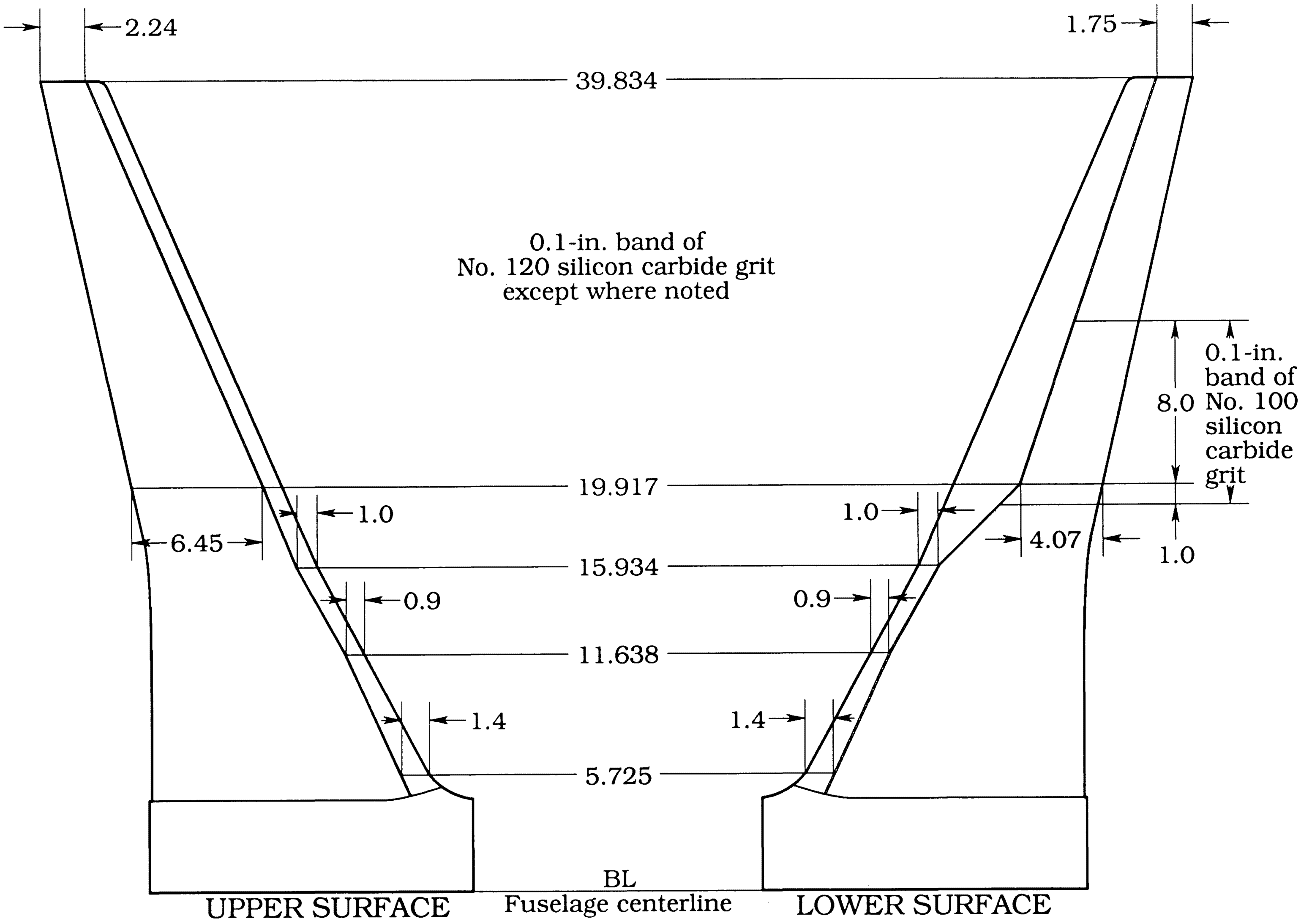

Figure 10. Location of boundary-layer transition strips on wing. Linear dimensions are in inches.

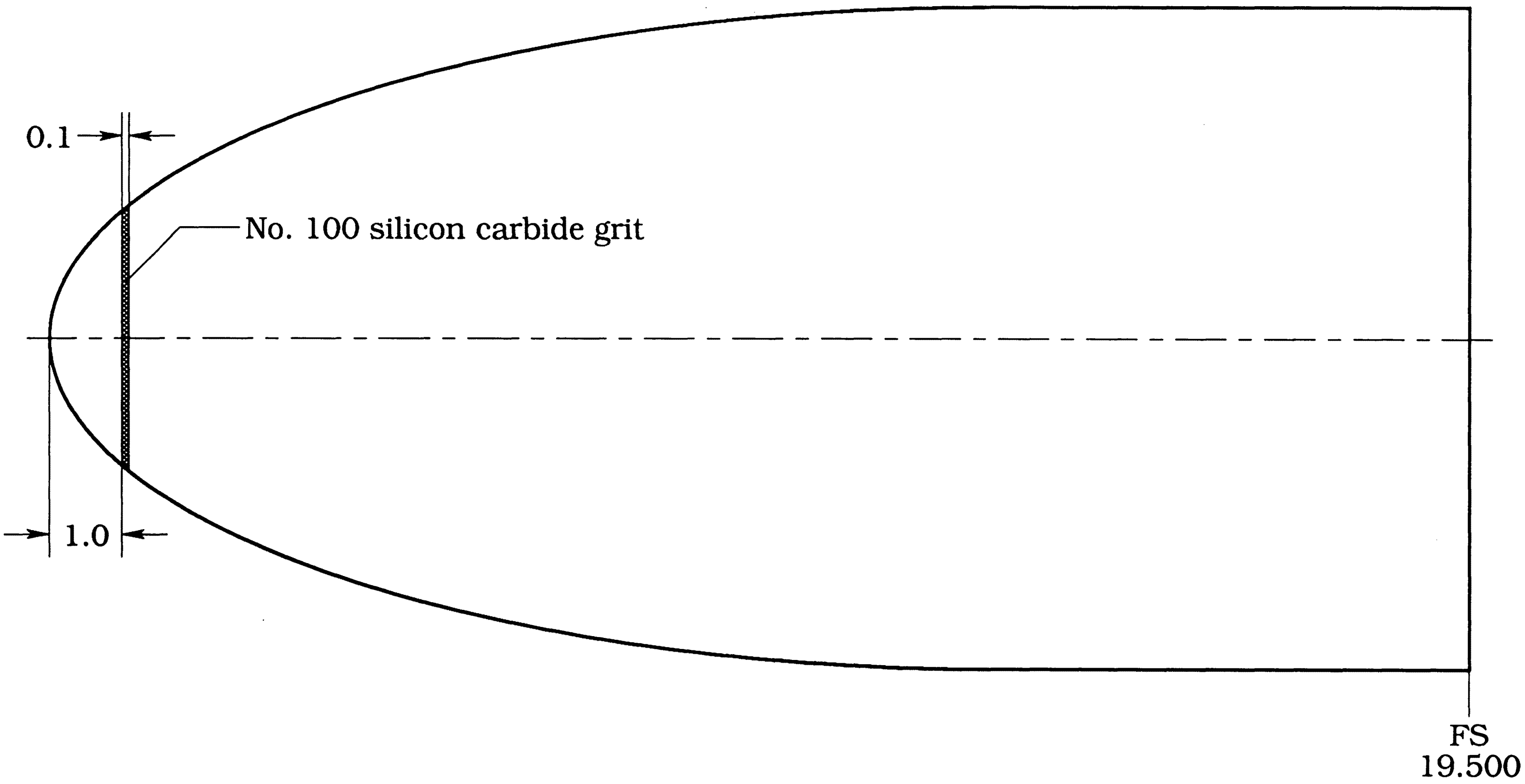

Figure 11. Location of boundary-layer transition strips on fuselage nose. Linear dimensions are in inches.

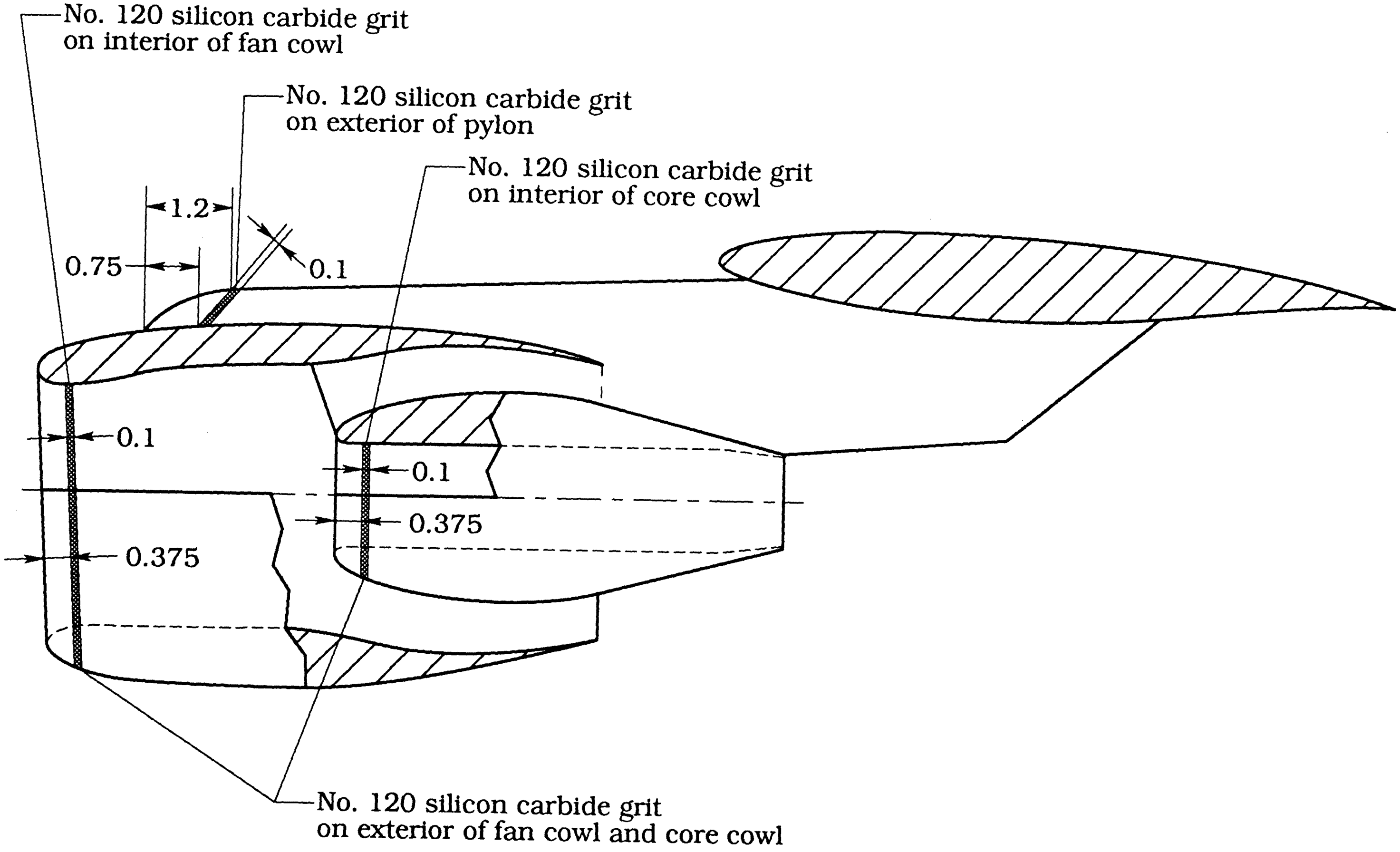

(a) ATF nacelles.

Figure 12. Location of boundary-layer transition strips on the nacelle configurations. Linear dimensions are in inches.

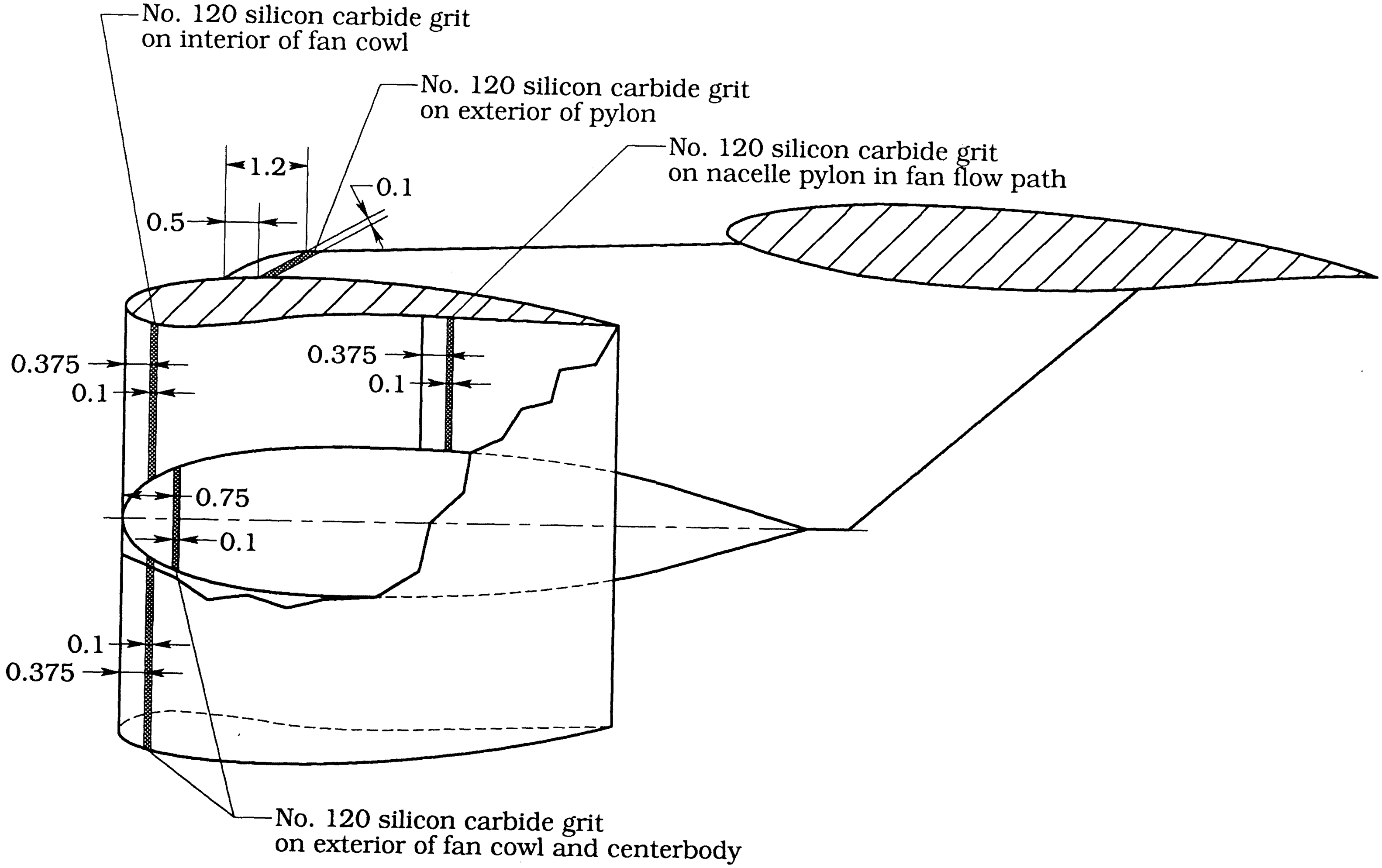

(b) SF-1 nacelles.

Figure 12. Continued.

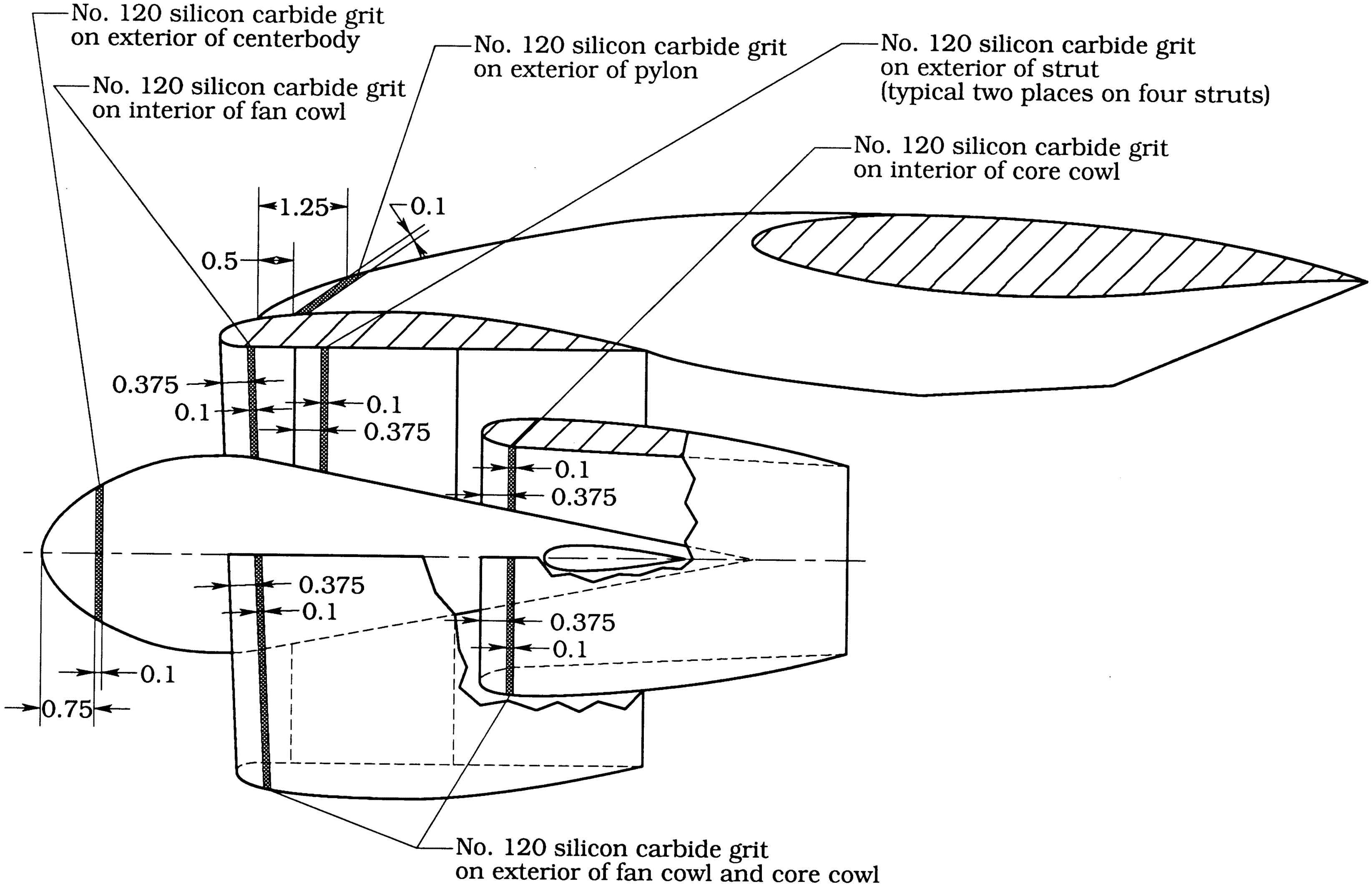

(c) SF-2 nacelles.

Figure 12. Concluded.

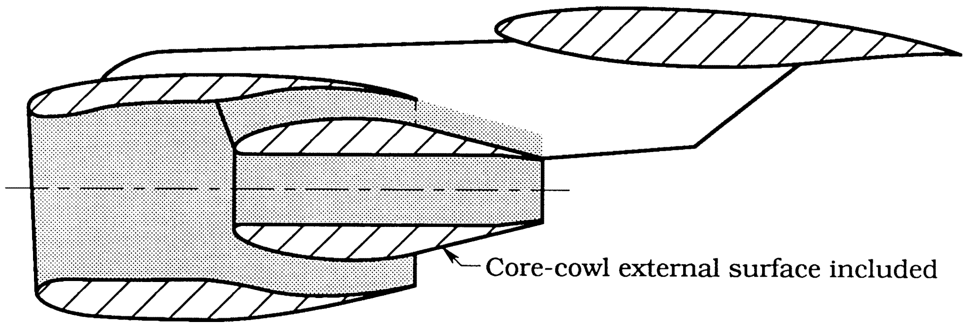

(a) ATF nacelle.

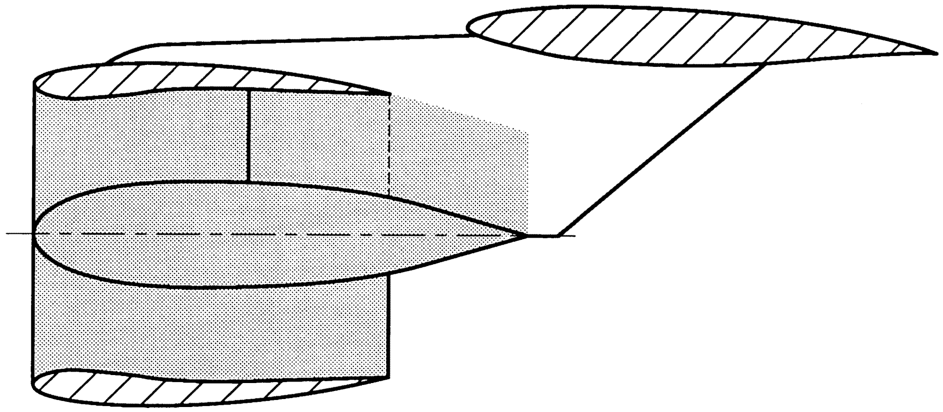

(b) SF-1 nacelle.

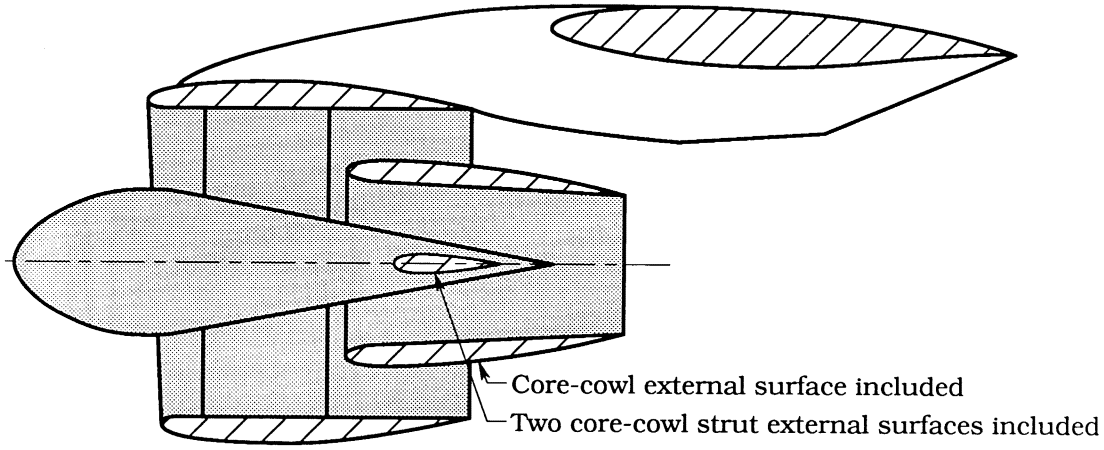

(c) SF-2 nacelle.

Figure 13. Areas on nacelles used for internal-drag calculations. Shaded areas indicate areas used for calculations.

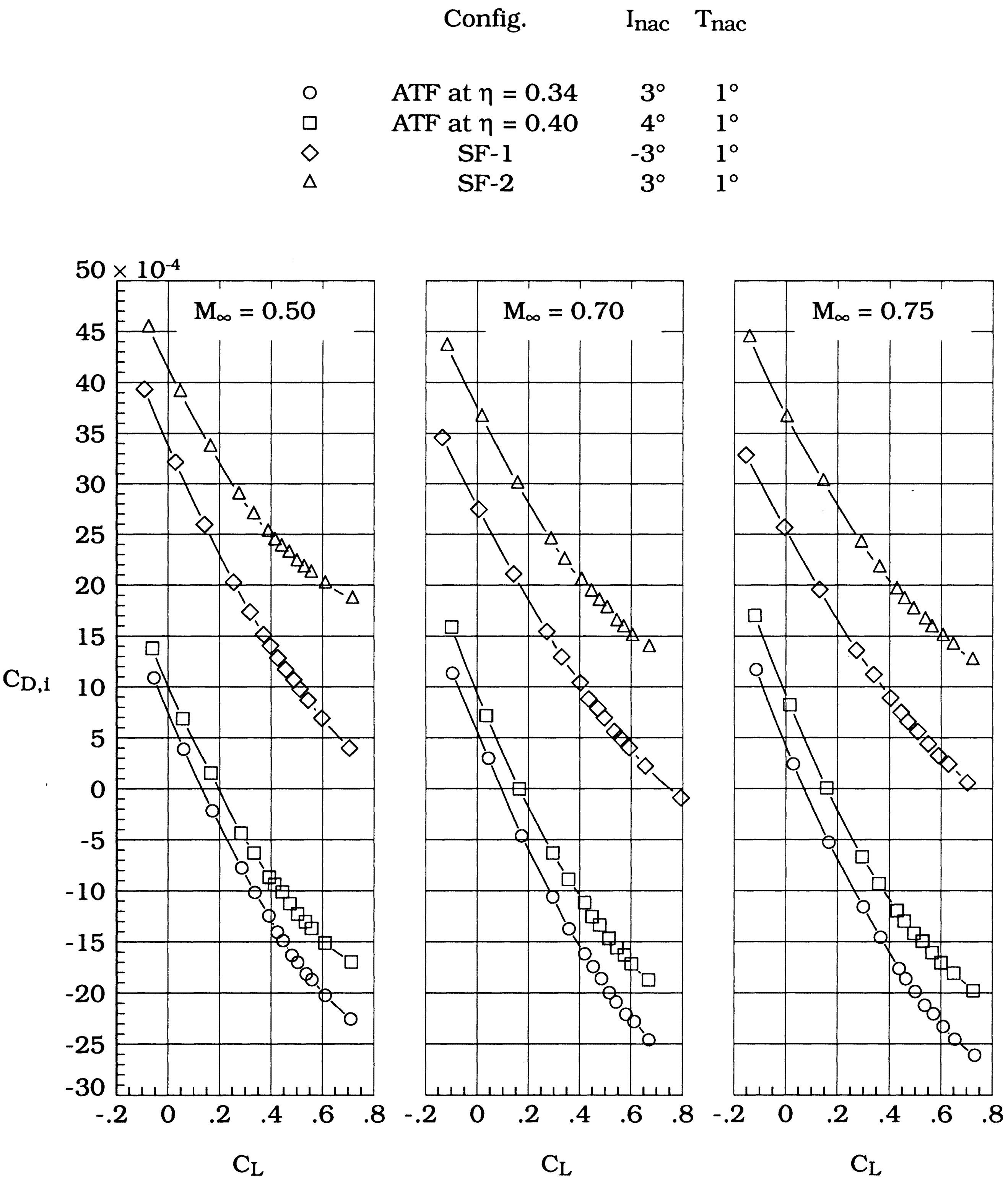

(a) $M_\infty = 0.50$, 0.70, and 0.75.

Figure 14. Variation of total internal drag with lift coefficient for two nacelles.

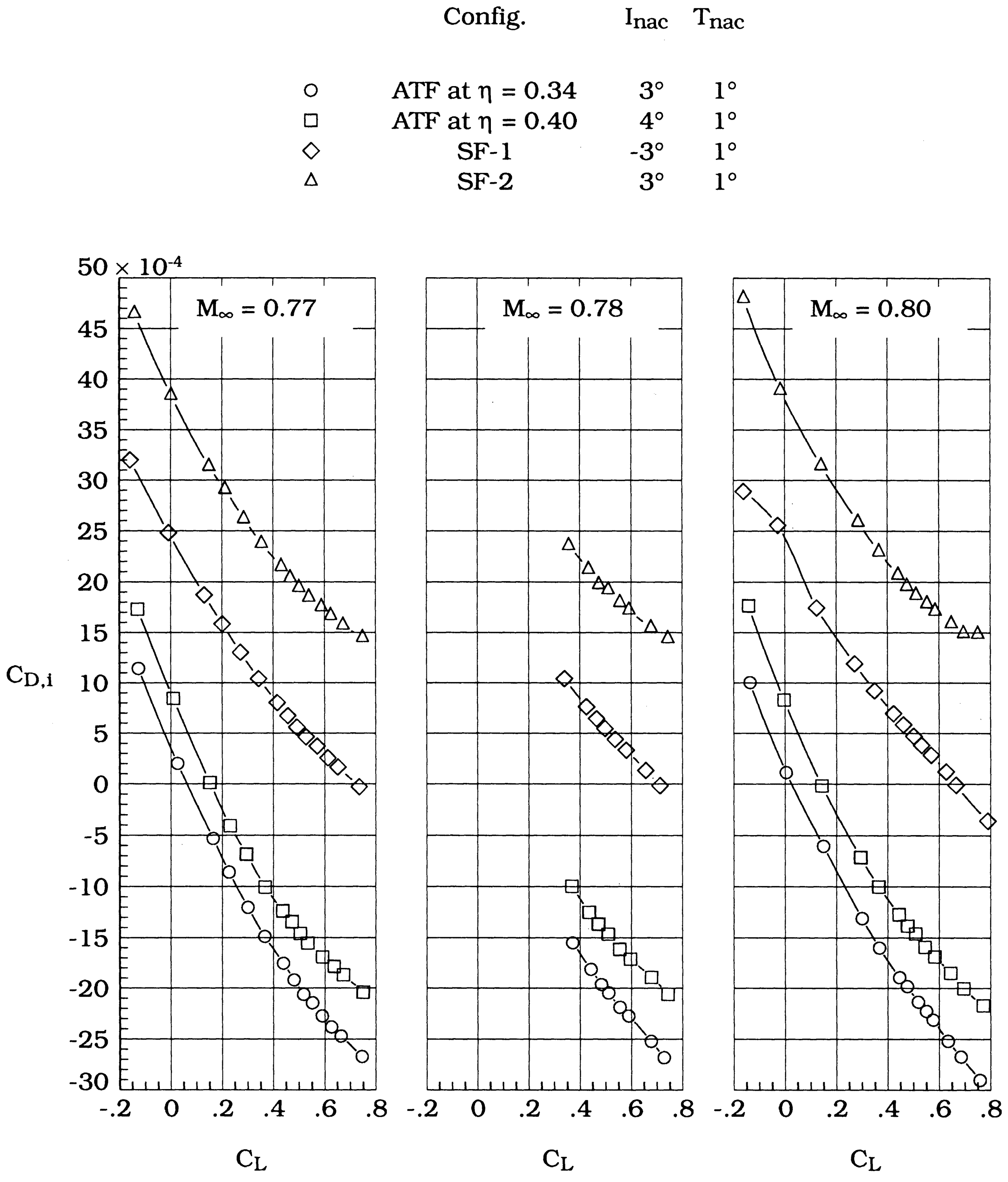

(b) $M_\infty = 0.77$, 0.78, and 0.80.

Figure 14. Concluded.

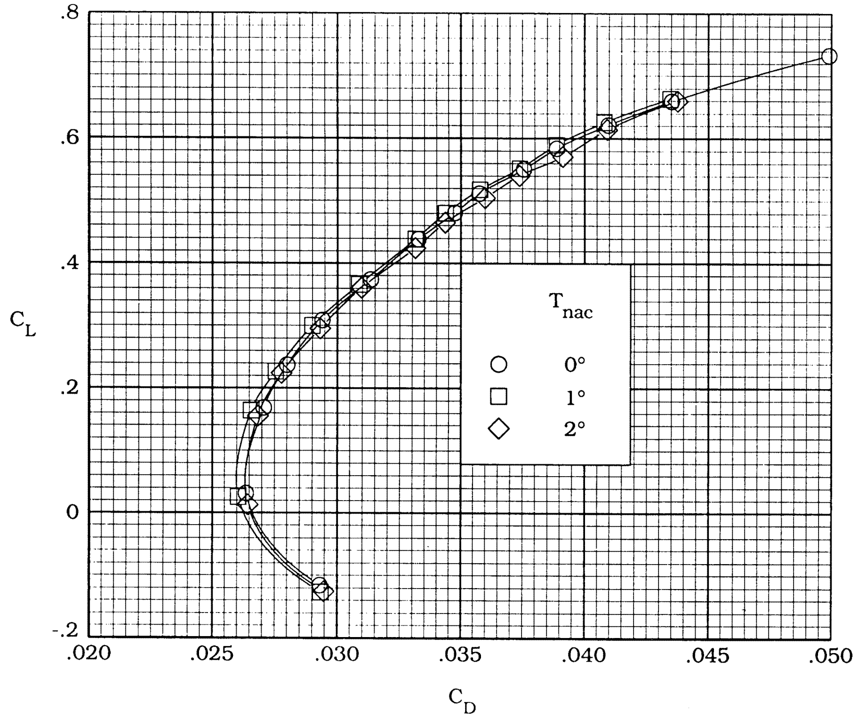

(a) $I_{\text{nac}} = 3°$.

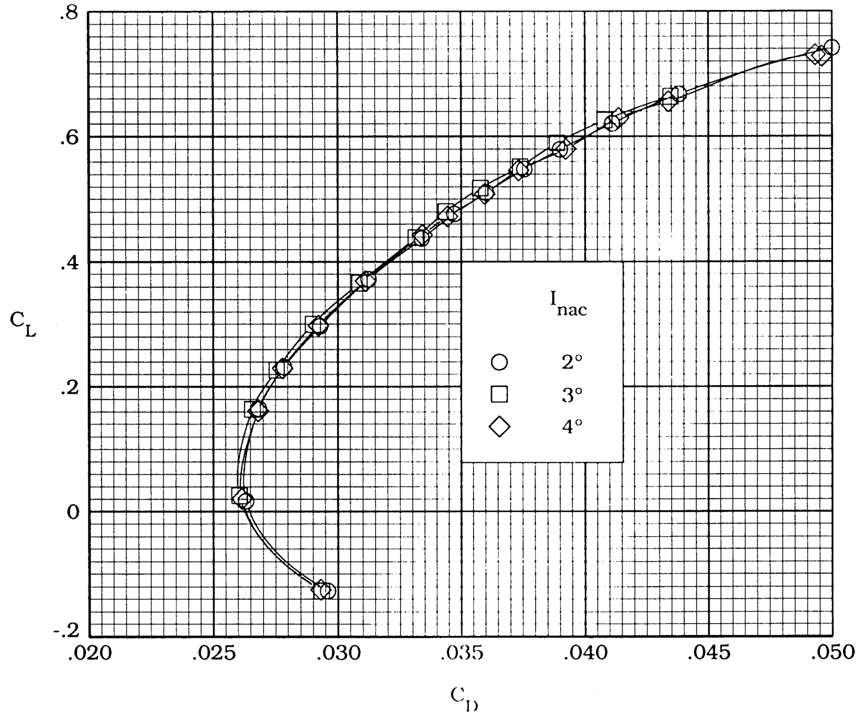

(b) $T_{\text{nac}} = 1°$.

Figure 15. Drag polars for ATF nacelle installation with varying nacelle incidence angle or toe-in angle at $\eta = 0.34$. $M_\infty = 0.77$.

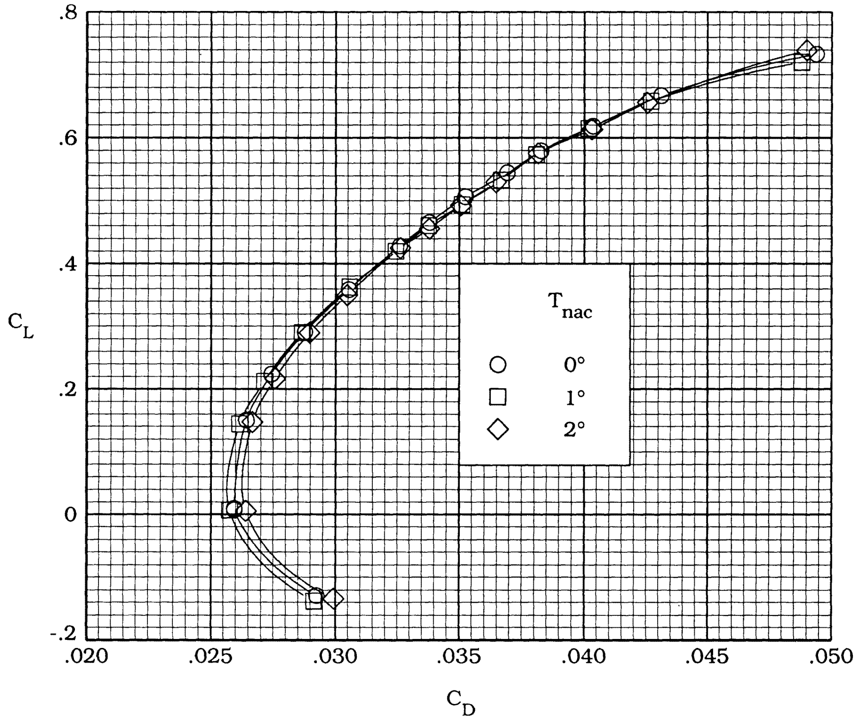

(a) $I_{nac} = 3°$.

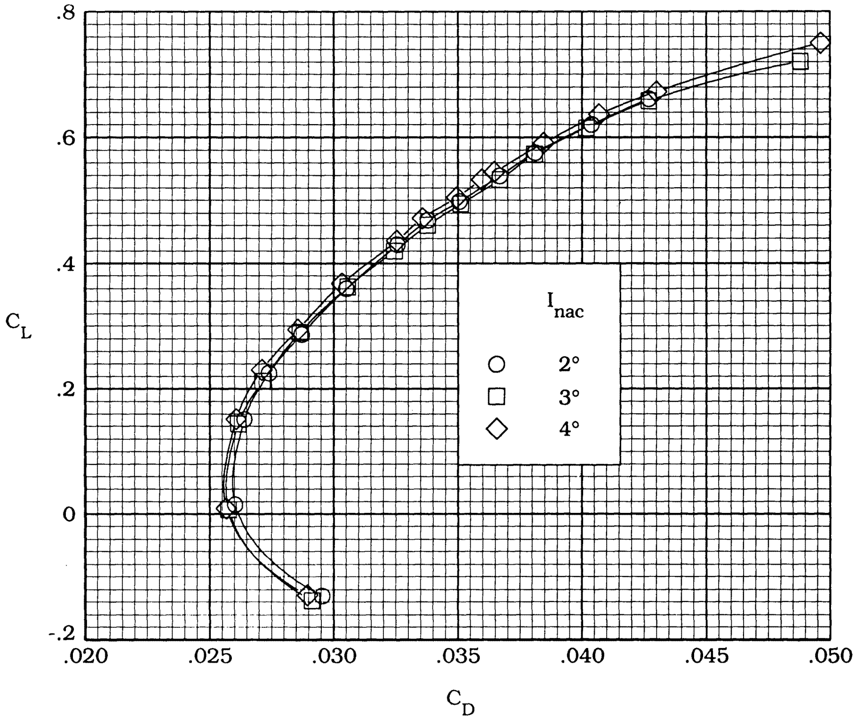

(b) $T_{nac} = 1°$.

Figure 16. Drag polars for ATF nacelle installation with varying nacelle incidence angle or toe-in angle at $\eta = 0.40$. $M_\infty = 0.77$.

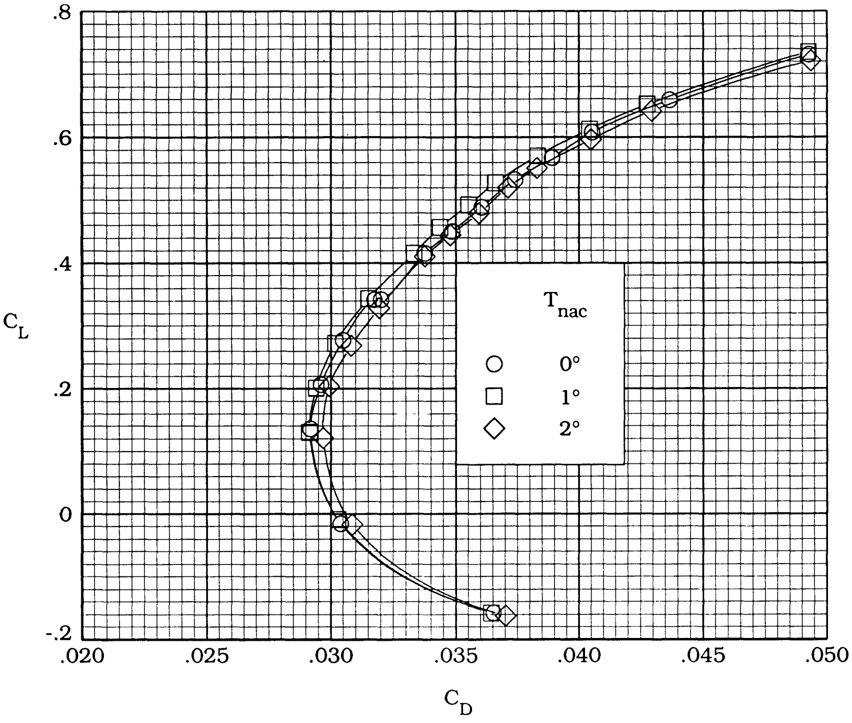

(a) $I_{nac} = 3°$.

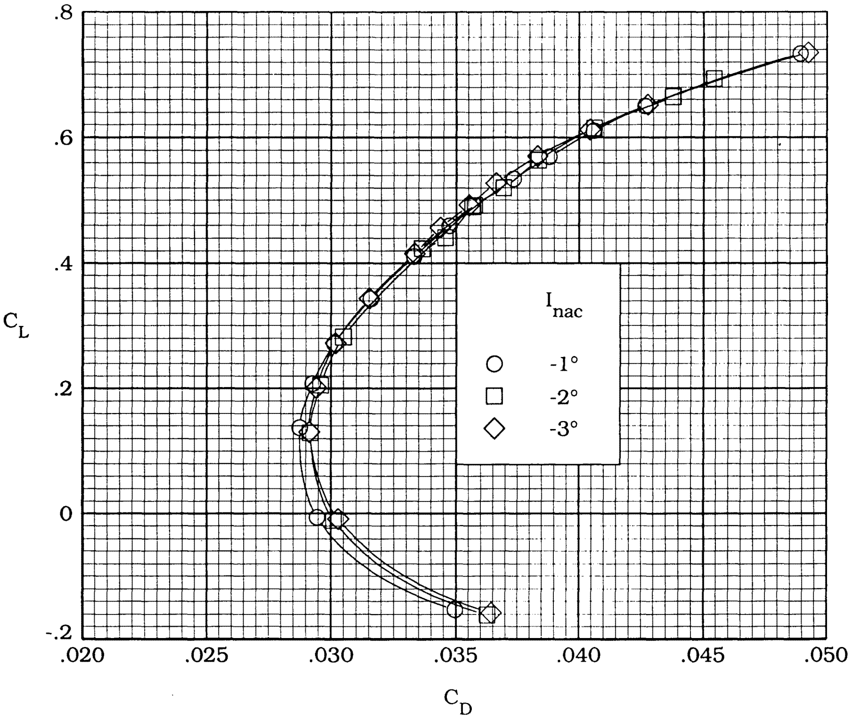

(b) $T_{nac} = 1°$.

Figure 17. Drag polars for SF-1 nacelle installation with varying nacelle incidence angle or toe-in angle at $\eta = 0.40$. $M_\infty = 0.77$.

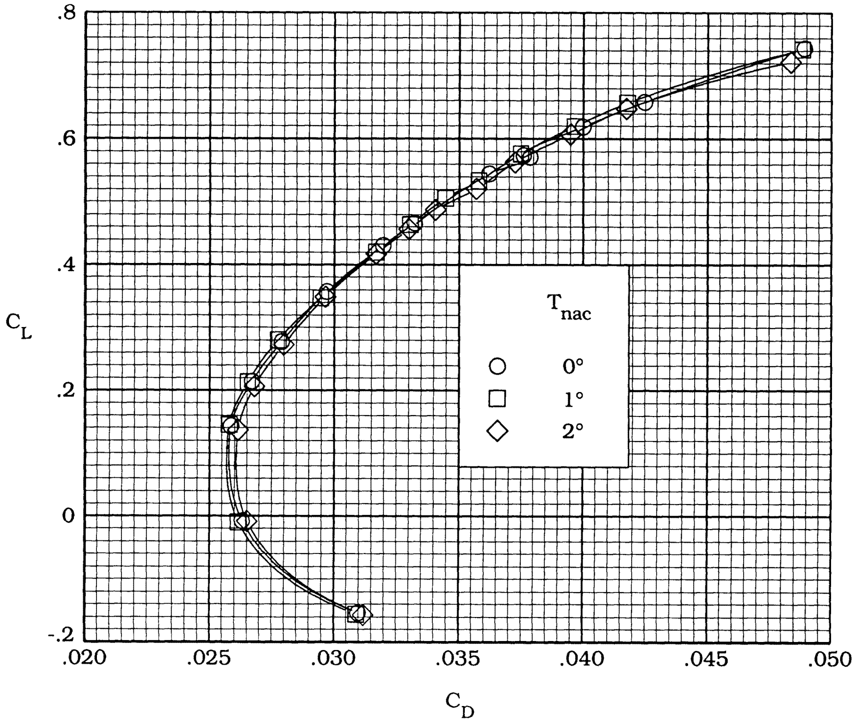

(a) $I_{nac} = 2°$.

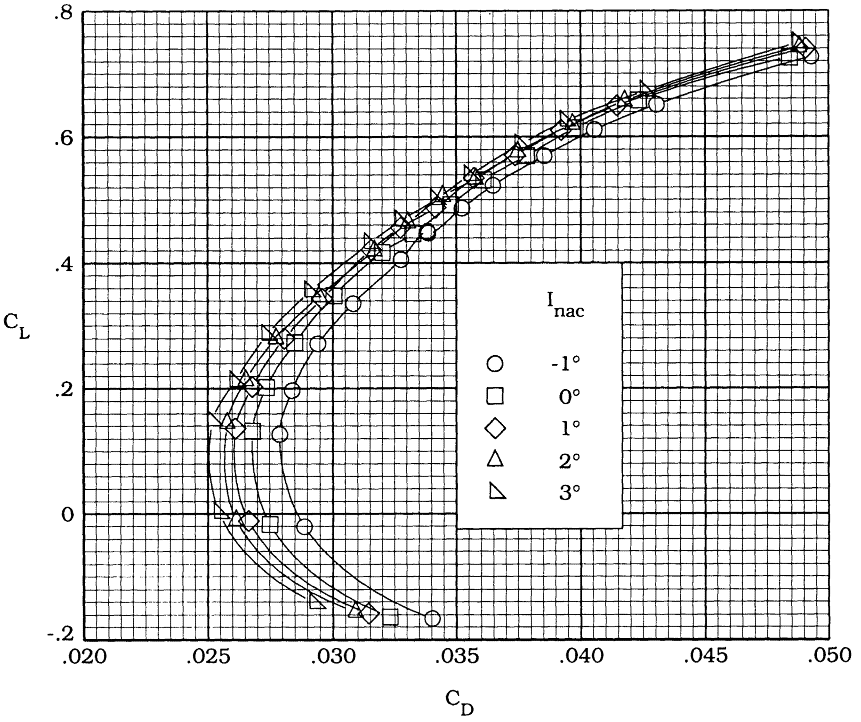

(b) $T_{nac} = 1°$.

Figure 18. Drag polars for SF-2 nacelle installation with varying nacelle incidence angle or toe-in angle at $\eta = 0.40$. $M_\infty = 0.77$.

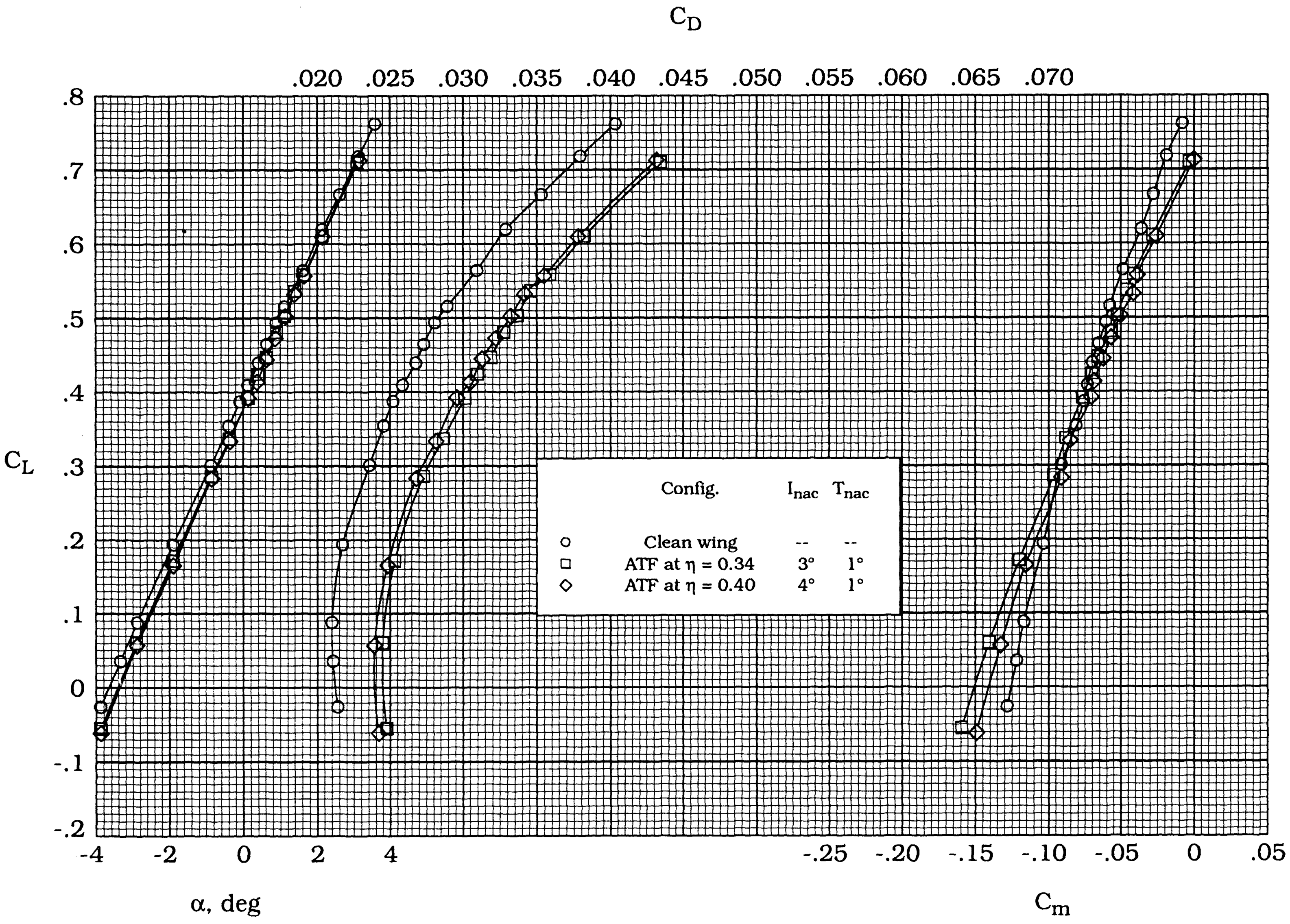

(a) $M_\infty = 0.50$.

Figure 19. Comparisons of force and moment coefficients for ATF nacelles on and off at $\eta = 0.34$ and $\eta = 0.40$.

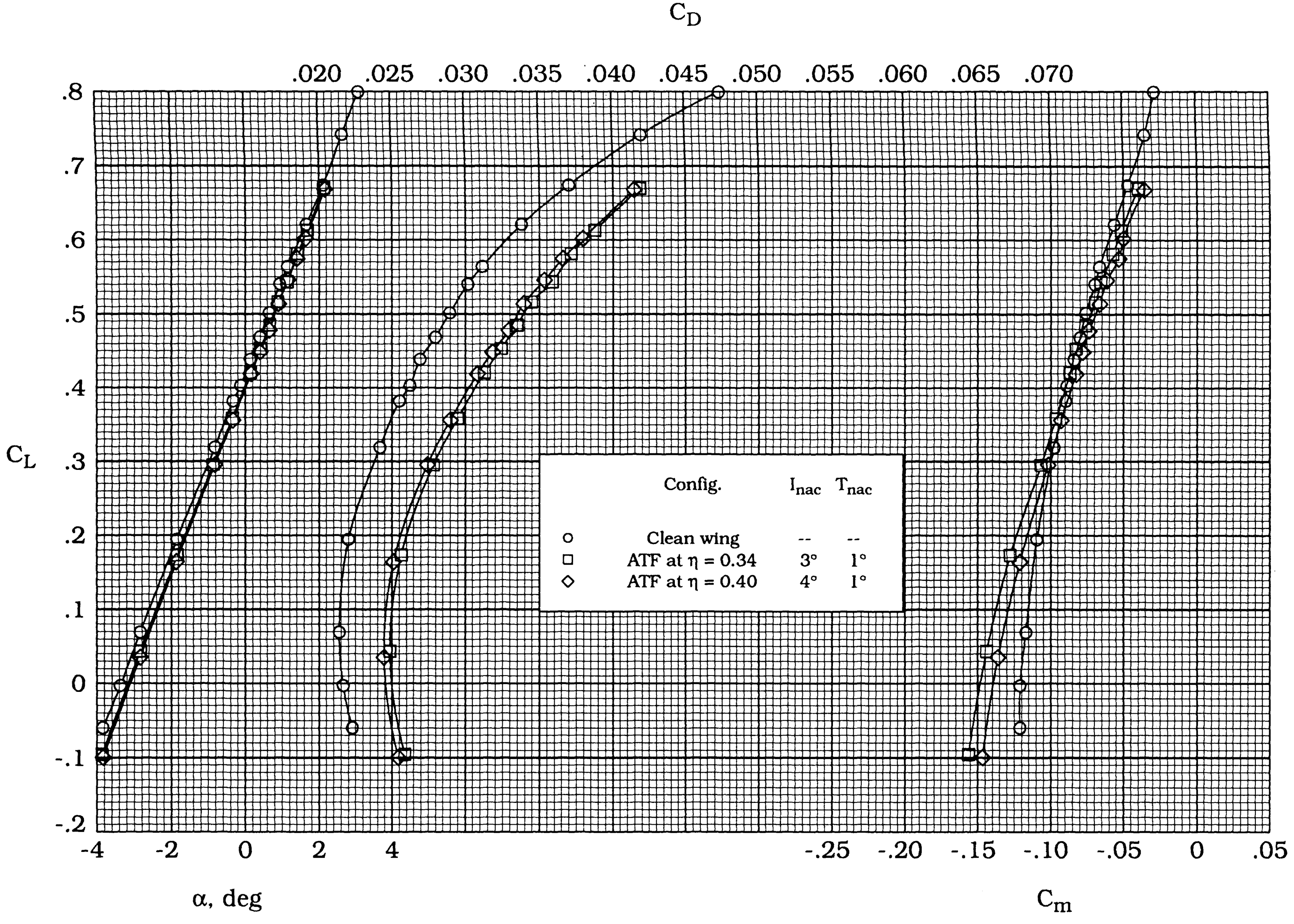

(b) $M_\infty = 0.70$.

Figure 19. Continued.

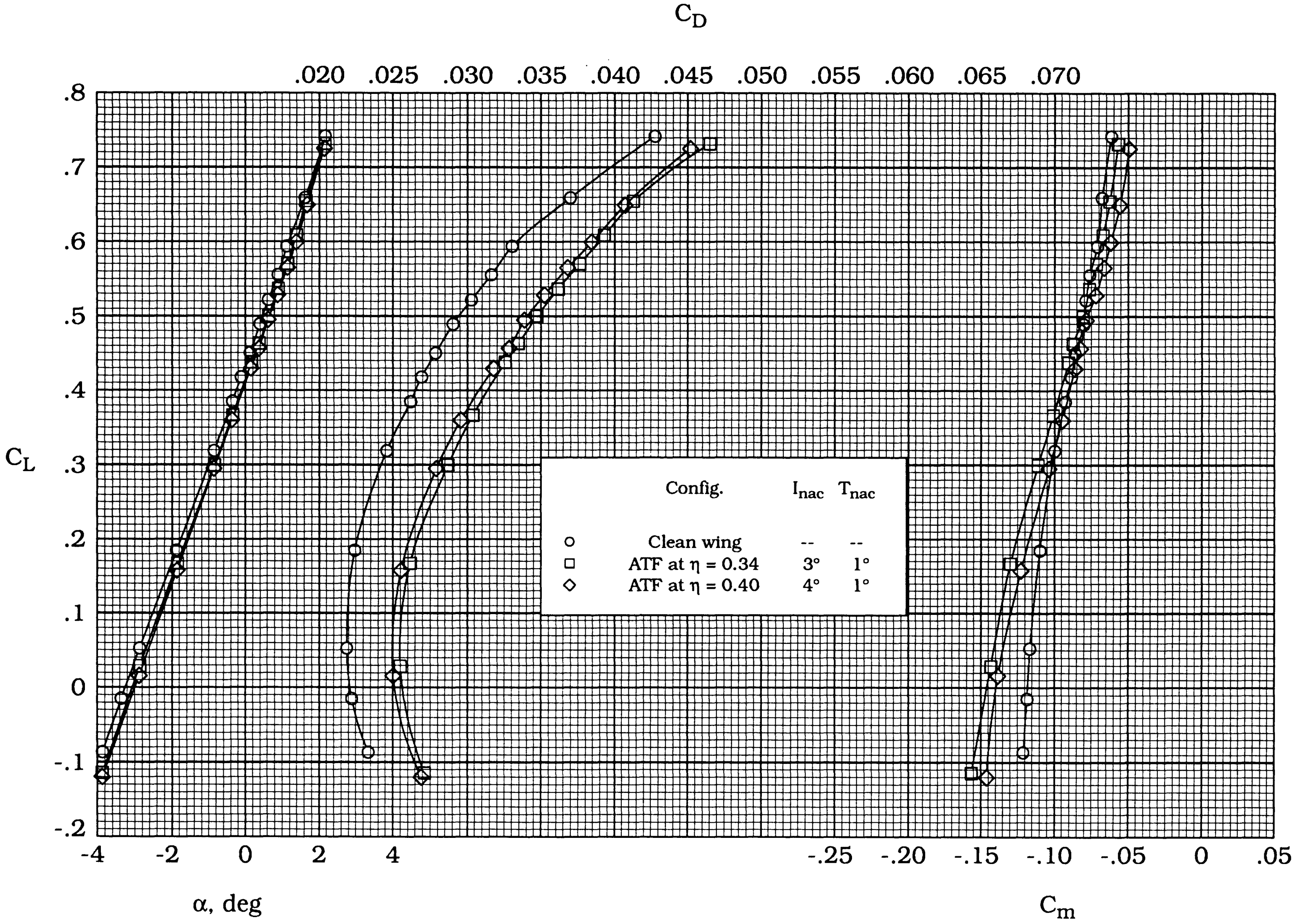

(c) $M_\infty = 0.75$.

Figure 19. Continued.

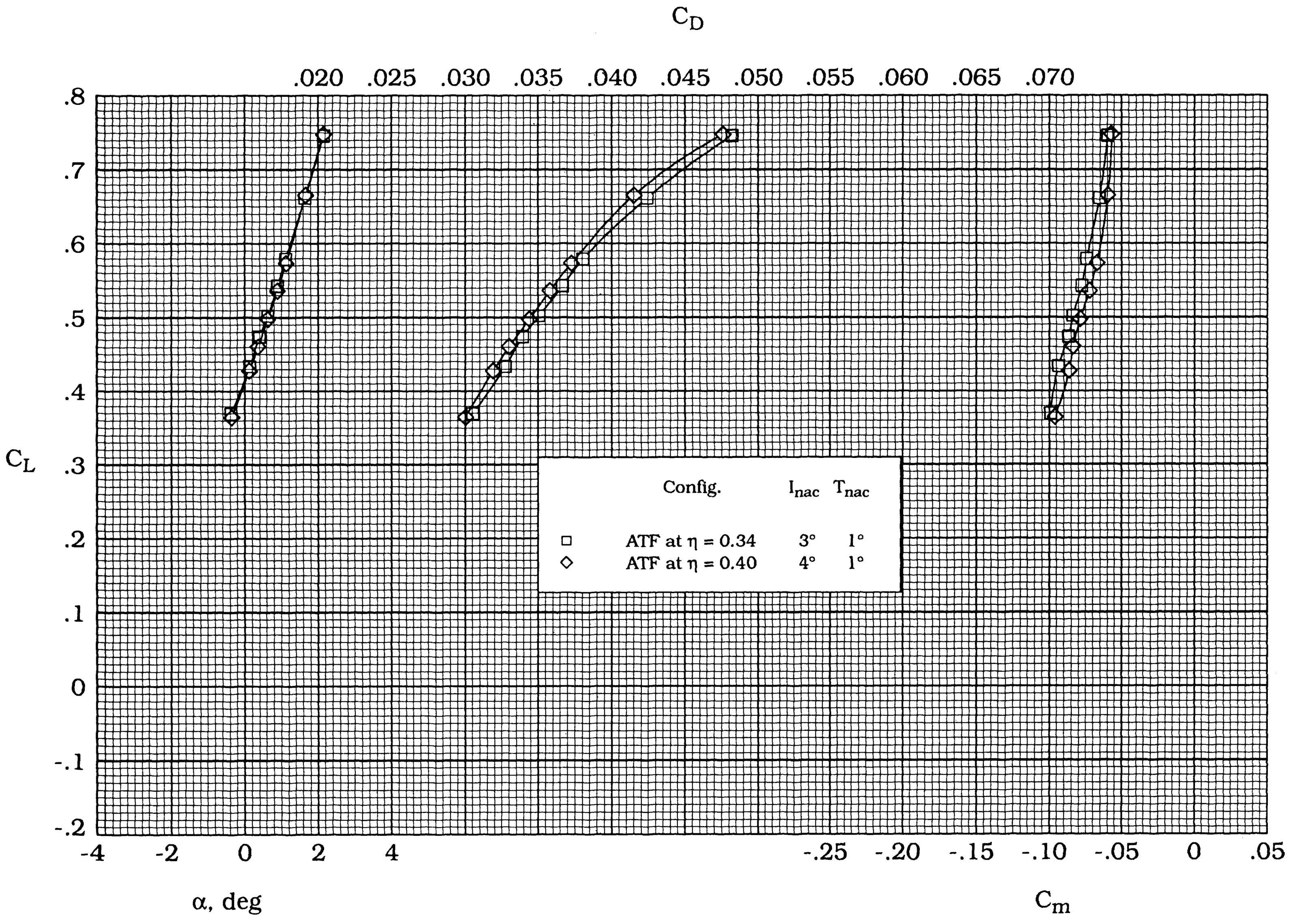

(d) $M_\infty = 0.76$.

Figure 19. Continued.

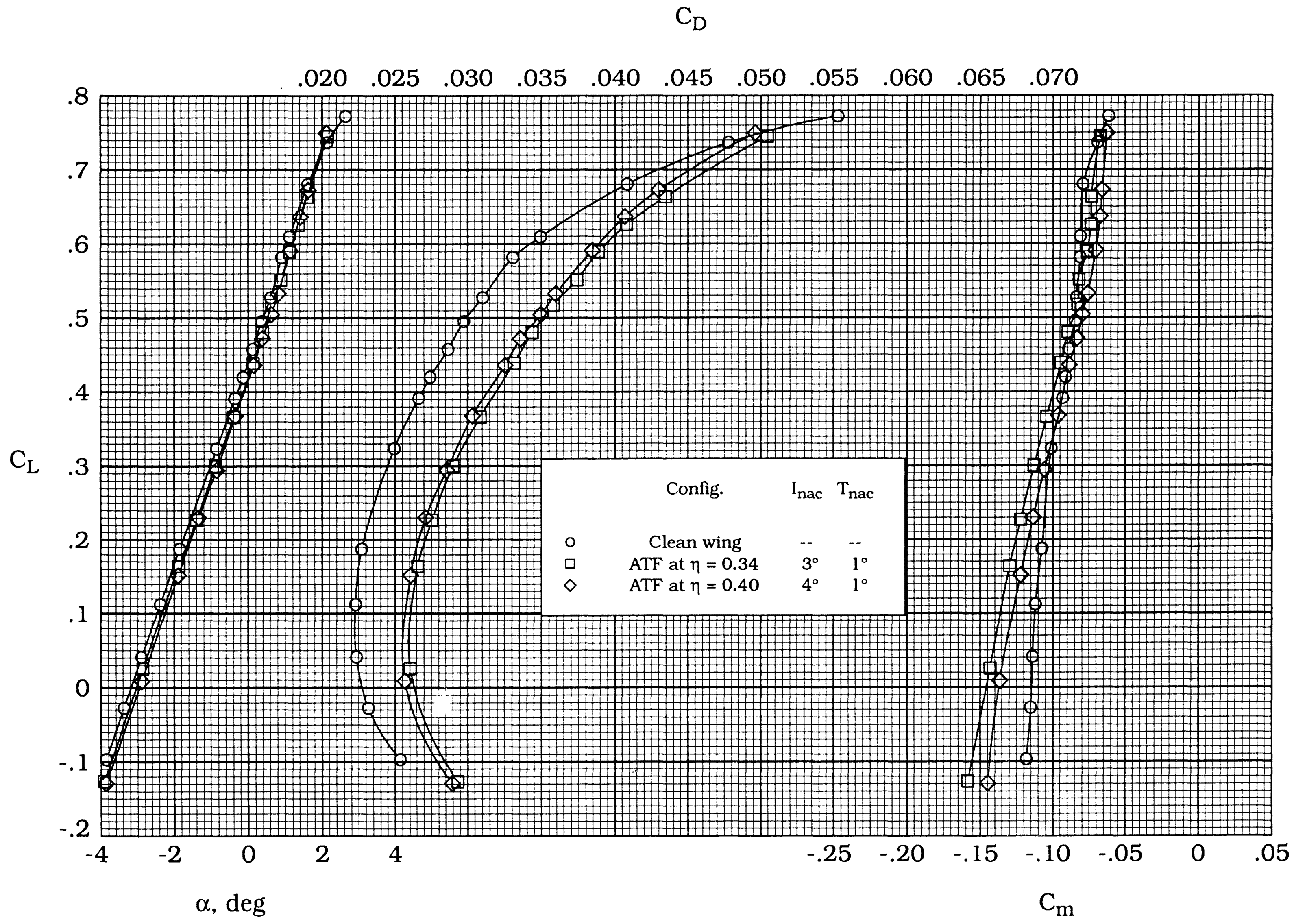

(e) $M_\infty = 0.77$.

Figure 19. Continued.

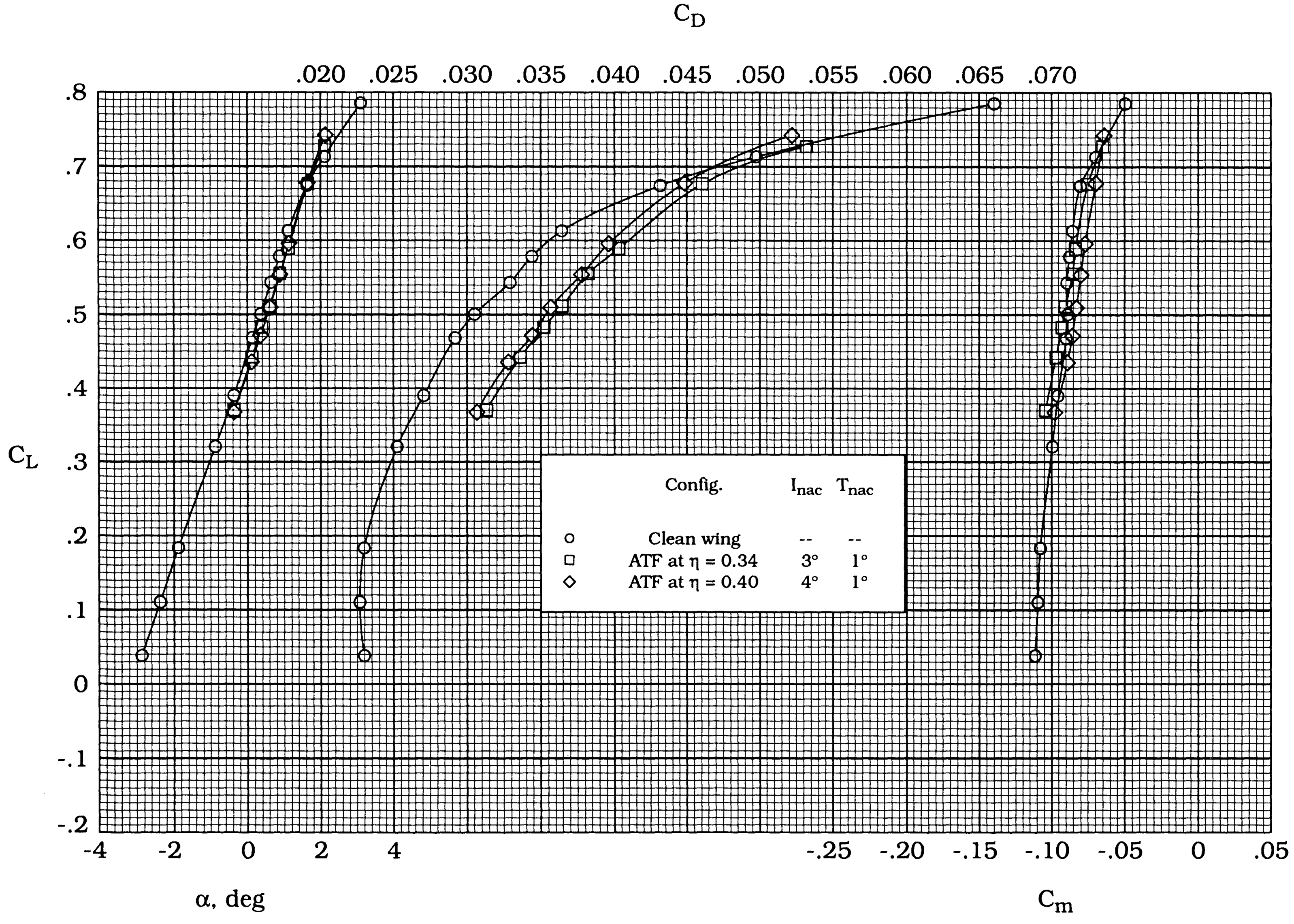

(f) $M_\infty = 0.78$.

Figure 19. Continued.

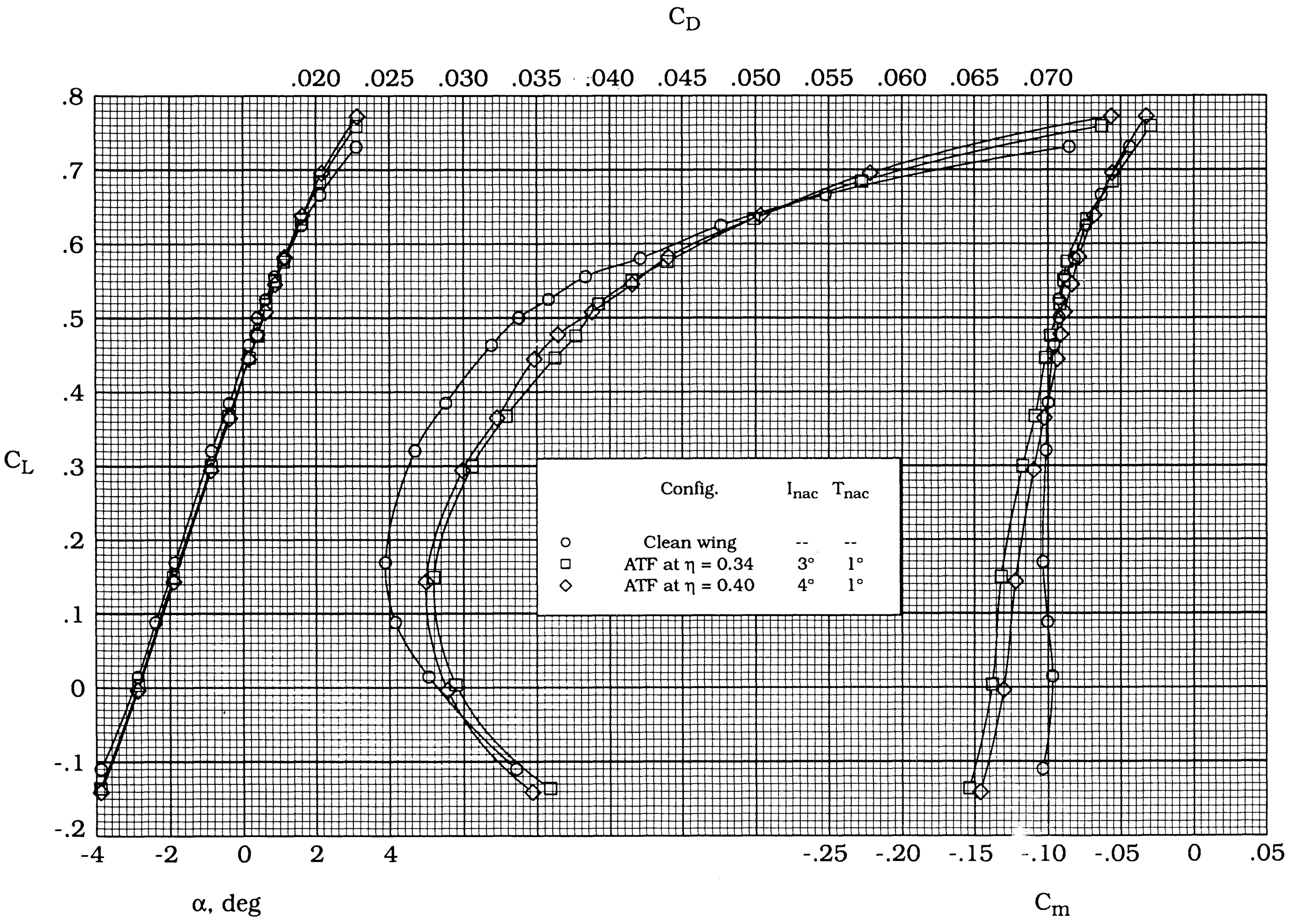

(g) $M_\infty = 0.80$.

Figure 19. Concluded.

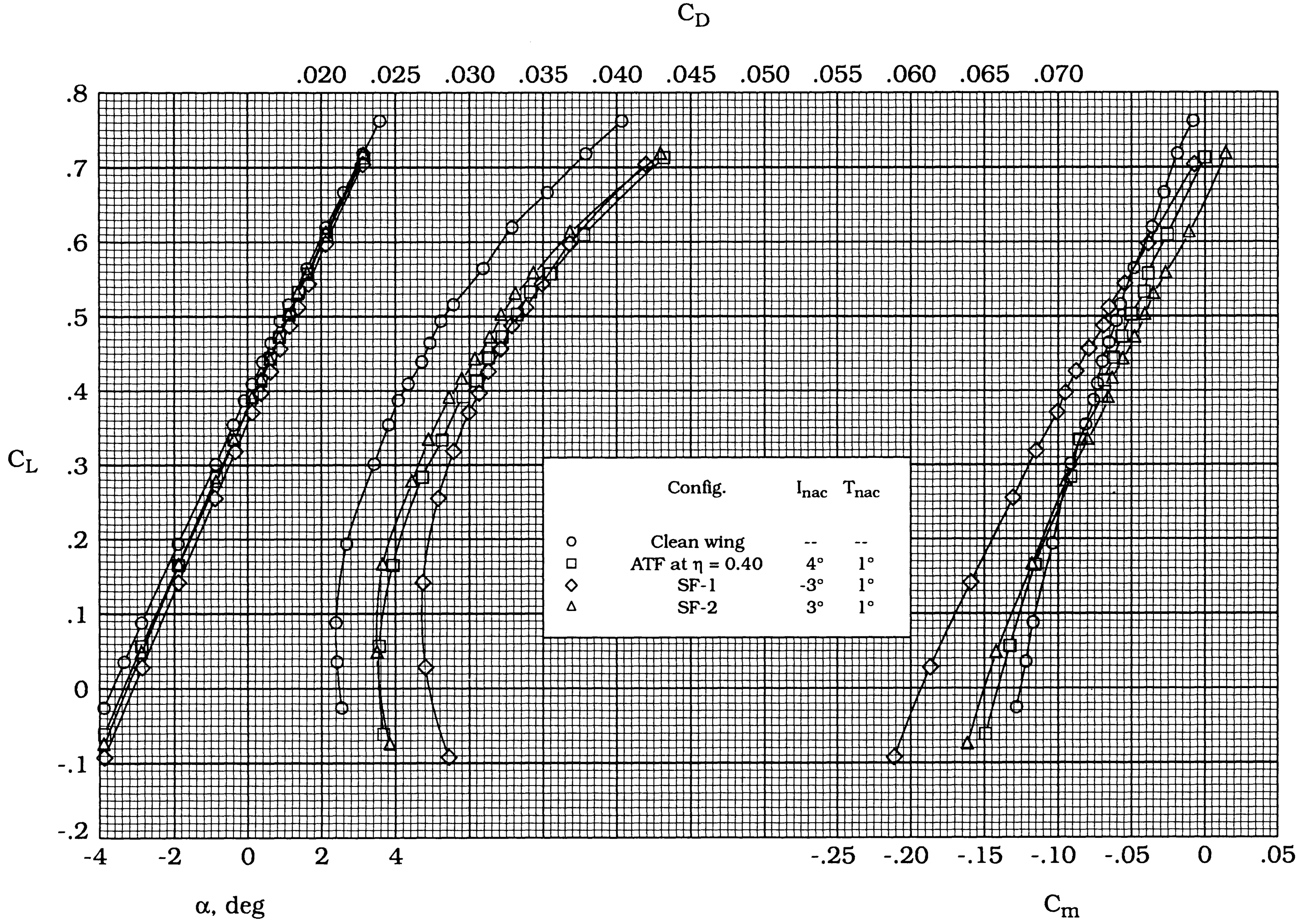

(a) $M_\infty = 0.50$.

Figure 20. Comparisons of force and moment coefficients for clean-wing, ATF, SF-1, and SF-2 nacelle configurations at $\eta = 0.40$.

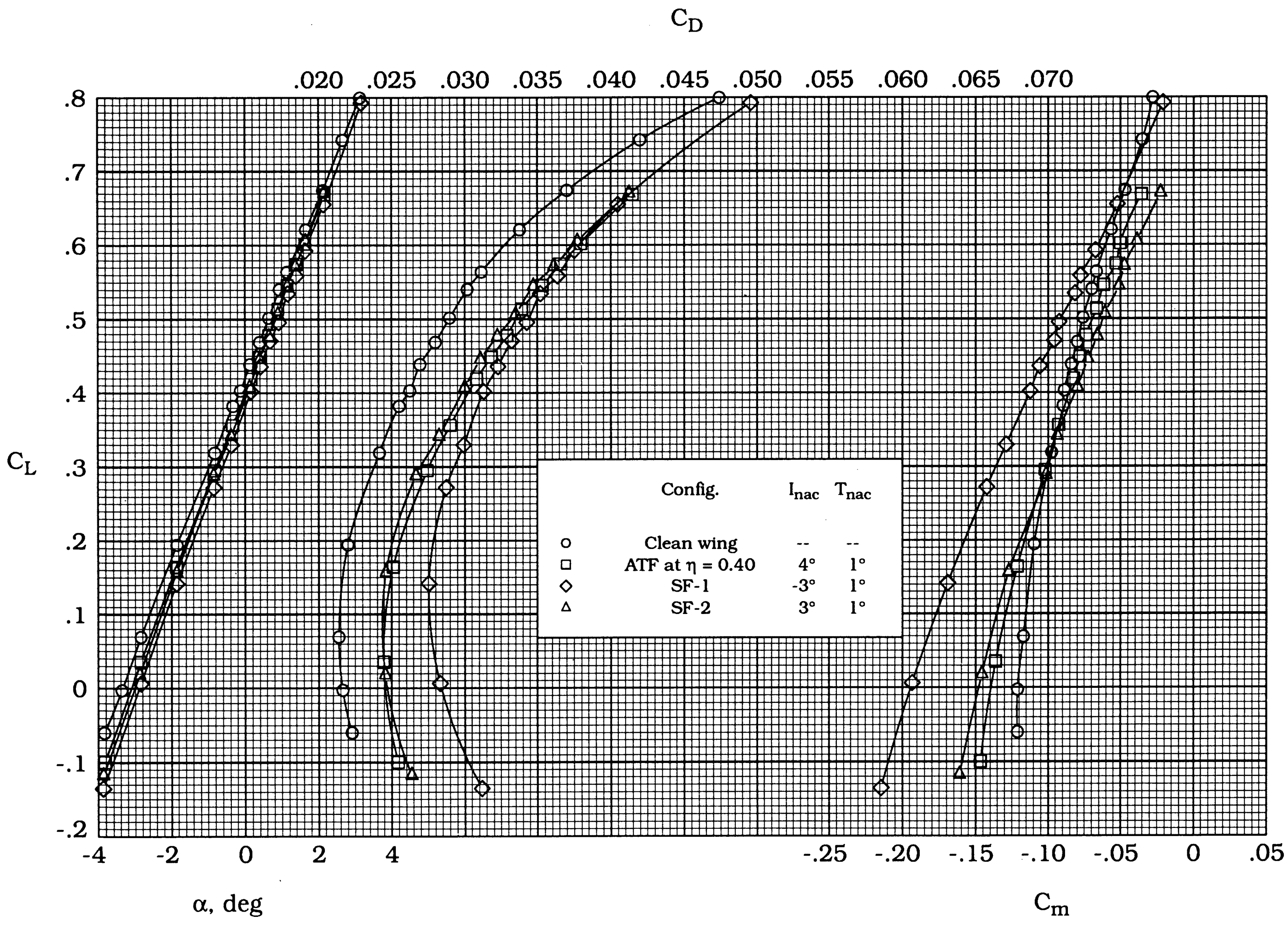

(b) $M_\infty = 0.70$.

Figure 20. Continued.

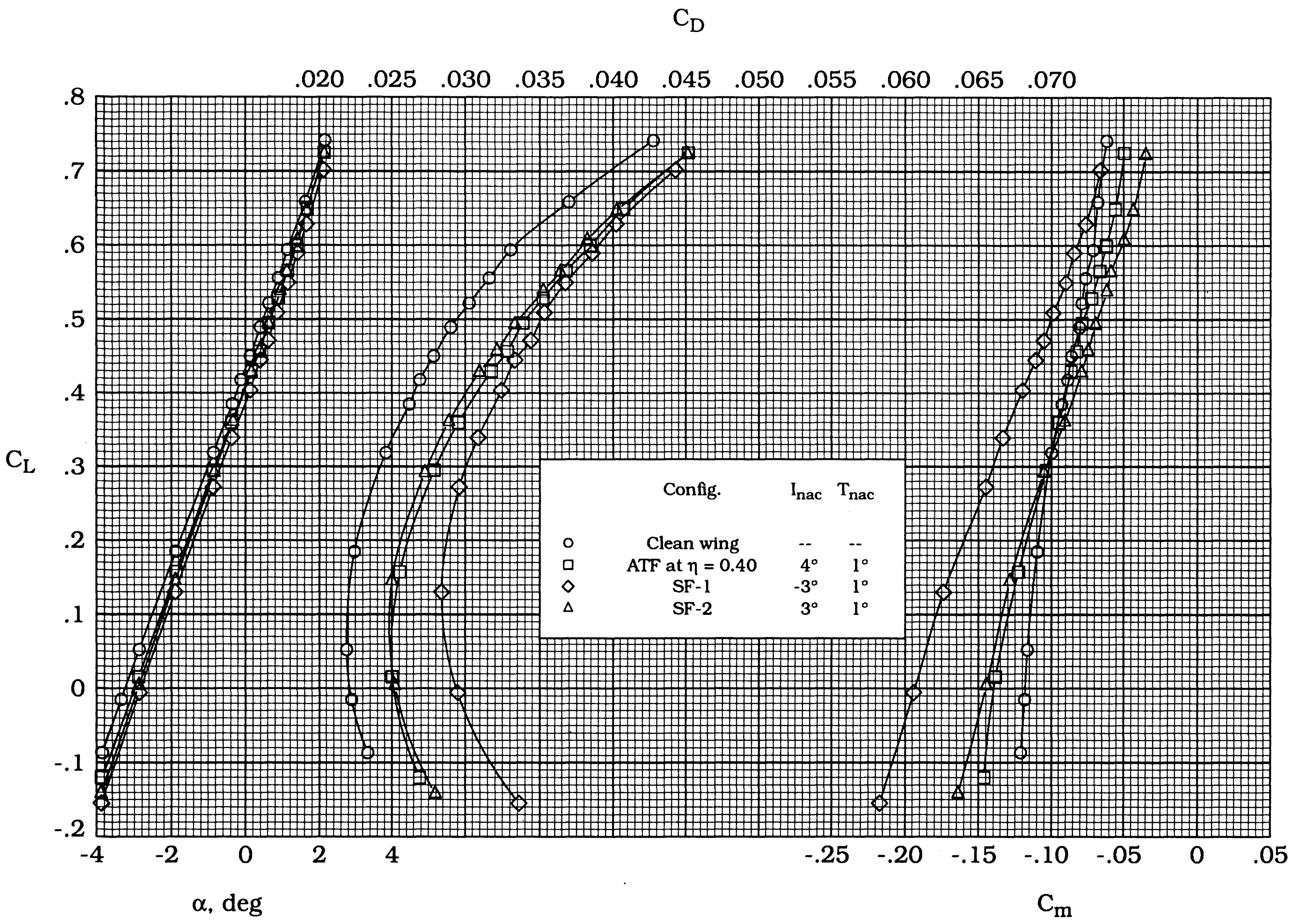

(c) $M_\infty = 0.75$.

Figure 20. Continued.

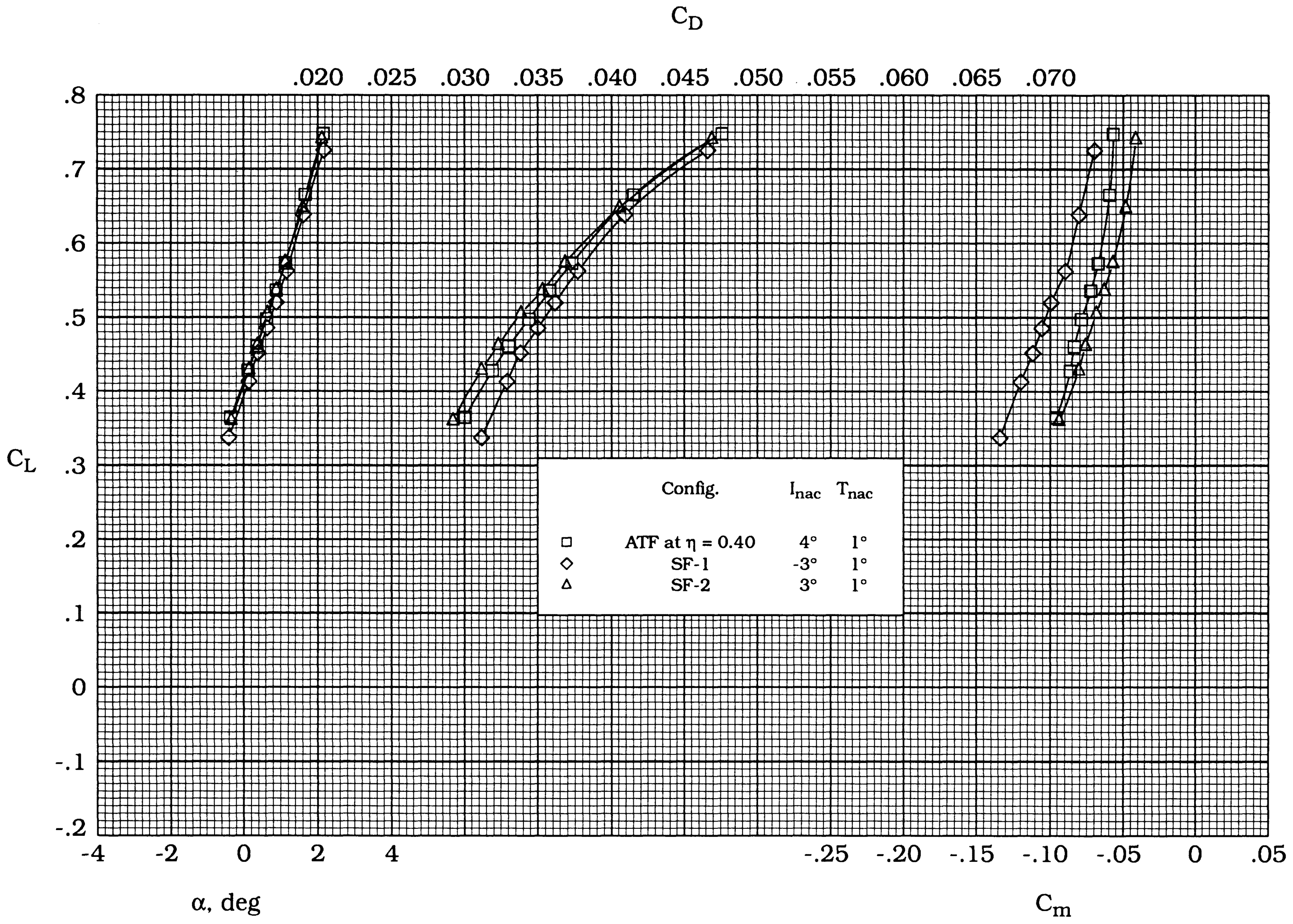

(d) $M_\infty = 0.76$.

Figure 20. Continued.

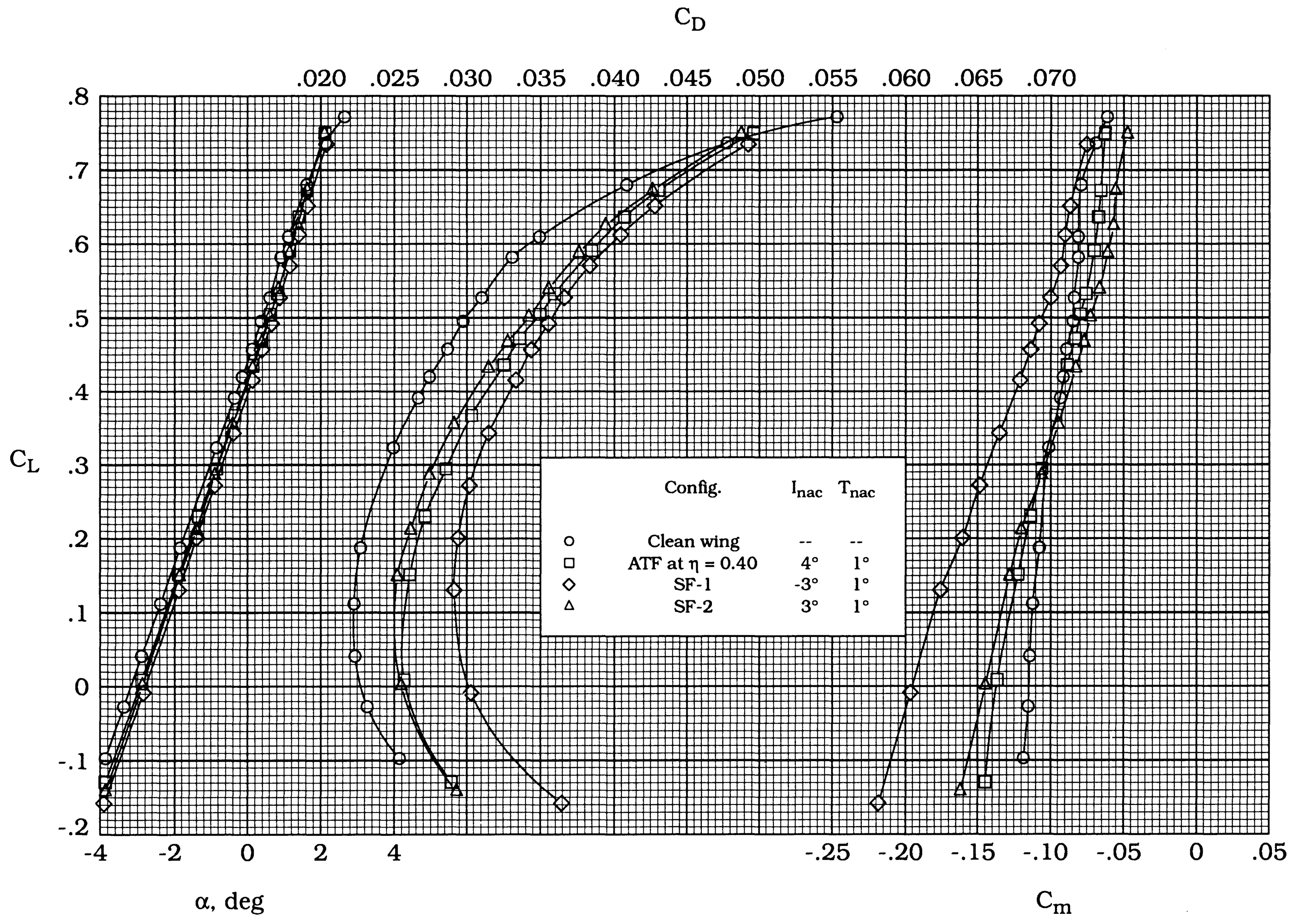

(e) $M_\infty = 0.77$.

Figure 20. Continued.

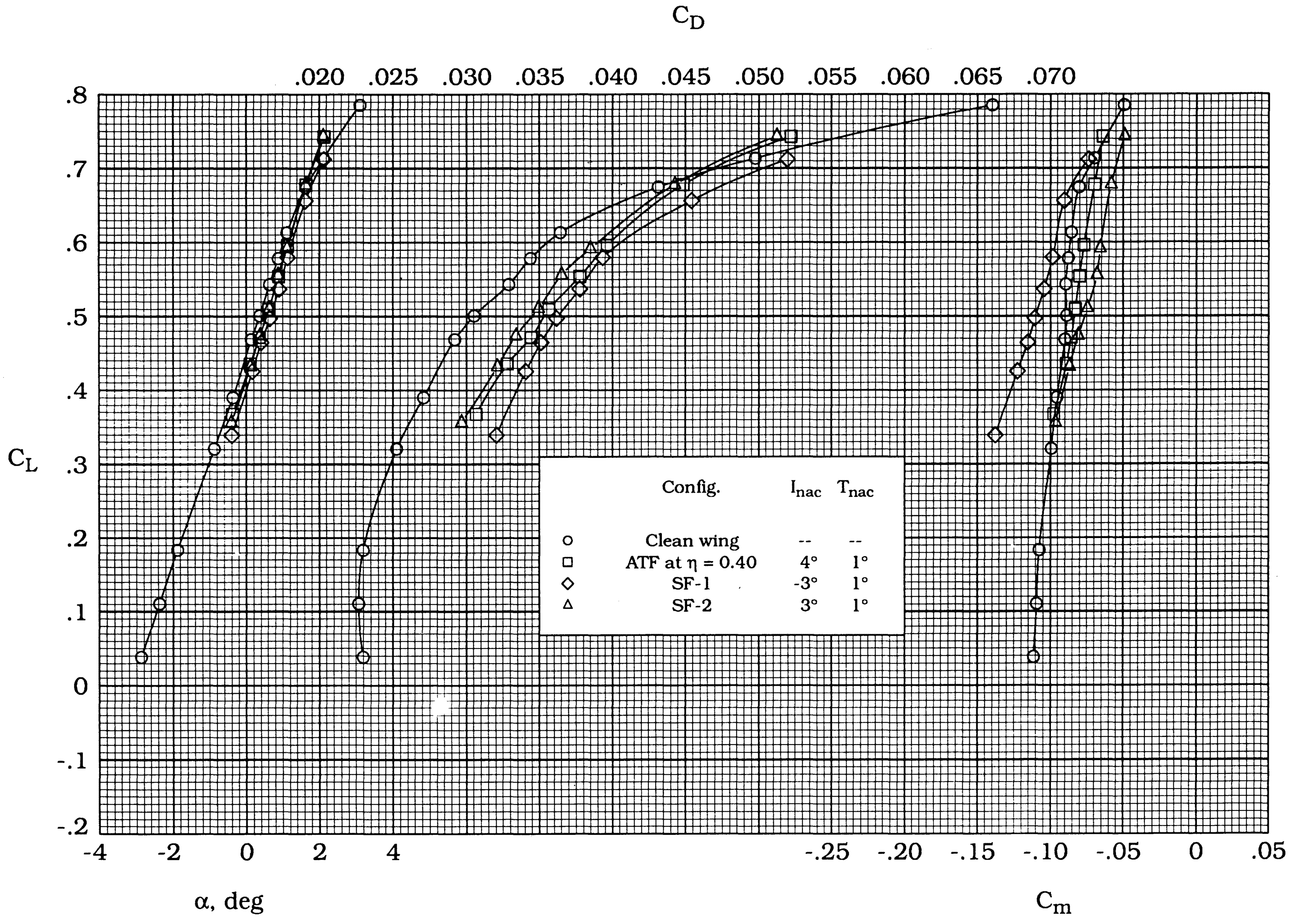

(f) $M_\infty = 0.78$.

Figure 20. Continued.

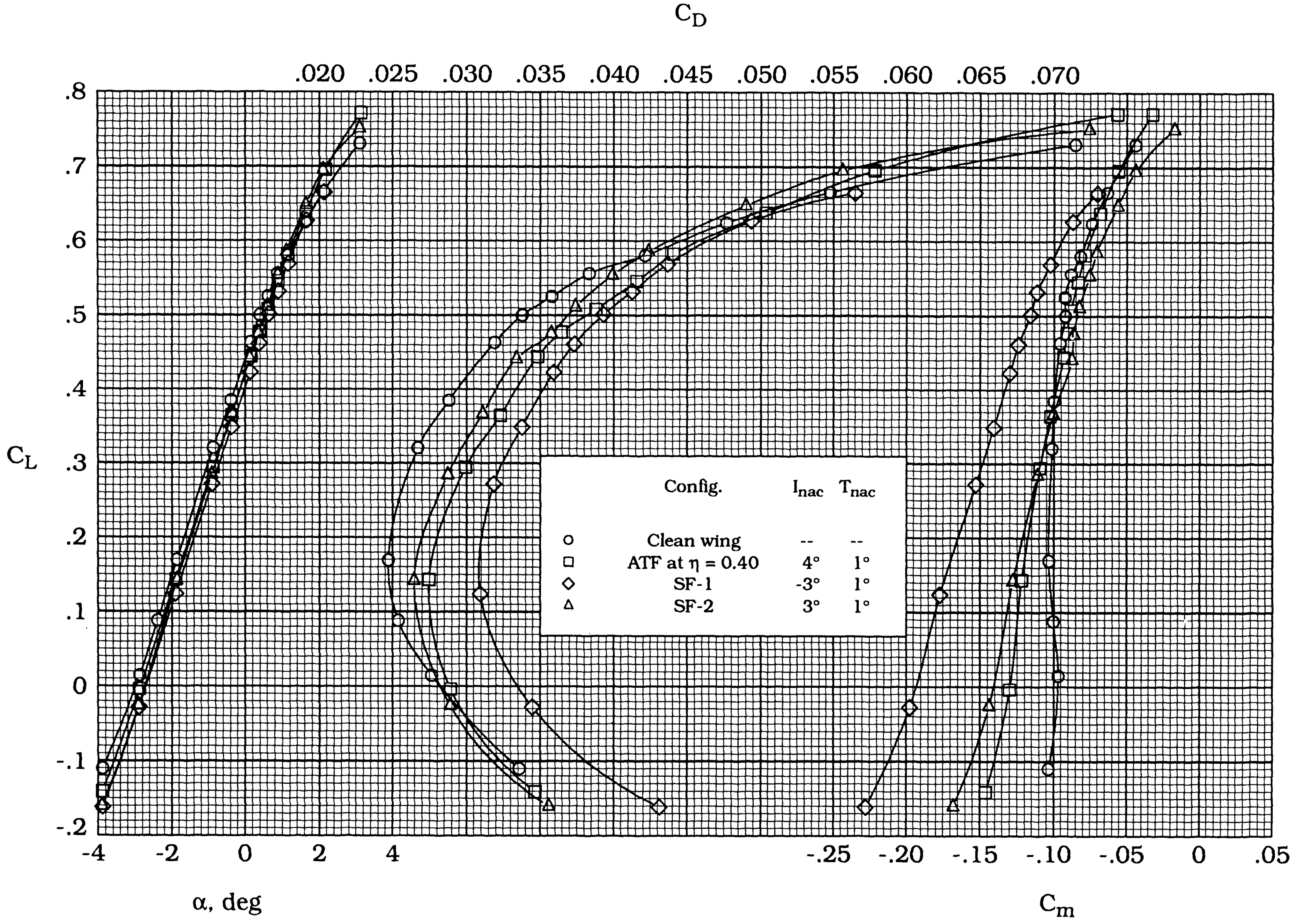

(g) $M_\infty = 0.80$.

Figure 20. Concluded.

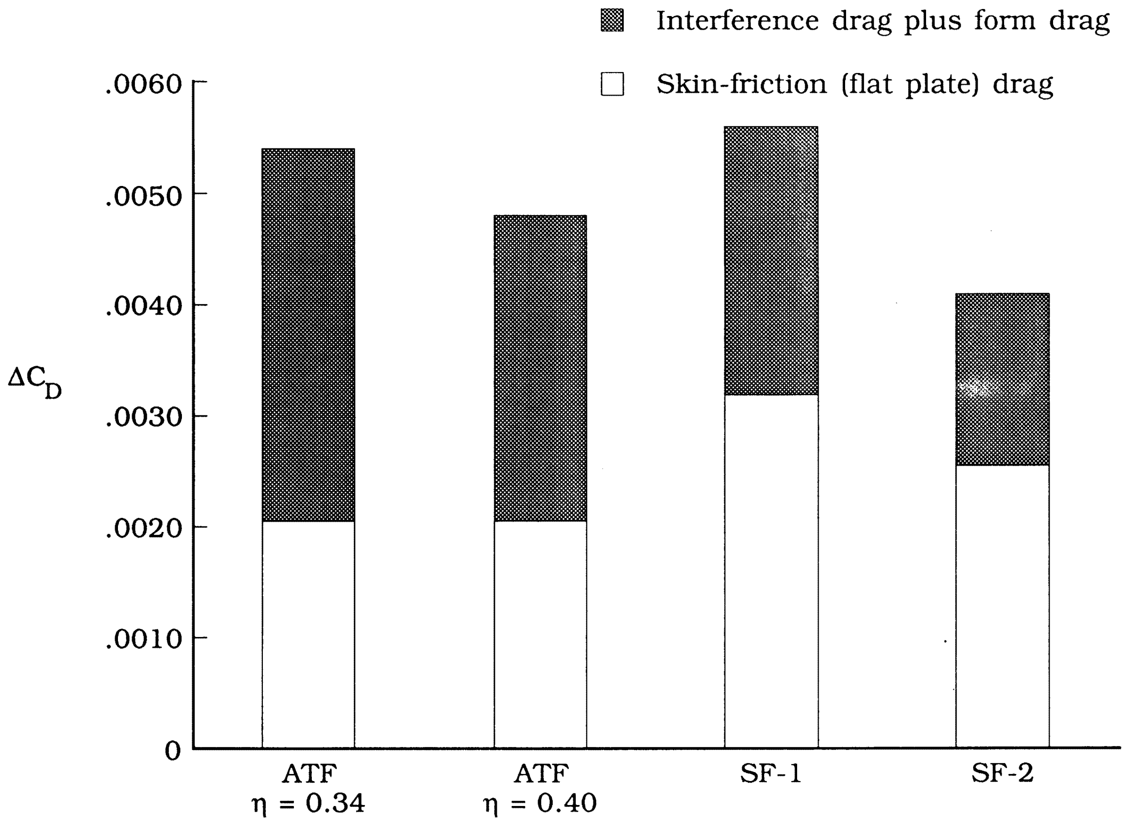

Figure 21. Installation drag coefficient increment for all nacelle configurations at $M_\infty = 0.77$ and $C_L = 0.55$.

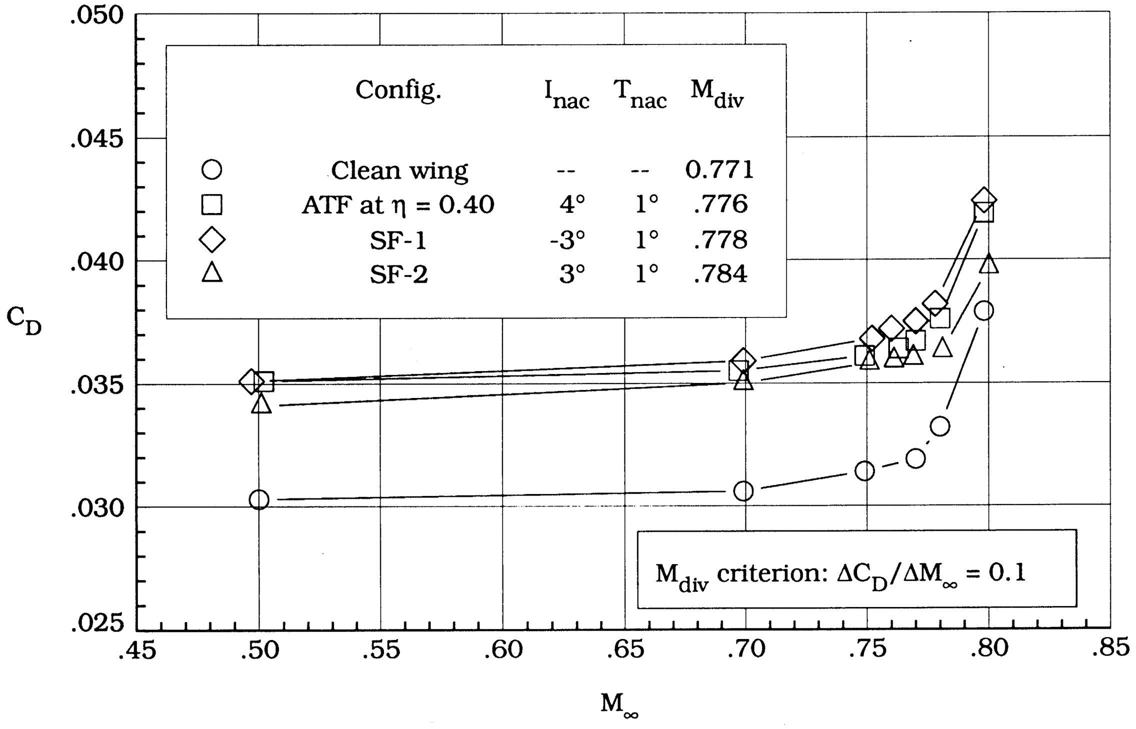

Figure 22. Model drag-rise characteristics with and without nacelles at $C_L = 0.55$.

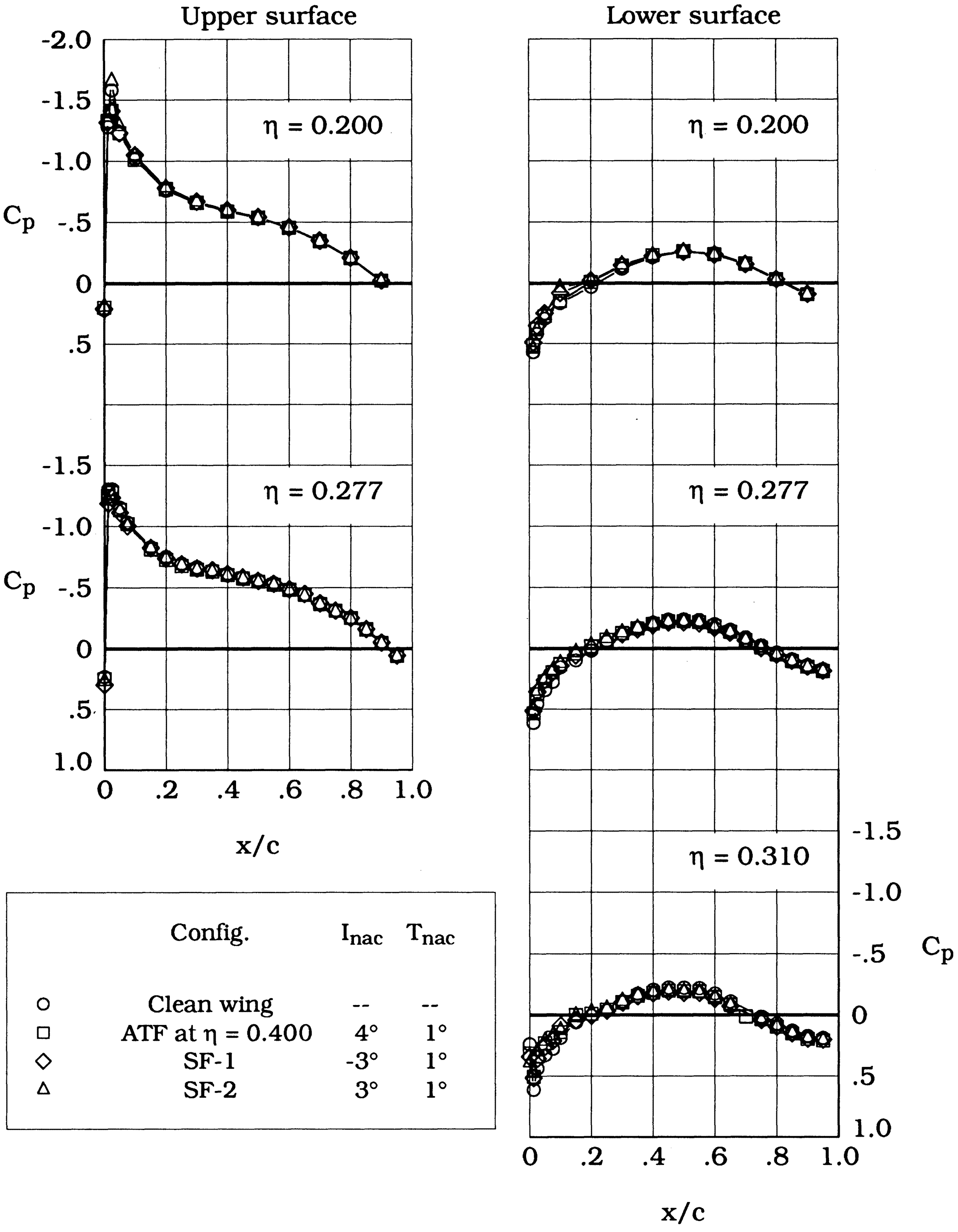

(a) Orifice locations at $\eta = 0.200$, 0.277, and 0.310.

Figure 23. Effects of nacelles installed at $\eta = 0.400$ on wing pressure distributions at $M_\infty = 0.50$ and $C_L \approx 0.55$.

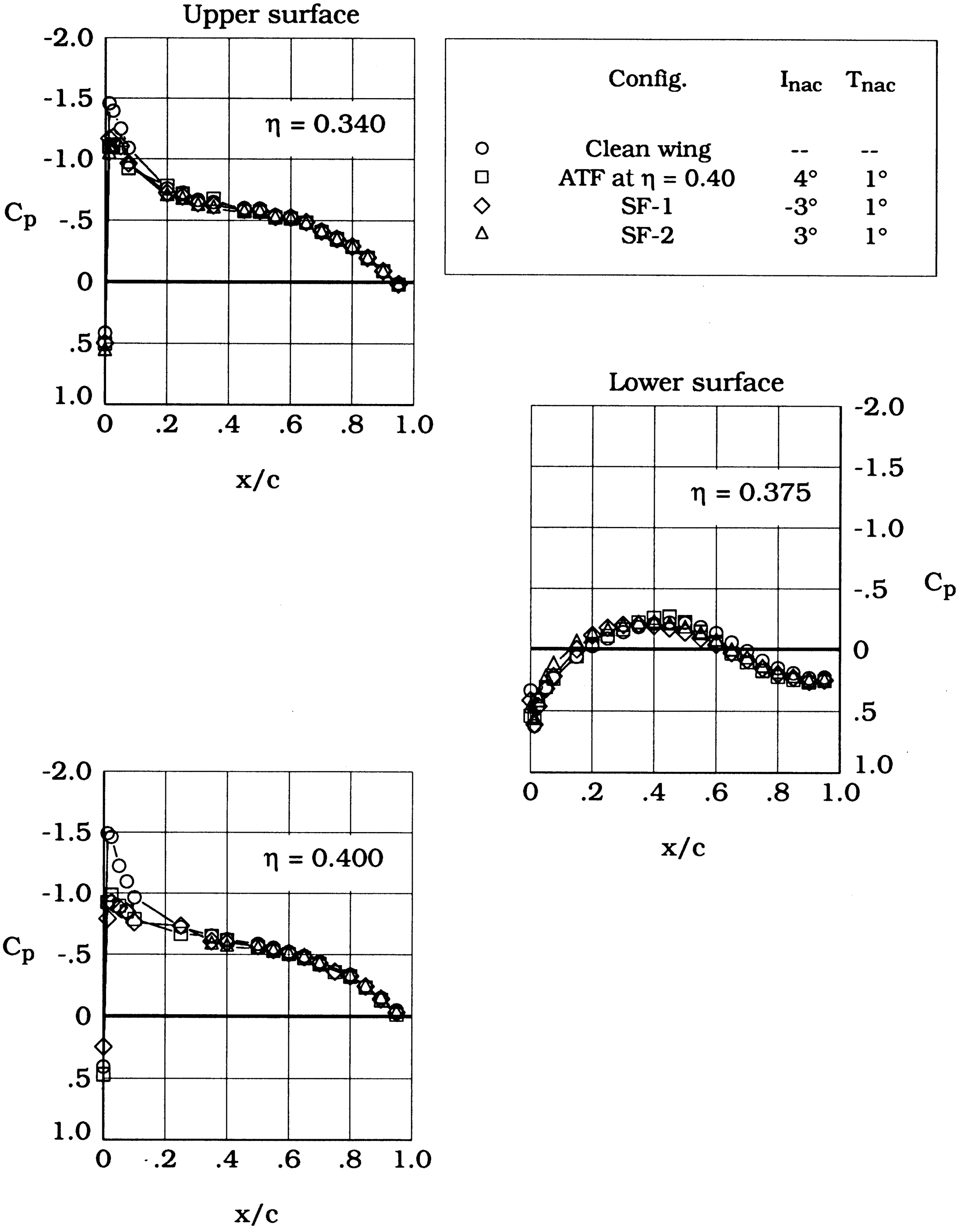

(b) $\eta = 0.340, 0.375$, and 0.400.

Figure 23. Continued.

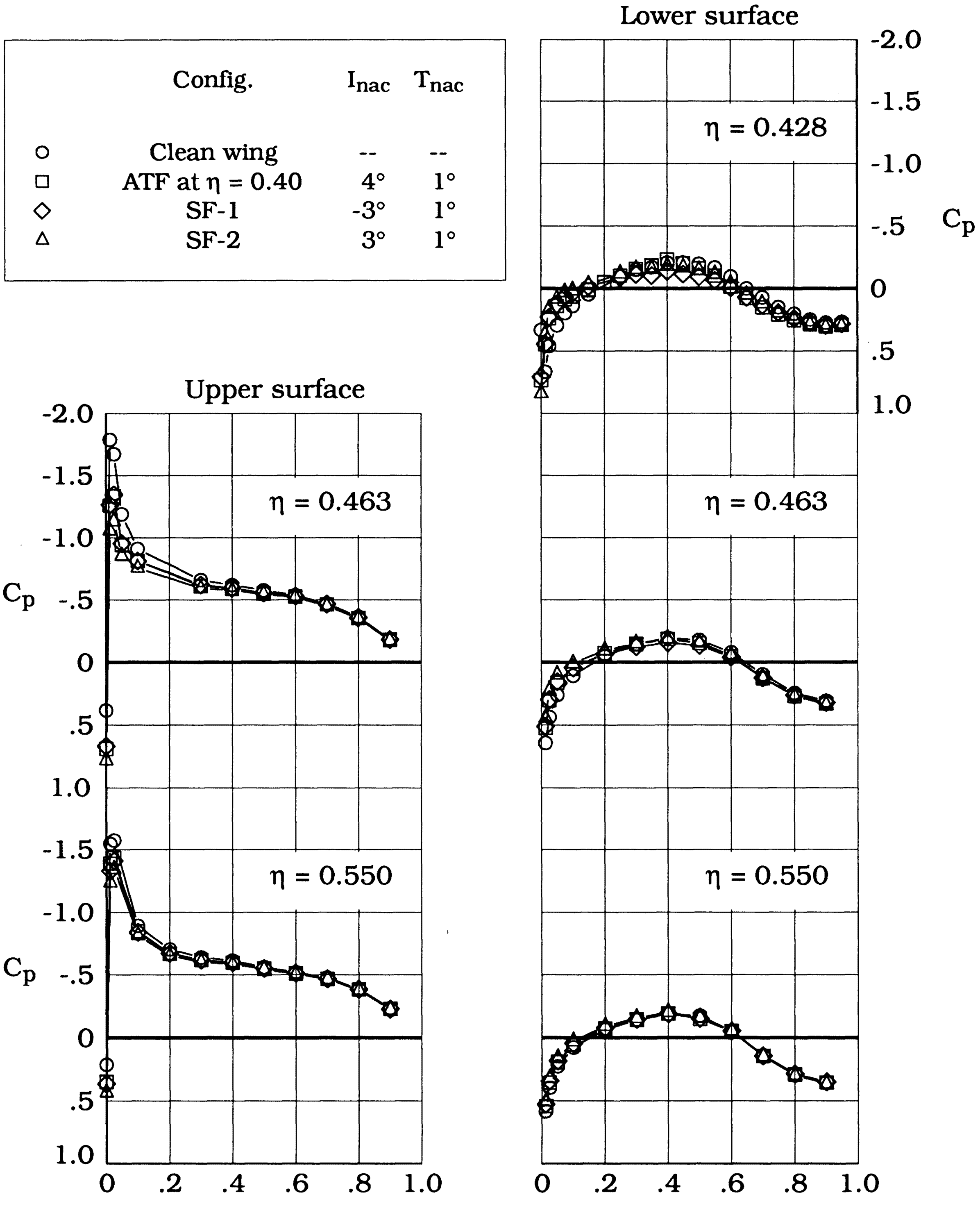

(c) $\eta = 0.428$, 0.463, and 0.550.

Figure 23. Continued.

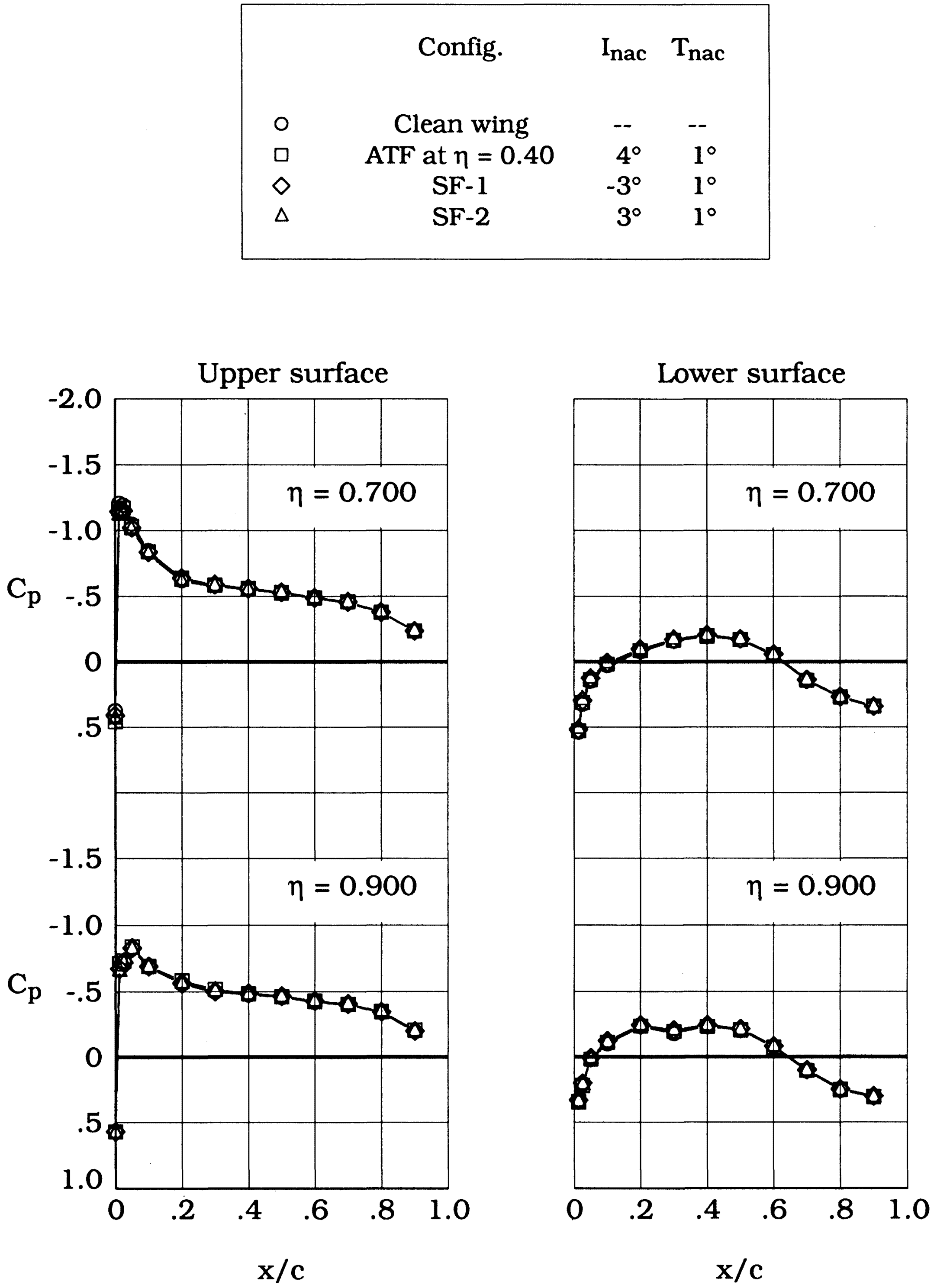

(d) $\eta = 0.700$ and 0.900.

Figure 23. Concluded.

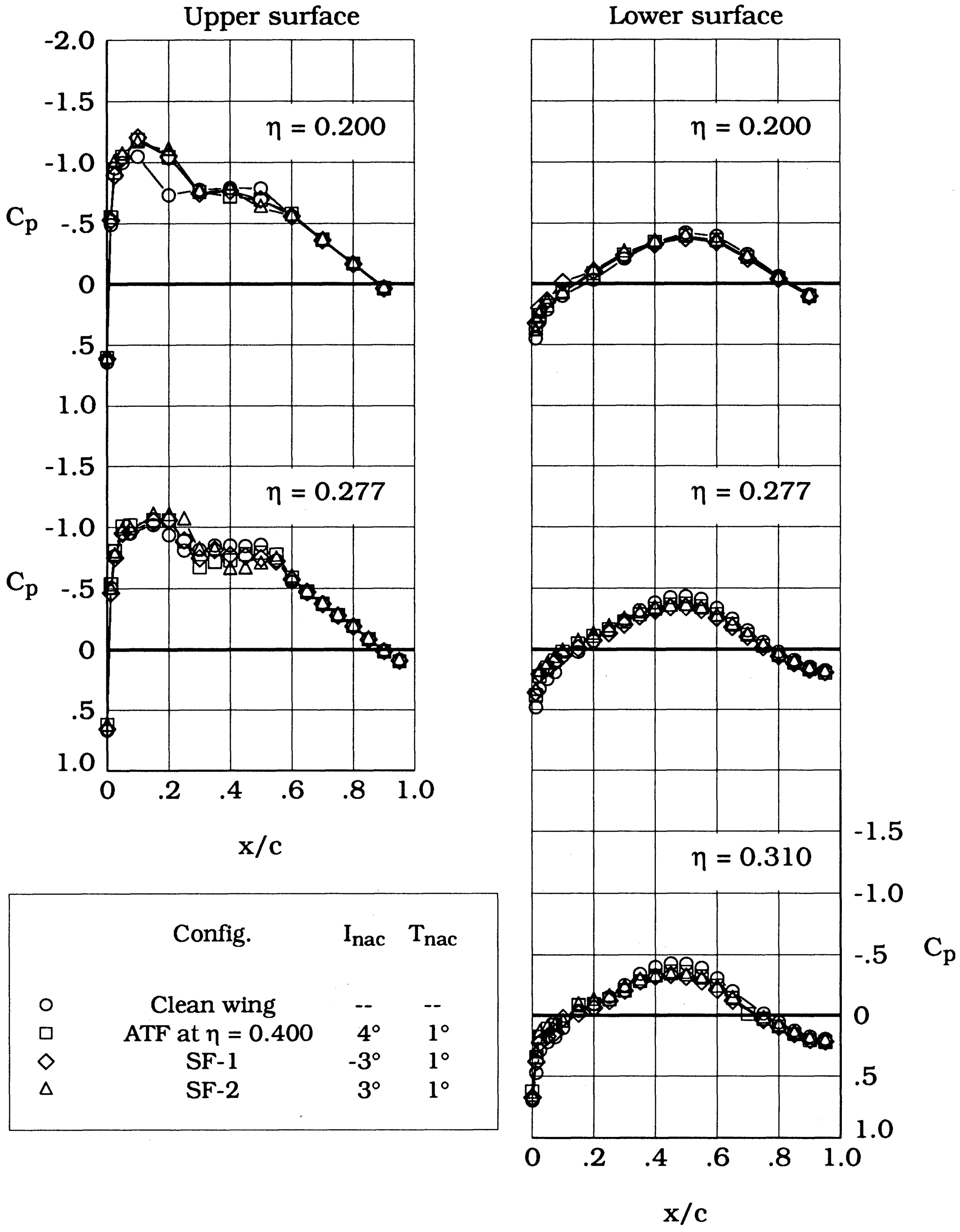

(a) $\eta = 0.200$, 0.277, and 0.310.

Figure 24. Effects of nacelles installed at $\eta = 0.400$ on wing pressure distributions at $M_\infty = 0.77$ and $C_L \approx 0.55$.

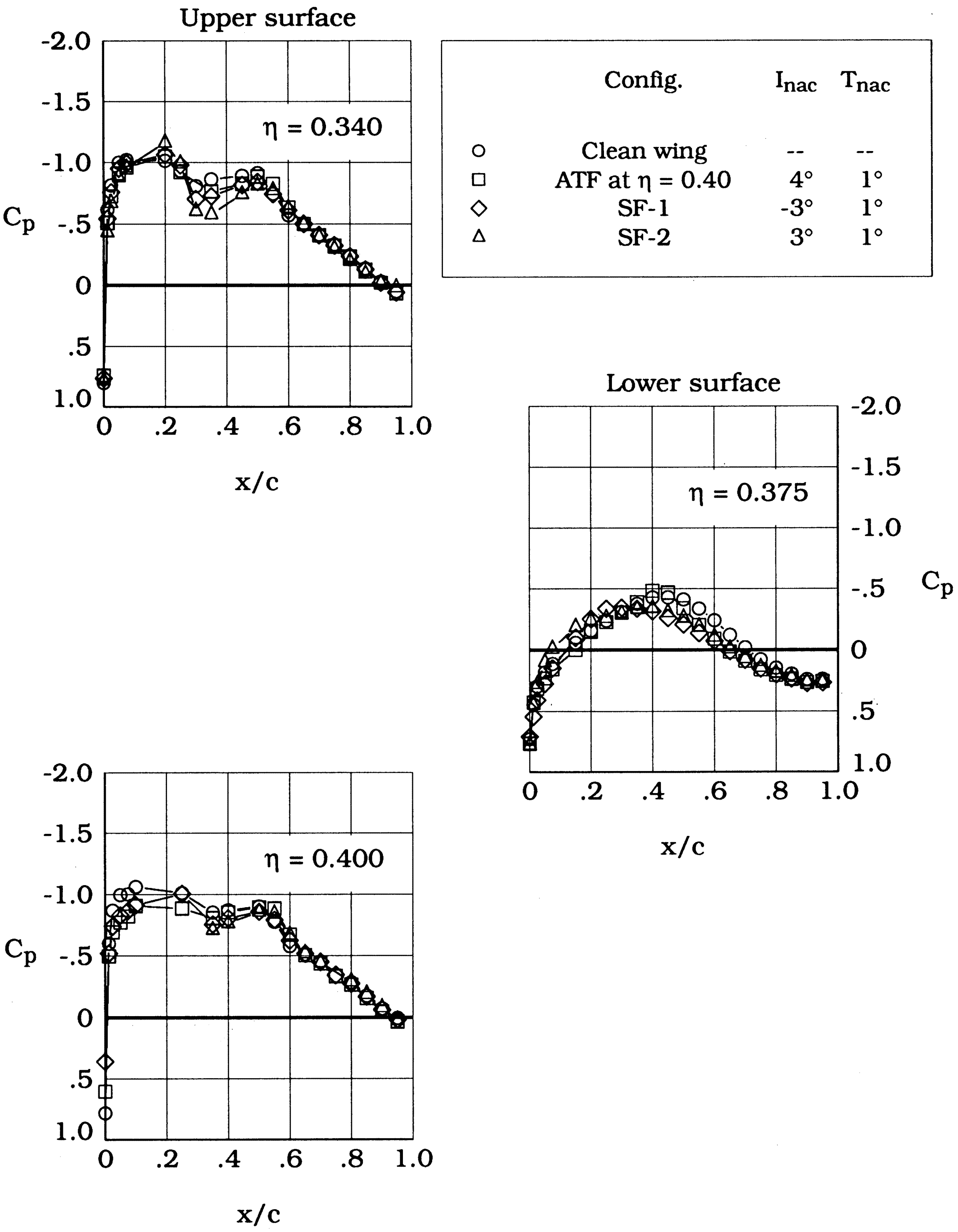

(b) $\eta = 0.340$, 0.375, and 0.400.

Figure 24. Continued.

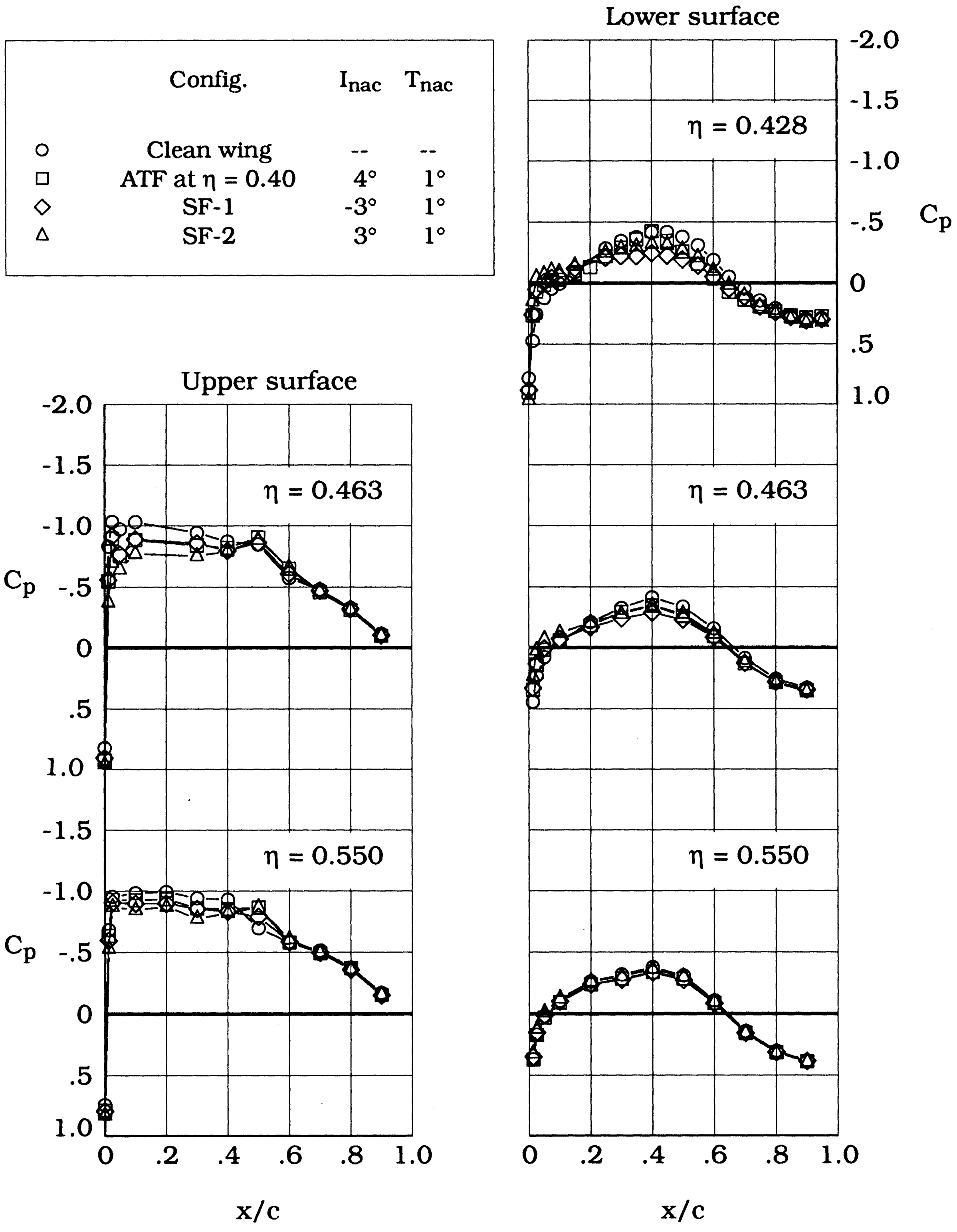

(c) η = 0.428, 0.463, and 0.550.

Figure 24. Continued.

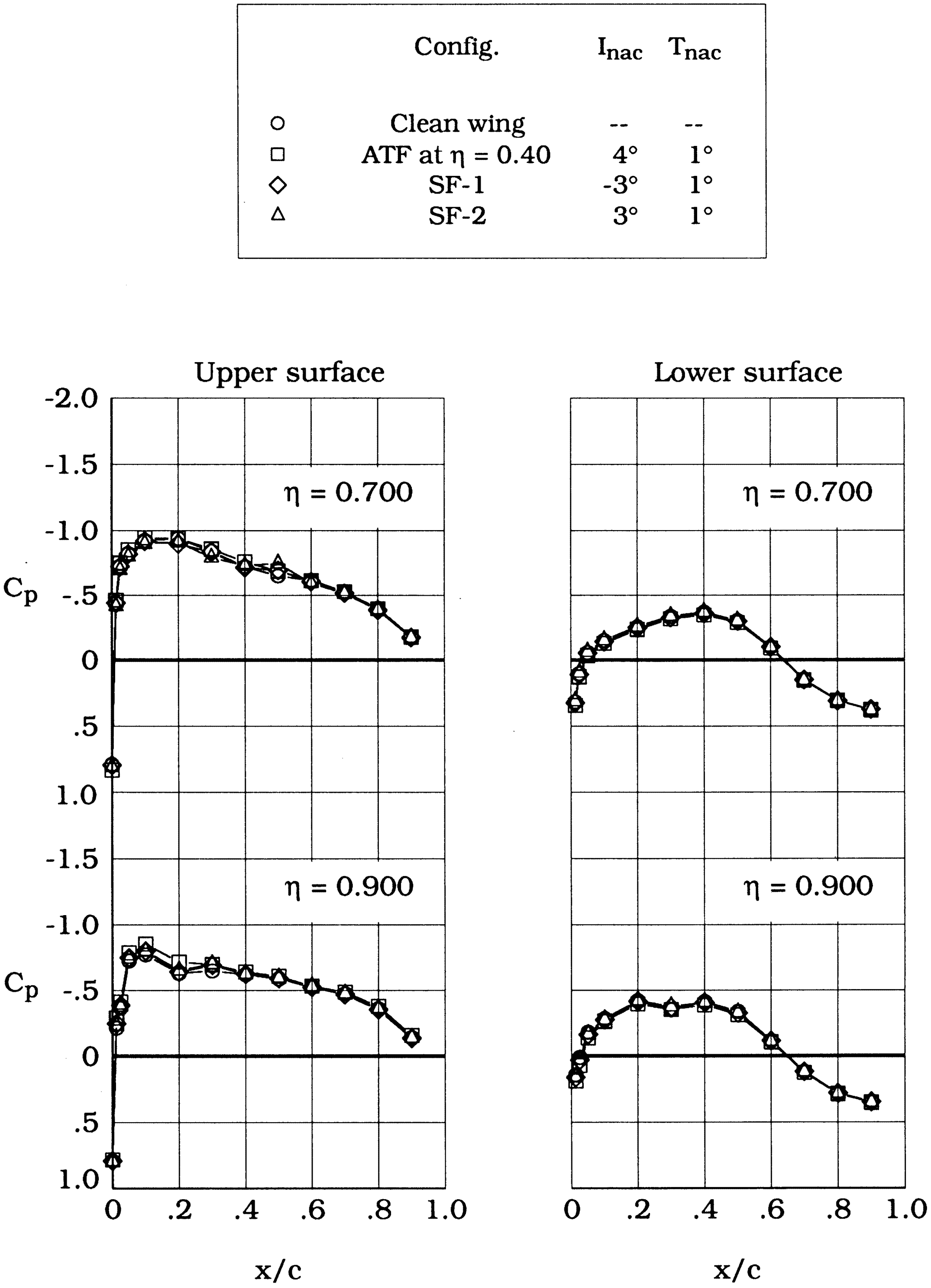

(d) $\eta = 0.700$ and 0.900.

Figure 24. Concluded.

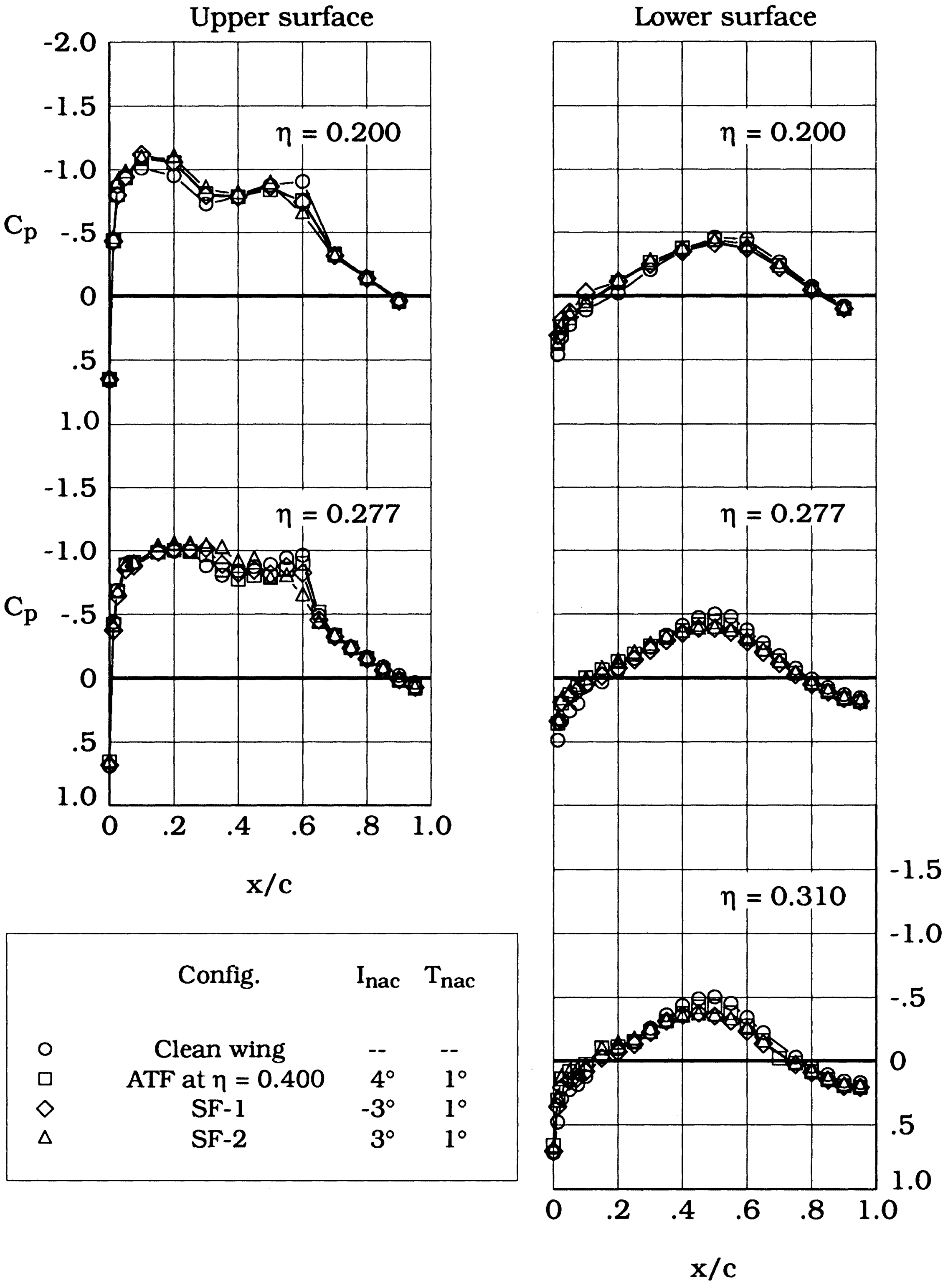

(a) $\eta = 0.200$, 0.277, and 0.310.

Figure 25. Effects of nacelles installed at $\eta = 0.400$ on wing pressure distributions at $M_\infty = 0.80$ and $C_L \approx 0.55$.

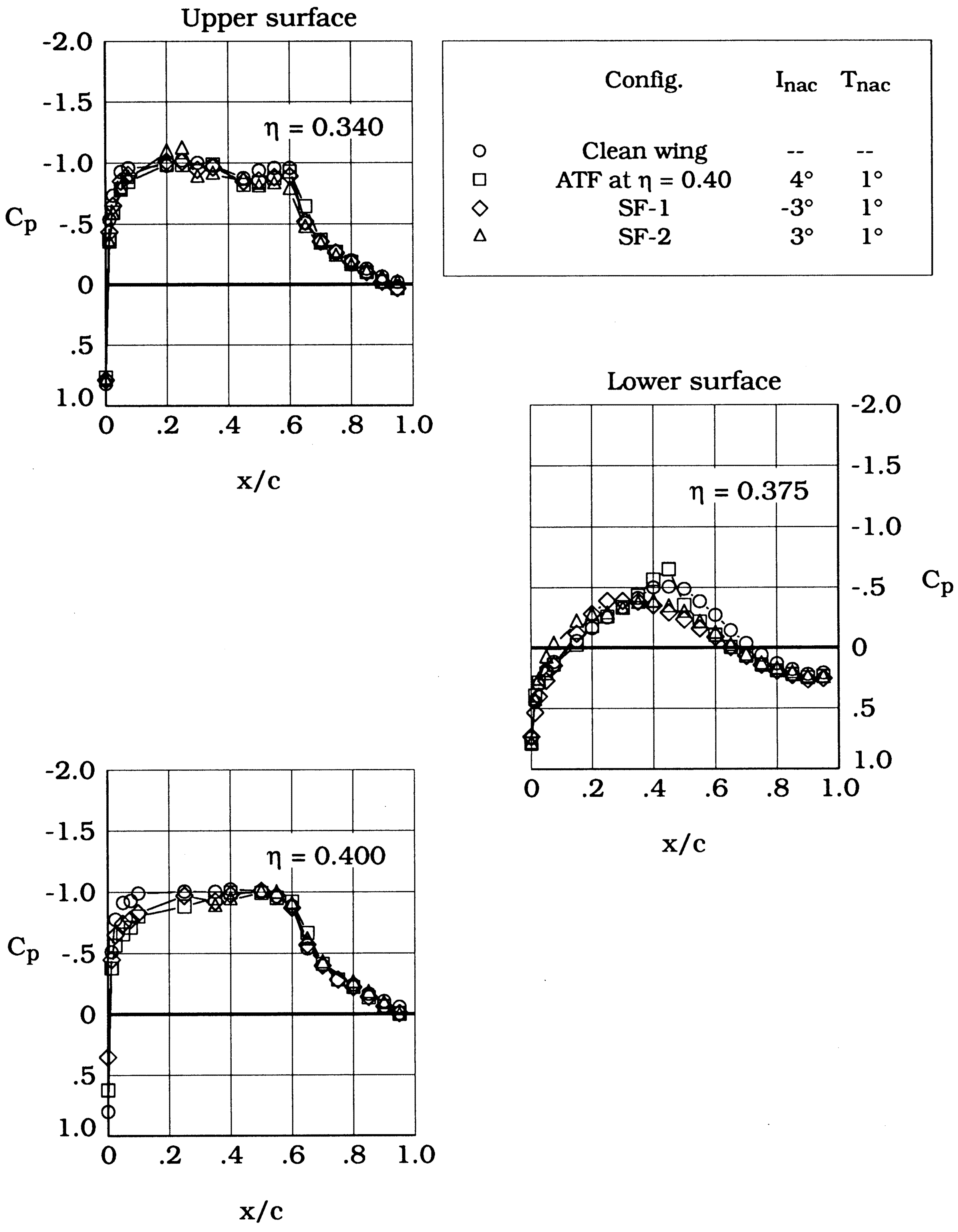

(b) $\eta = 0.340$, 0.375, and 0.400.

Figure 25. Continued.

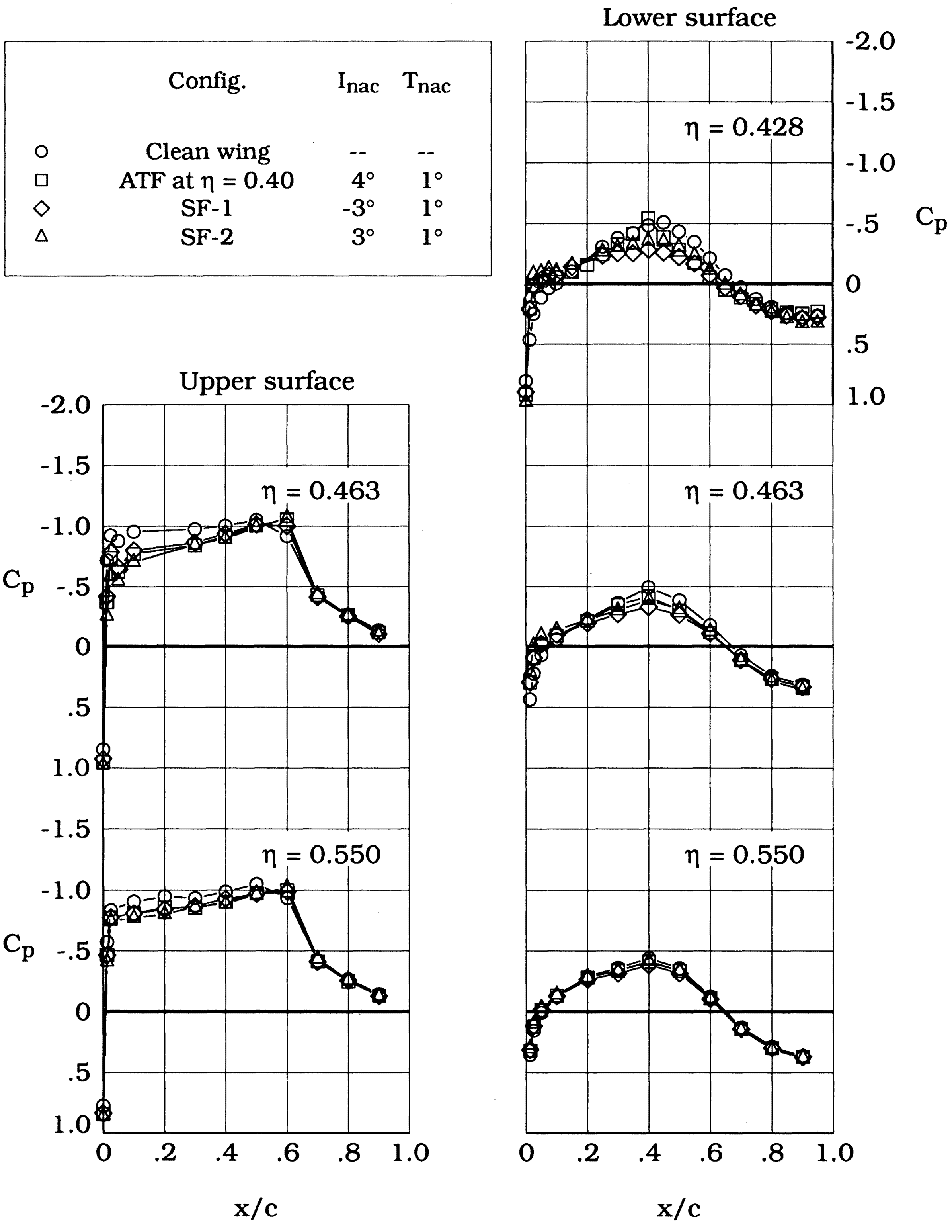

(c) $\eta = 0.428$, 0.463, and 0.550.

Figure 25. Continued.

	Config.	I_{nac}	T_{nac}
○	Clean wing	--	--
□	ATF at η = 0.40	4°	1°
◇	SF-1	-3°	1°
△	SF-2	3°	1°

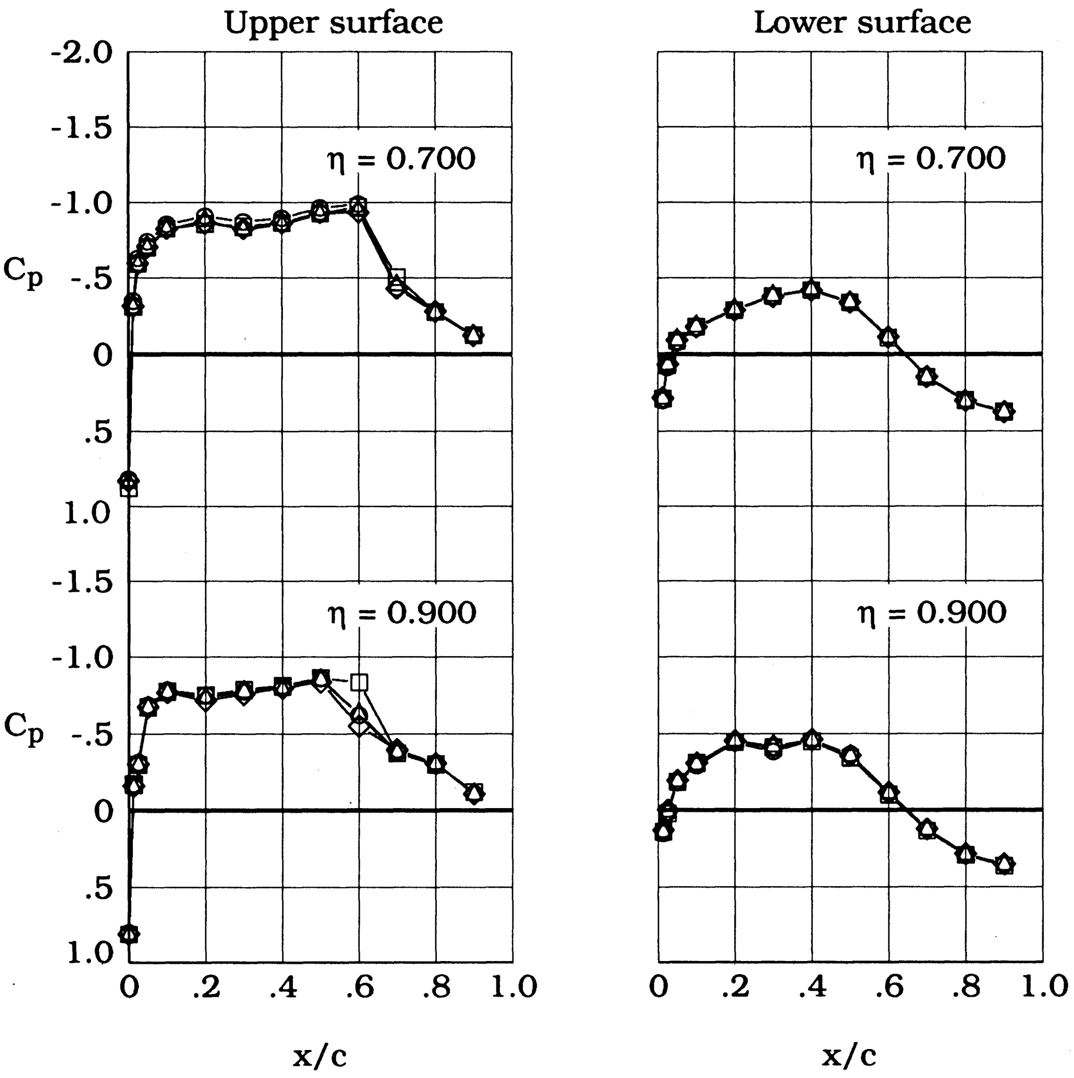

(d) $\eta = 0.700$ and 0.900.

Figure 25. Concluded.

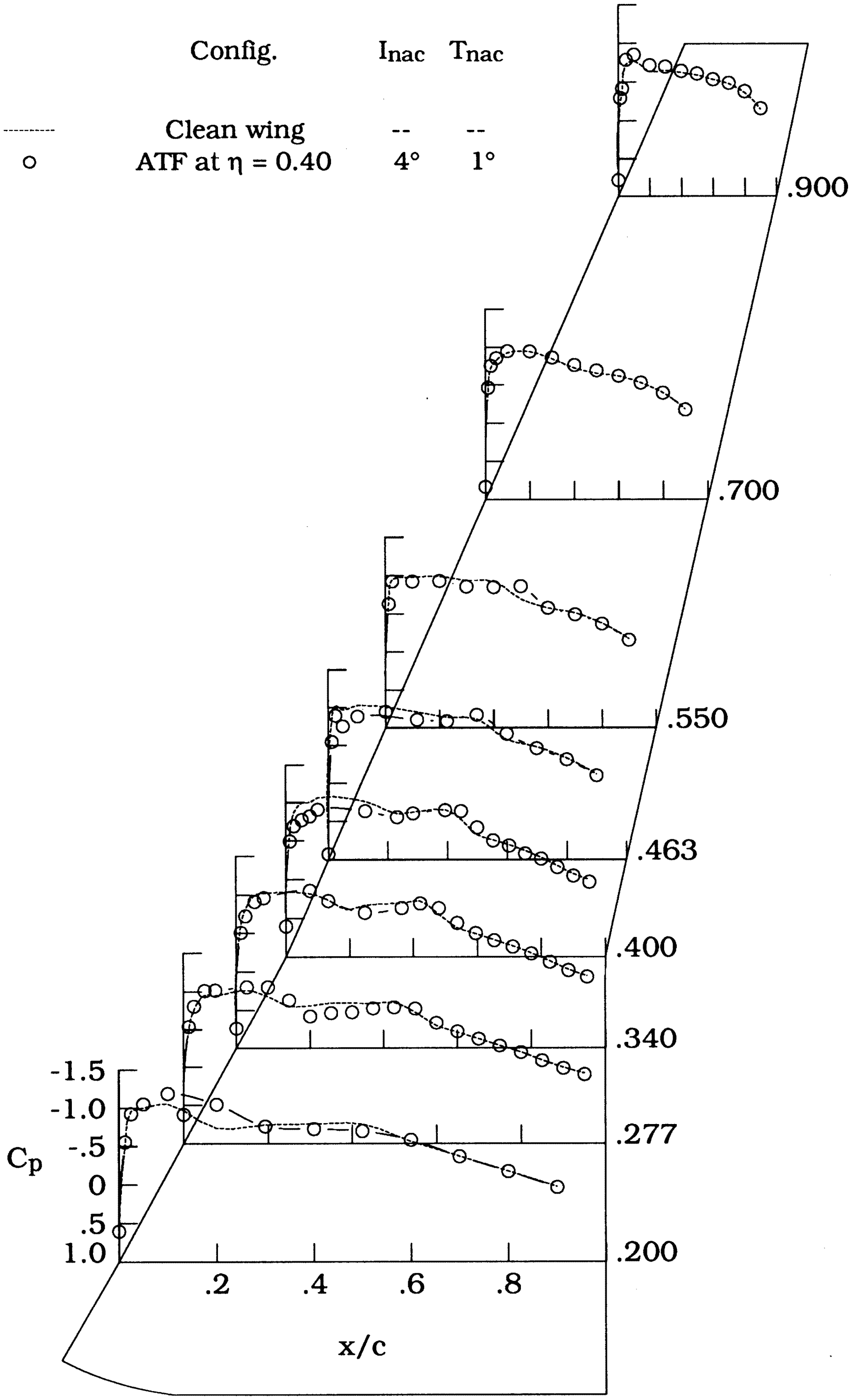

(a) Upper surface.

Figure 26. Influence of ATF nacelles installed at $\eta = 0.40$ on wing surface pressure coefficients for $M_\infty = 0.77$ and $C_L \approx 0.55$. Semispan stations $y/(b/2) = 0.20$ to 0.90 given to right of plot.

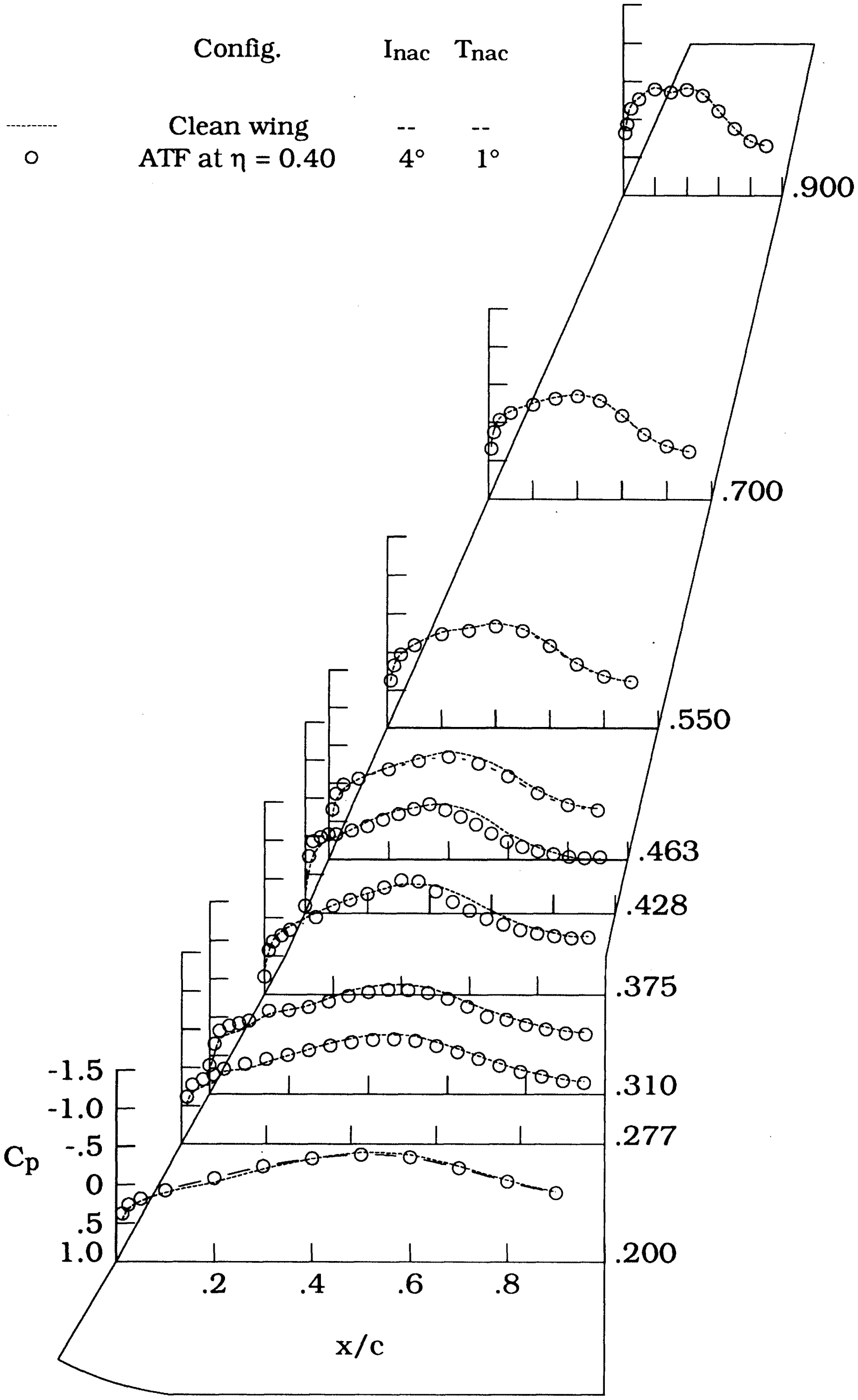

(b) Lower surface.

Figure 26. Concluded.

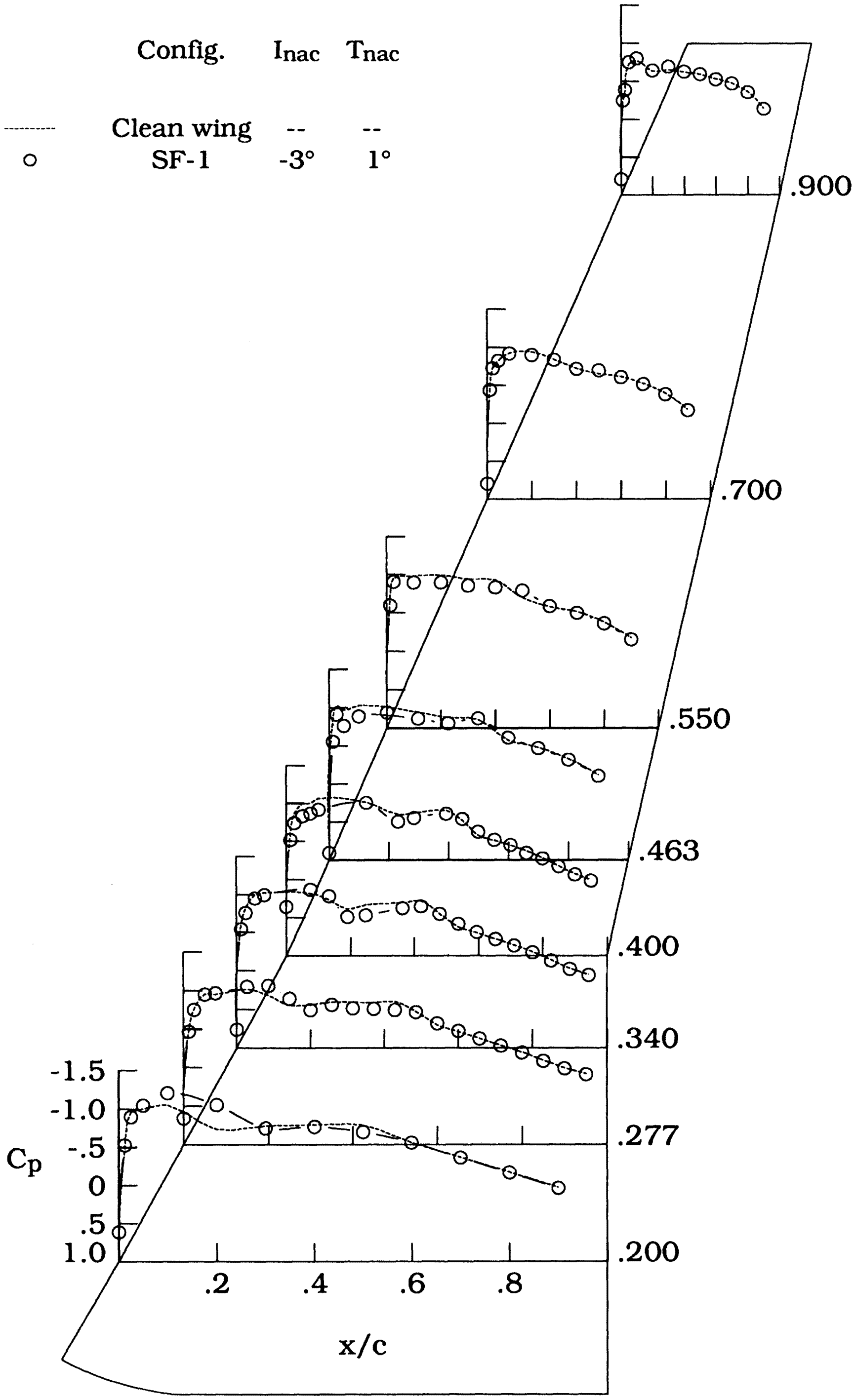

(a) Upper surface.

Figure 27. Influence of SF-1 nacelles installed at $\eta = 0.40$ on wing surface pressure coefficients for $M_\infty = 0.77$ and $C_L \approx 0.55$. Semispan stations $y/(b/2) = 0.20$ to 0.90 given to right of plot.

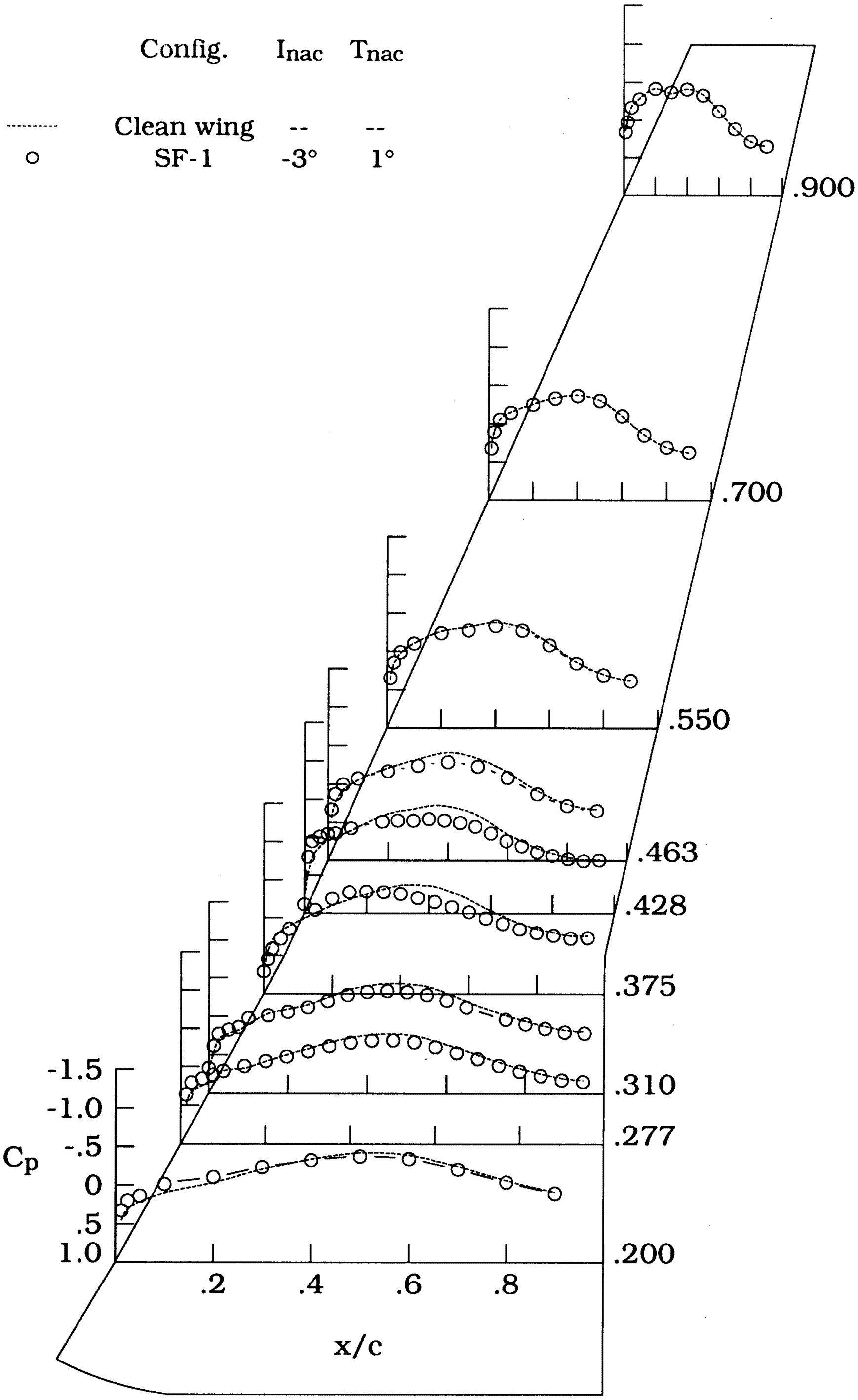

(b) Lower surface.

Figure 27. Concluded.

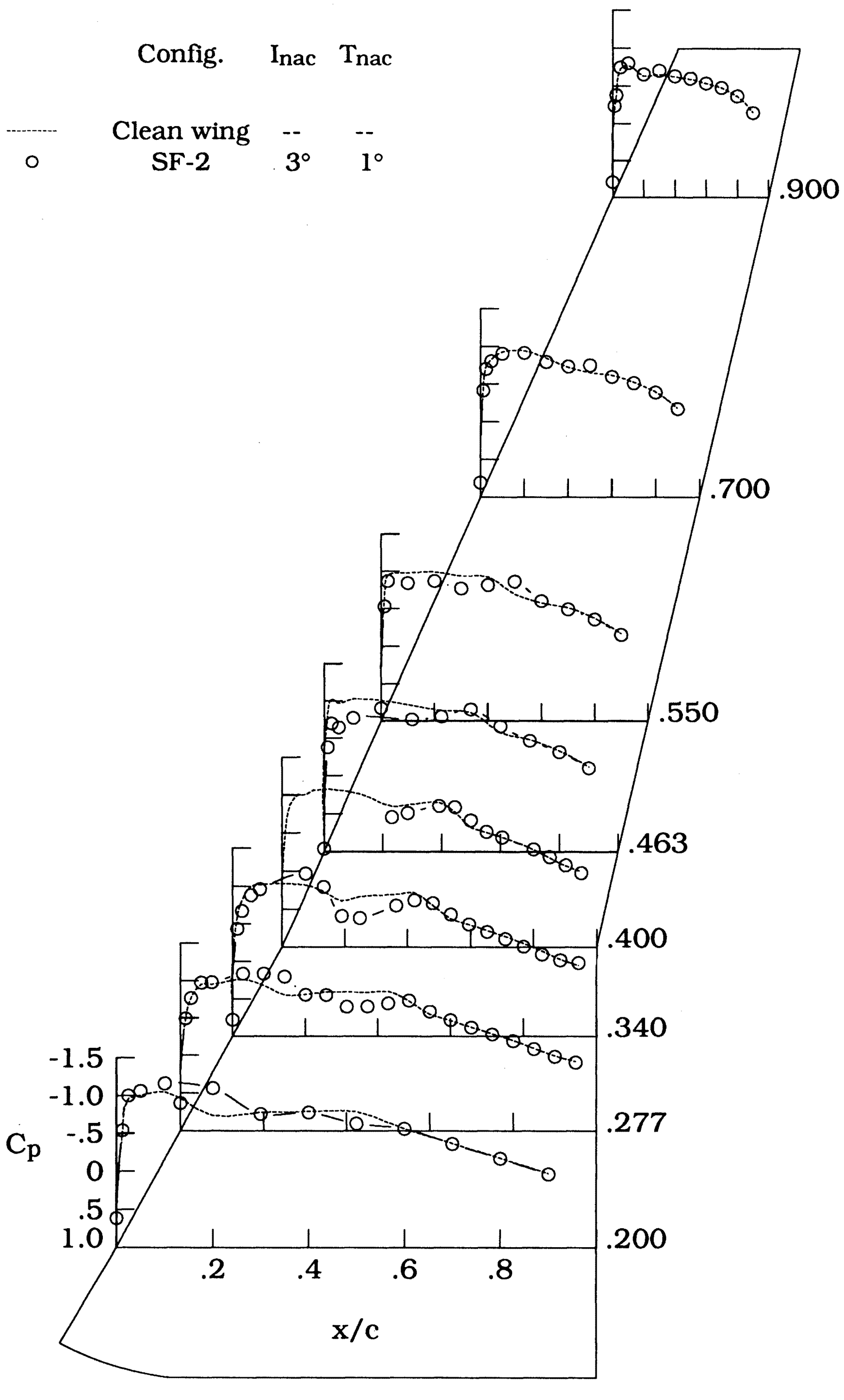

(a) Upper surface.

Figure 28. Influence of SF-2 nacelles installed at $\eta = 0.40$ on wing surface pressure coefficients for $M_\infty = 0.77$ and $C_L \approx 0.55$. Semispan stations $y/(b/2) = 0.20$ to 0.90 given to right of plot.

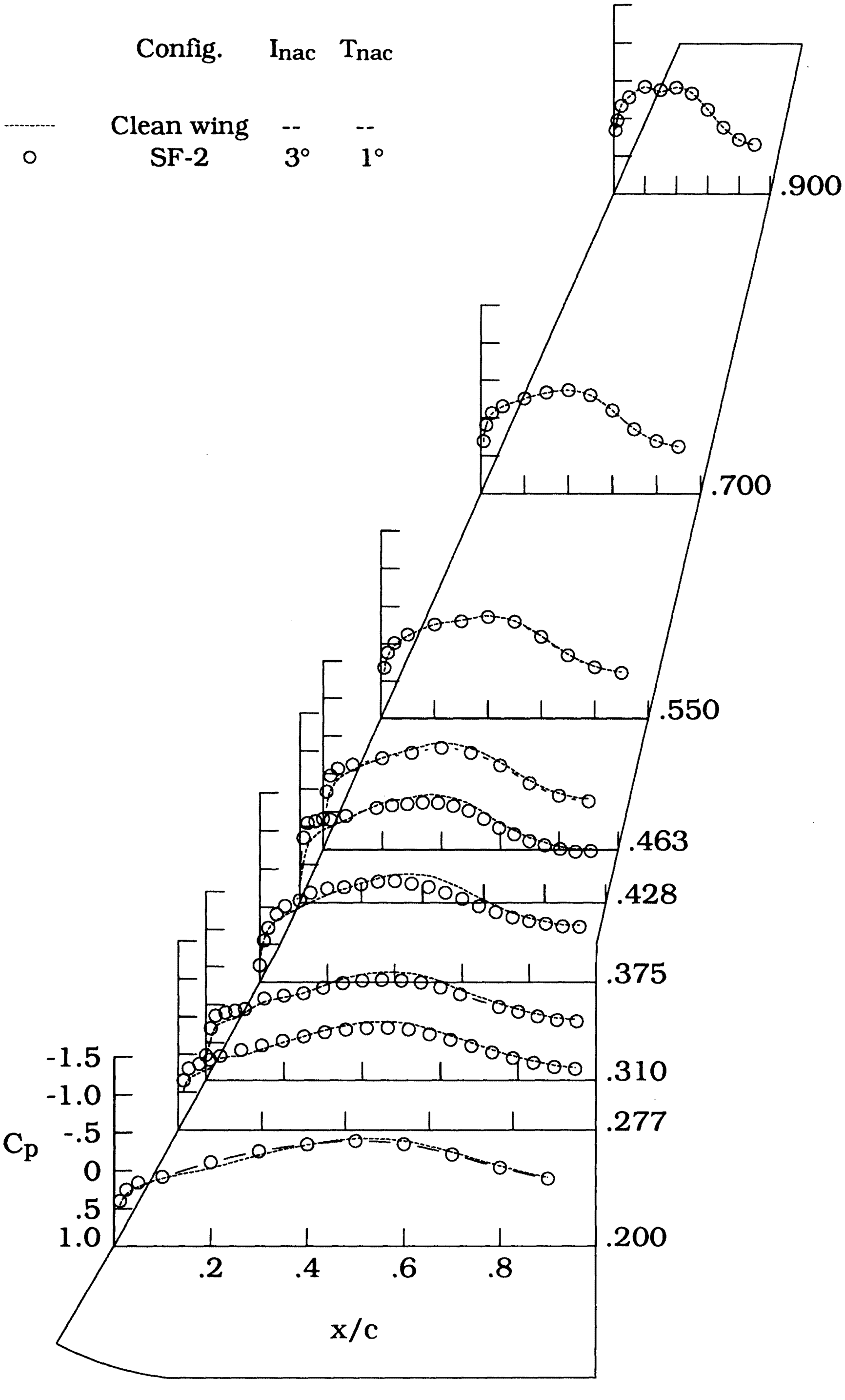

(b) Lower surface.

Figure 28. Concluded.

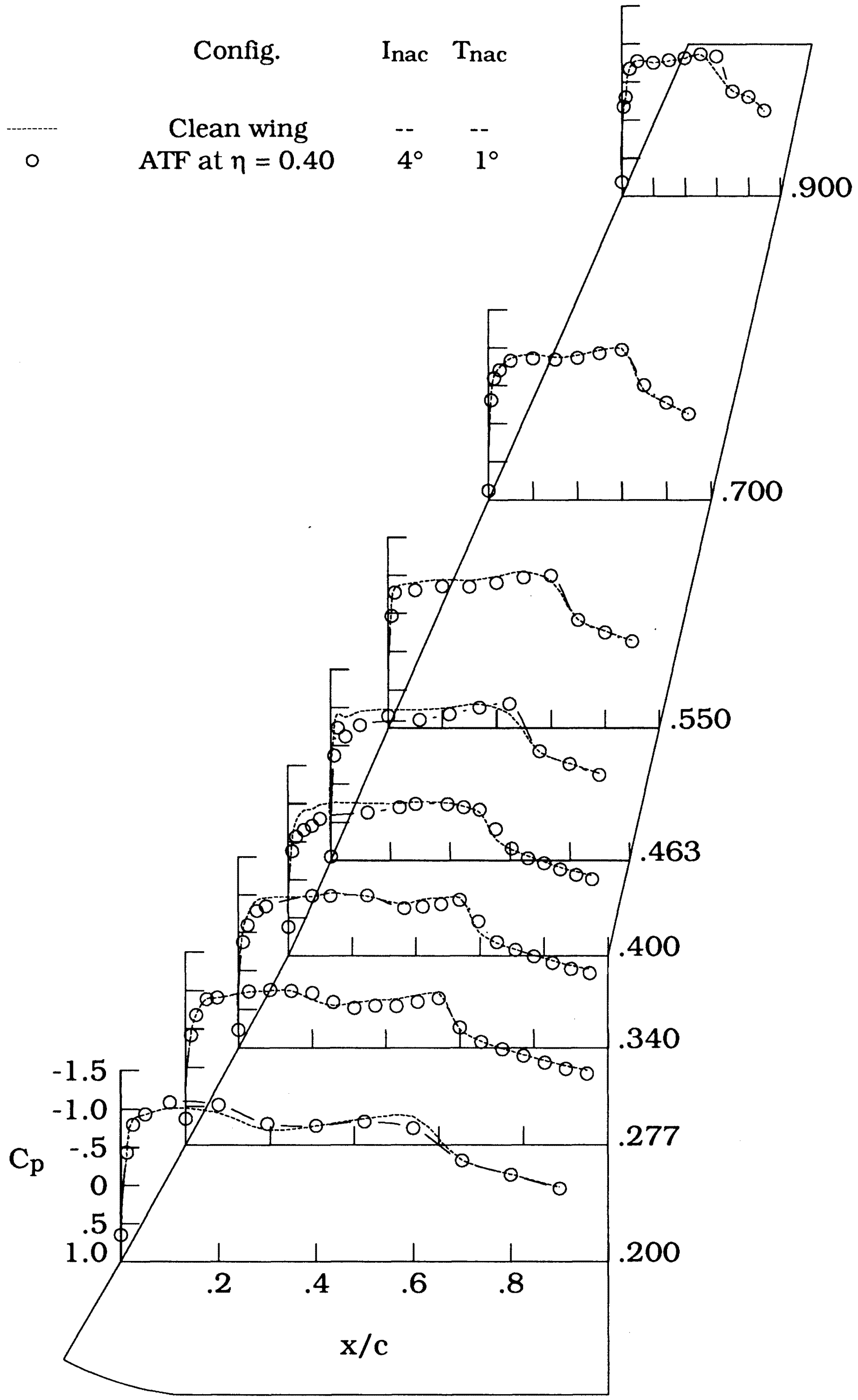

(a) Upper surface.

Figure 29. Influence of ATF nacelles installed at $\eta = 0.40$ on wing surface pressure coefficients for $M_\infty = 0.80$ and $C_L \approx 0.55$. Semispan stations $y/(b/2) = 0.20$ to 0.90 given to right of plot.

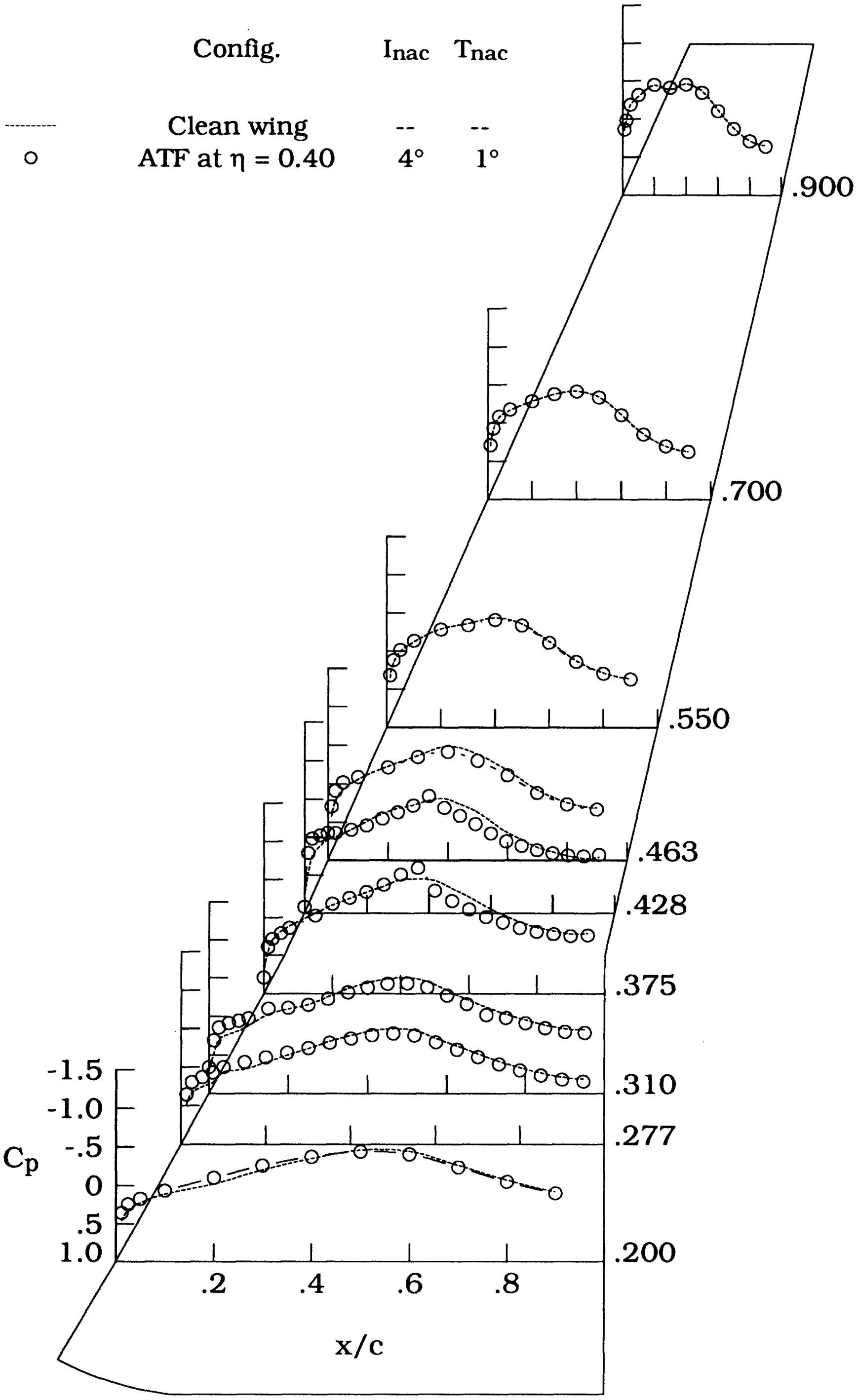

(b) Lower surface.

Figure 29. Concluded.

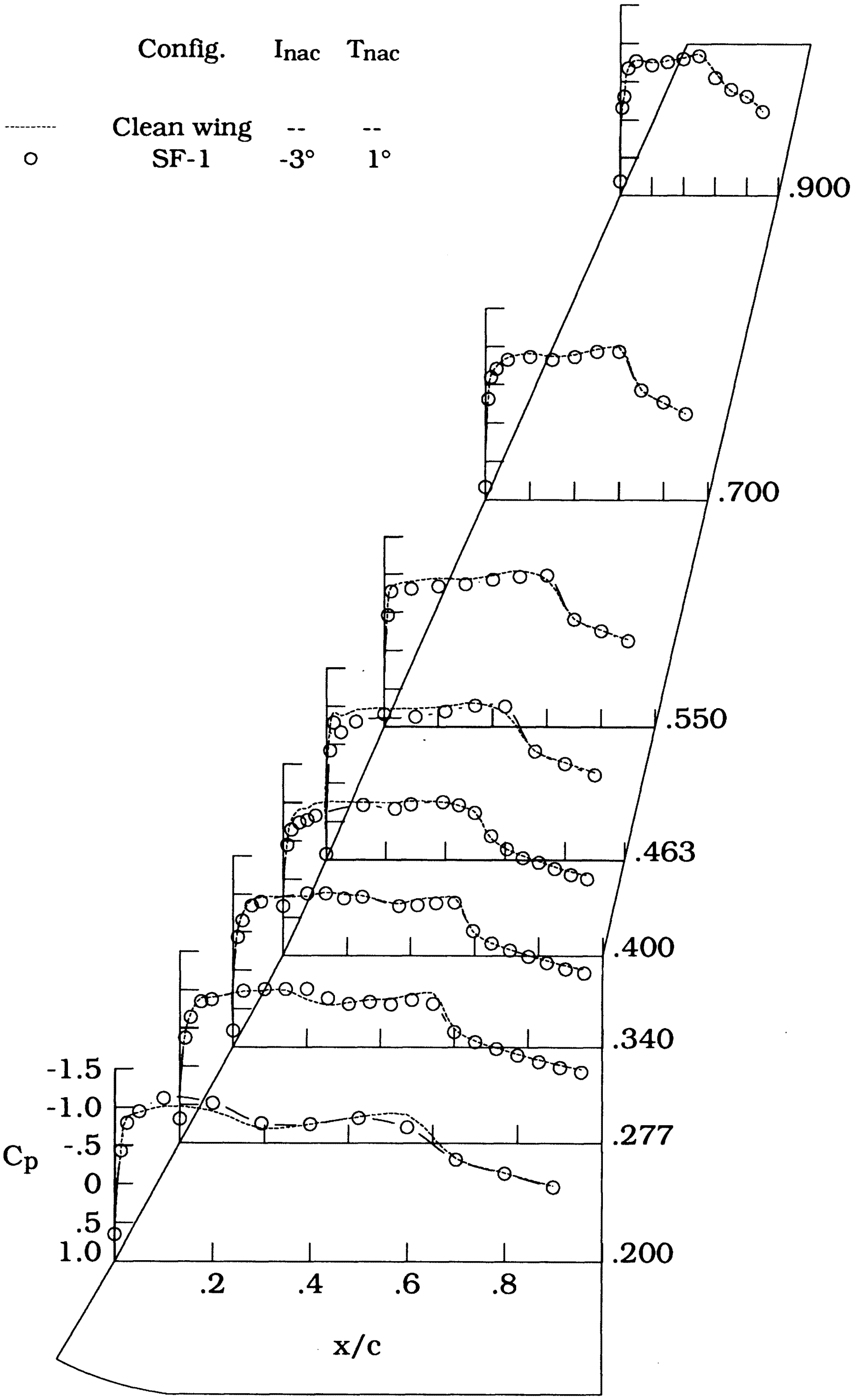

(a) Upper surface.

Figure 30. Influence of SF-1 nacelles installed at $\eta = 0.40$ on wing surface pressure coefficients for $M_{\infty} = 0.80$ and $C_L \approx 0.55$. Semispan stations $y/(b/2) = 0.20$ to 0.90 given to right of plot.

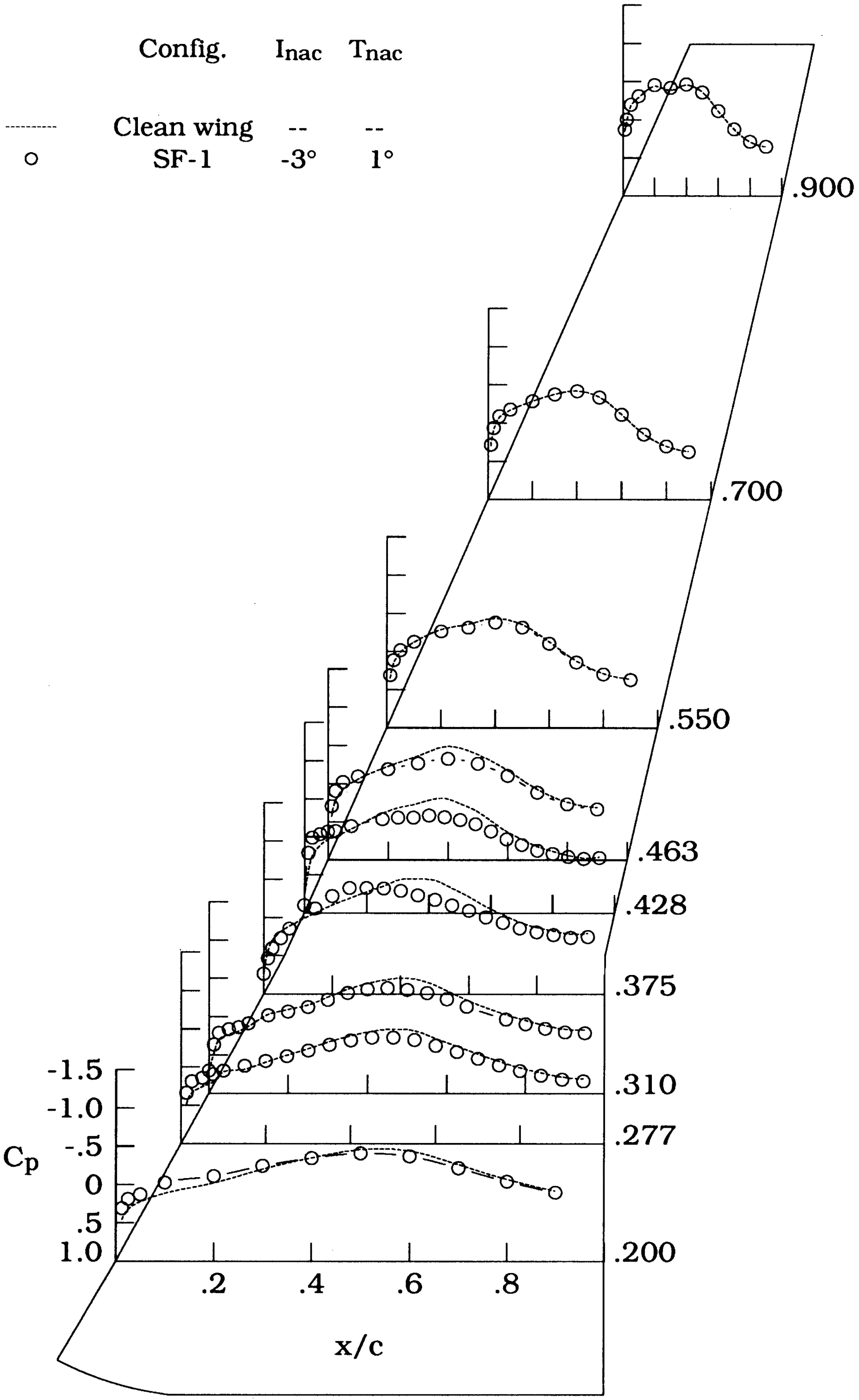

(b) Lower surface.

Figure 30. Concluded.

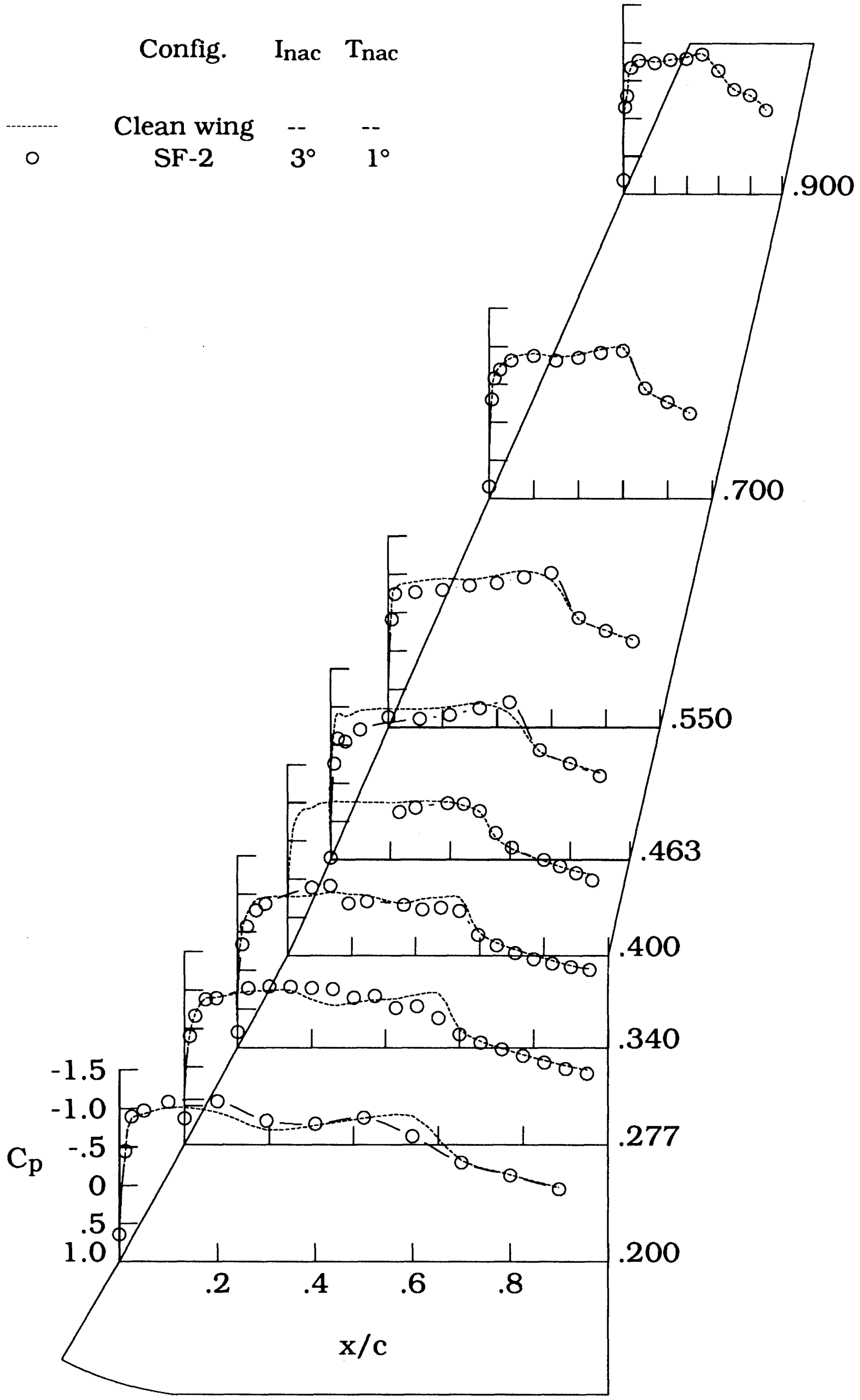

(a) Upper surface.

Figure 31. Influence of SF-2 nacelles installed at $\eta = 0.40$ on wing surface pressure coefficients for $M_\infty = 0.80$ and $C_L \approx 0.55$. Semispan stations $y/(b/2) = 0.20$ to 0.90 given to right of plot.

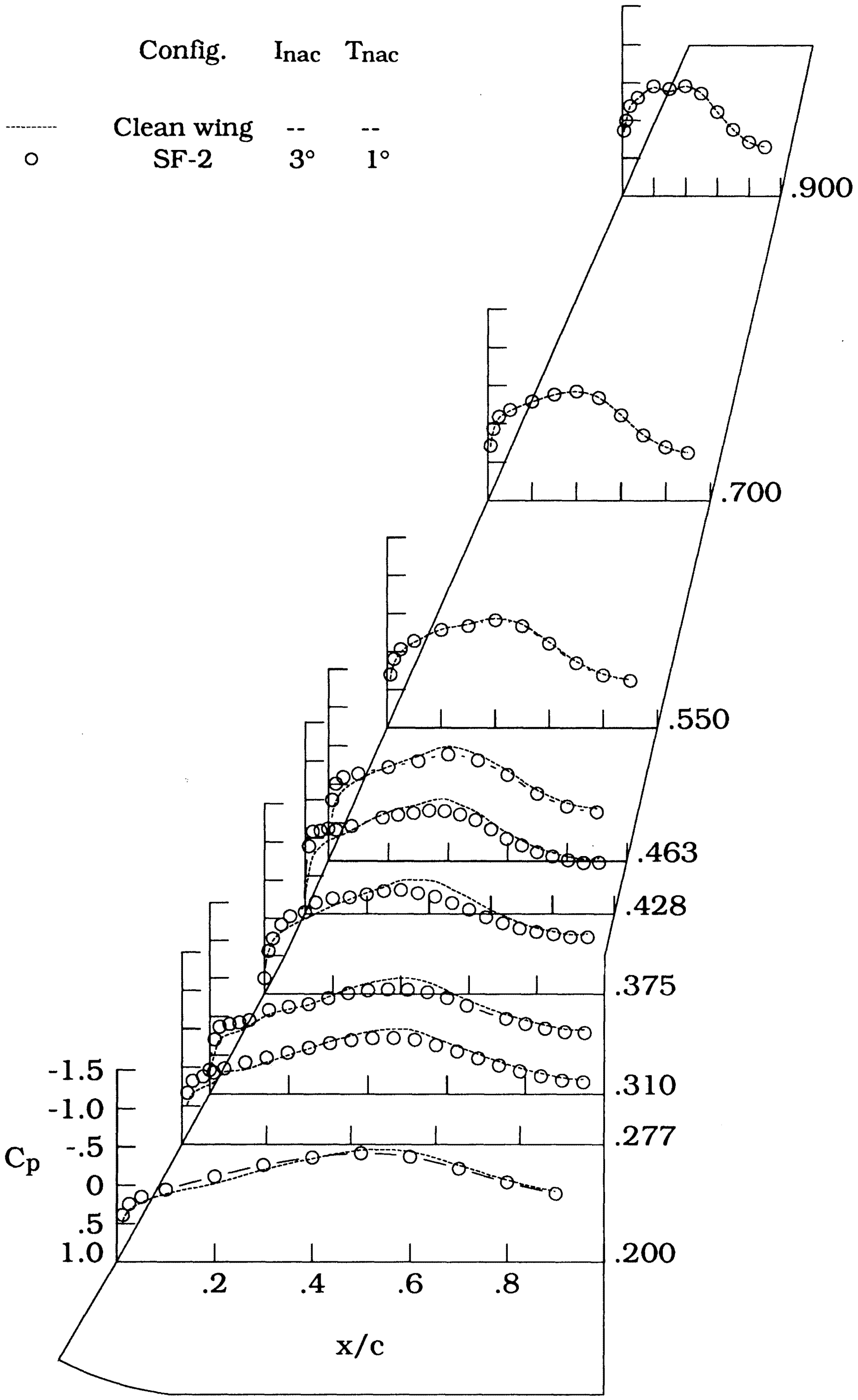

(b) Lower surface.

Figure 31. Concluded.

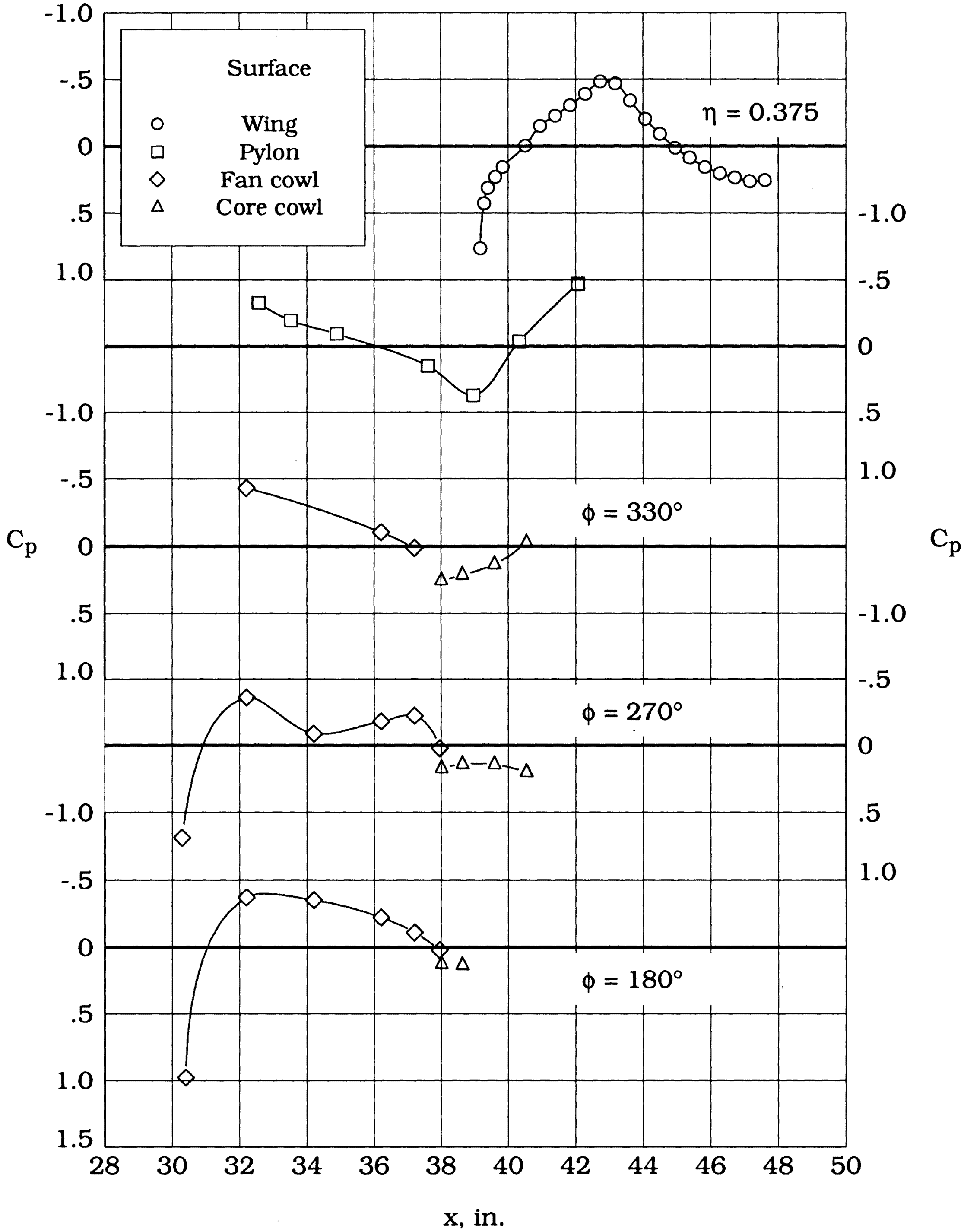

(a) Inboard.

Figure 32. Pressure distributions for ATF nacelle at $M_{\infty} = 0.77$ and $C_L \approx 0.55$ with nacelles mounted at $\eta = 0.400$.

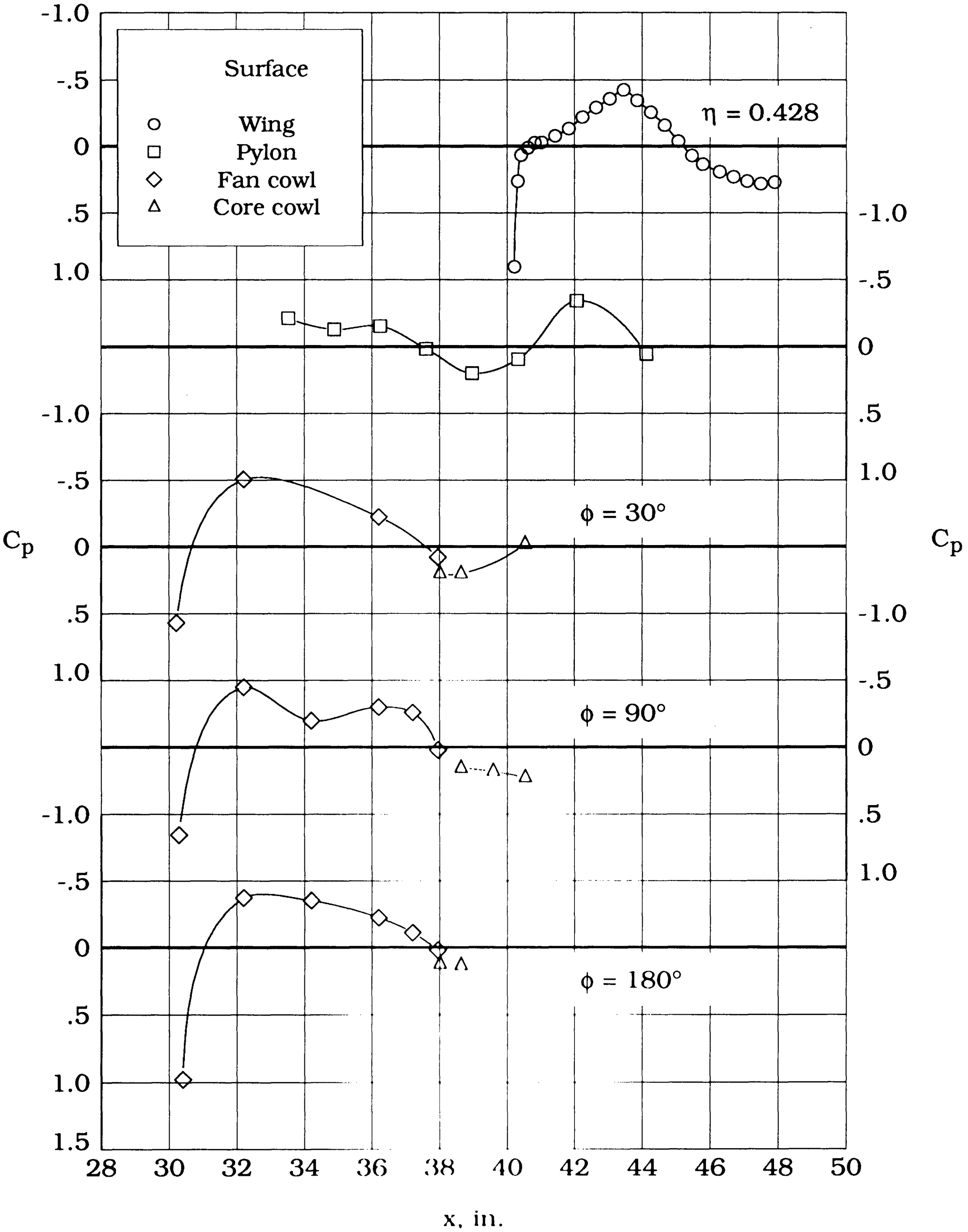

(b) Outboard.

Figure 32. Concluded.

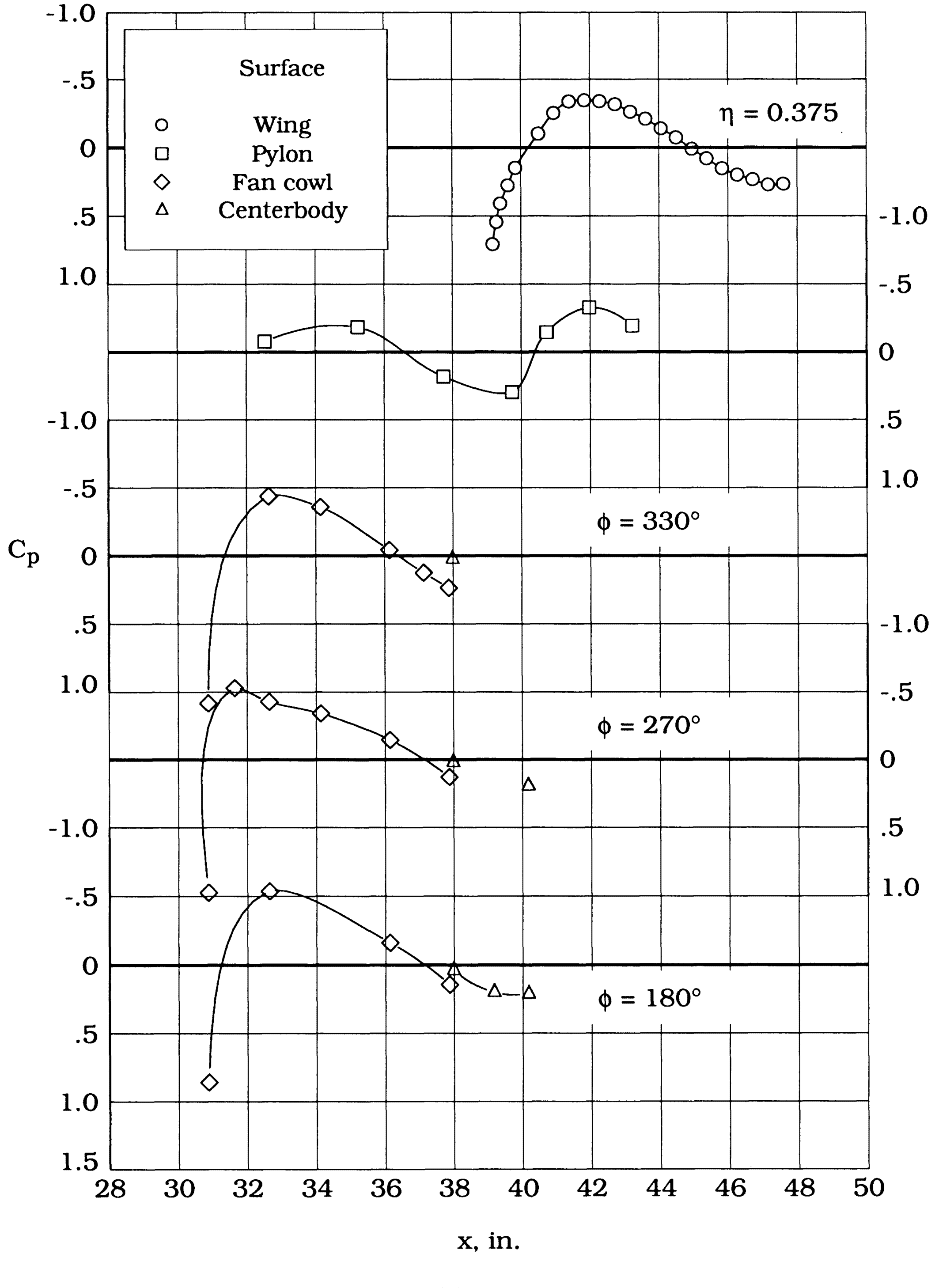

(a) Inboard.

Figure 33. Pressure distributions for SF-1 nacelle at $M_\infty = 0.77$ and $C_L \approx 0.55$ with nacelles mounted at $\eta = 0.400$.

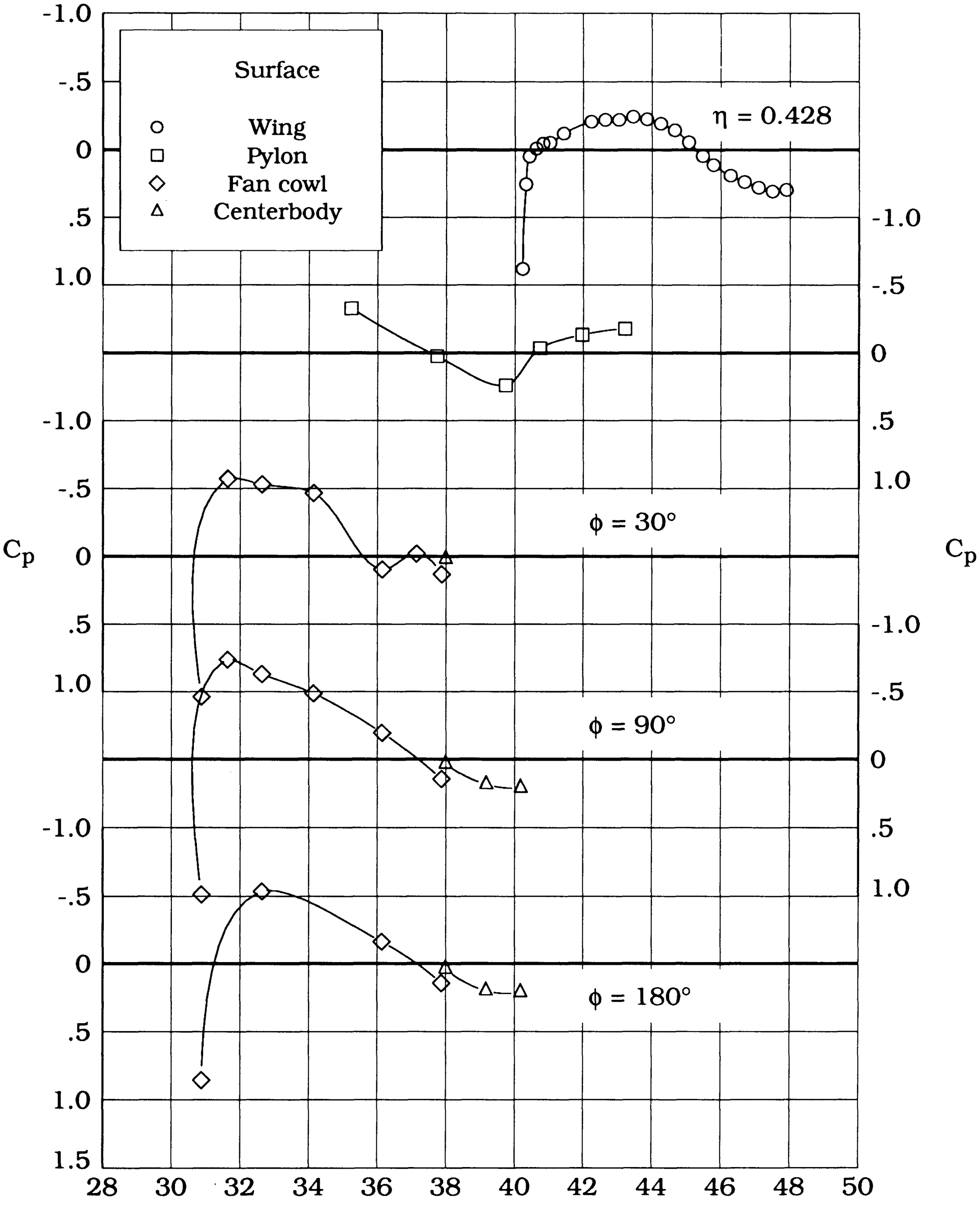

(b) Outboard.

Figure 33. Concluded.

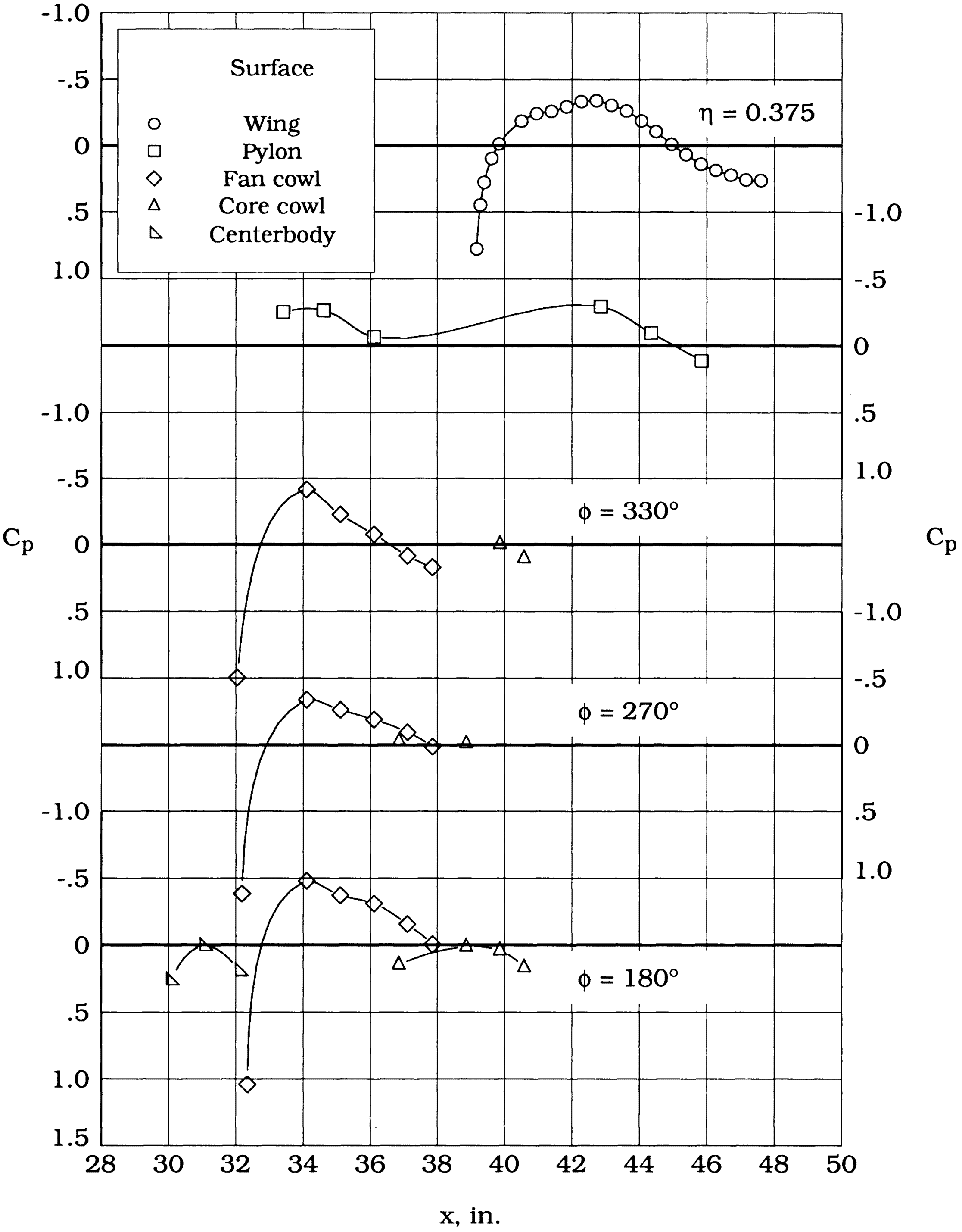

(a) Inboard.

Figure 34. Pressure distributions for SF-2 nacelle at $M_\infty = 0.77$ and $C_L \approx 0.55$ with nacelles mounted at $\eta = 0.400$.

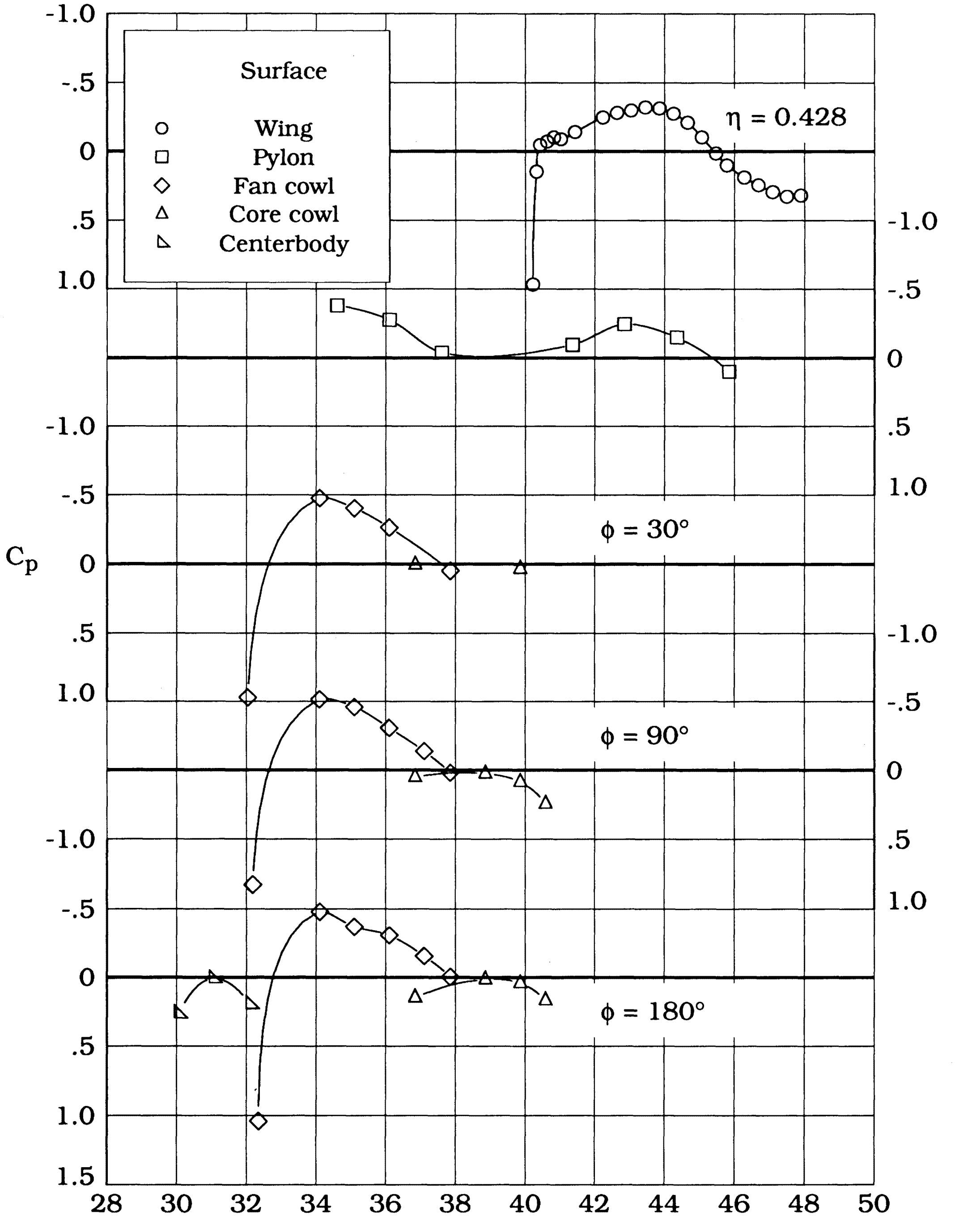

(b) Outboard.

Figure 34. Concluded.

REPORT DOCUMENTATION PAGE

Form Approved
OMB No. 0704-0188

1. AGENCY USE ONLY*(Leave blank)*

2. REPORT DATE
March 1992

3. REPORT TYPE AND DATES COVERED
Technical Paper

4. TITLE AND SUBTITLE
Installation Effects of Wing-Mounted Turbofan Nacelle-Pylons on a 1/17-Scale, Twin-Engine, Low-Wing Transport Model

5. FUNDING NUMBERS
WU 535-03-10-01

6. AUTHOR(S)
Odis C. Pendergraft, Jr., Anthony M. Ingraldi, Richard J. Re, and Timmy T. Kariya

7. PERFORMING ORGANIZATION NAME(S) AND ADDRESS(ES)
NASA Langley Research Center
Hampton, VA 23665-5225

8. PERFORMING ORGANIZATION REPORT NUMBER
L-16960

9. SPONSORING/MONITORING AGENCY NAME(S) AND ADDRESS(ES)
National Aeronautics and Space Administration
Washington, DC 20546-0001

10. SPONSORING/MONITORING AGENCY REPORT NUMBER
NASA TP-3168

11. SUPPLEMENTARY NOTES
Pendergraft, Ingraldi, and Re: Langley Research Center, Hampton, VA; Kariya: ViGYAN, Inc., Hampton, VA.

12a. DISTRIBUTION/AVAILABILITY STATEMENT

Unclassified–Unlimited

Subject Category 02

12b. DISTRIBUTION CODE

13. ABSTRACT *(Maximum 200 words)*

A twin-engine, low-wing transport model, with a supercritical wing of aspect ratio 10.8 designed for a cruise Mach number of 0.77 and a lift coefficient of 0.55, was tested in the Langley 16-Foot Transonic Tunnel. The purpose of this test was to compare the wing-nacelle interference effects of flow-through nacelles simulating *superfan* engines (very high bypass ratio (BPR $\approx$ 18) turbofan engines) with the wing-nacelle interference effects of current-technology turbofan engines (BPR $\approx$ 6). Forces and moments on the complete model were measured with a strain-gage balance, and extensive external static-pressure measurements (383 orifice locations) were made on the wing, nacelles, and pylons of the model. Data were taken at Mach numbers from 0.50 to 0.80 and at model angles of attack from -4° to 8°. Test results indicate that flow-through nacelles with a very high bypass ratio can be installed on a low-wing transport model with a lower installation drag penalty than for a conventional turbofan nacelle at a design cruise Mach number of 0.77 and lift coefficient of 0.55.

14. SUBJECT TERMS
Swept supercritical wing; Low-wing transport model; Underwing nacelles; Very high bypass ratio; and superfan nacelles; Installation interference; Propulsion integration

15. NUMBER OF PAGES
106

16. PRICE CODE
A06

17. SECURITY CLASSIFICATION OF REPORT
Unclassified

18. SECURITY CLASSIFICATION OF THIS PAGE
Unclassified

19. SECURITY CLASSIFICATION OF ABSTRACT

20. LIMITATION OF ABSTRACT

NSN 7540-01-280-5500

Standard Form 298(Rev. 2-89)
Prescribed by ANSI Std. Z39-18
298-102

NASA-Langley, 1992